

AN ABSTRACT OF THE THESIS OF

Shou-Po Shih for the degree of Master of Science in Electrical and Computer

Engineering presented on October, 10, 1995. Title: Electrical Characterization and Aging

Studies of ALE ZnS:Mn ACTFEL Devices with Varying Phosphor Layer Thicknesses

Redacted for privacy

Abstract approved: _

John F. Wager

Electrical characterization and aging studies are performed using ZnS:Mn alternating-current thin-film electroluminescent (ACTFEL) devices grown by atomic layer epitaxy (ALE). Three ACTFEL devices with different phosphor thicknesses, but similar structure are employed in this study. Electrical measurement indicates that more space charge generation is observed in ALE ZnS:Mn ACTFEL devices with thicker phosphor layers. In agreement with previous researchers, this space charge generation is attributed to deep-level impact ionization of the zinc vacancy portion of chlorine-zinc vacancy self-activated defect. Maximum charge-maximum applied voltage (Q_{\max} - V_{\max}) measurements indicate that the optical threshold voltage is similar to the threshold voltage obtained by Brightness-Voltage (B-V) analysis. At higher temperatures more space charge generation is observed. One piece of evidence that more space charge generation occurs at higher temperature is an increase in the amount of offset in charge-voltage (Q-V) and internal charge-phosphor field (Q- F_p) curves. A method to adjust for Q-V and Q- F_p offset is proposed. Aging trends of the "Normal" and the "Thin" ALE ZnS:Mn ACTFEL devices are more bulk-like and are attributed to chlorine migration in ZnS phosphor. In contrast,

the aging behavior of the "Thick" sample is more interface-like and is ascribed to the creation of deep-level, fixed charge states near the phosphor/insulator interface.

Electrical Characterization and Aging Studies of ALE ZnS:Mn ACTFEL Devices with
Varying Phosphor Thicknesses

by

Shou-Po Shih

A THESIS
submitted to
Oregon State University

in partial fulfillment of
the requirements for the
degree of

Master of Science

Completed October 10, 1995
Commencement June 1996

Master of Science thesis of Shou-Po Shih presented on October 10, 1995

APPROVED:

Redacted for privacy

Major Professor Representing Electrical and Computer Engineering

Redacted for privacy

Head of Department of Electrical and Computer Engineering

Redacted for privacy

Dean of Graduate School _____

I understand that my thesis will become part of the permanent collection of Oregon State University libraries. My signature below authorizes release of my thesis to any reader upon request.

Redacted for privacy

Shou-Po Shih, Author _____

ACKNOWLEDGMENTS

I would like to thank Dr. John F. Wager for his great patience, guidance, and support throughout my graduate studies in Oregon State University.

I would like to thank all researchers in the EL group.

Thanks to Juha Viljanen at Planar International for providing the samples used in this work.

I would also like to thank my parents and brothers for constantly support in my education.

This work is supported by the U.S. Army Research Office under Contract No. DAAH04-94-G-0324 and by the Advanced Research Projects Agency under the Phosphor Technology Center of Excellence, Grant No. MDA 972-93-1-0030.

TABLE OF CONTENTS

	<u>page</u>
1. INTRODUCTION.....	1
2. LITERATURE REVIEW OF ACTFEL DEVICE.....	4
2.1 Brief History and Background.....	4
2.2 Device Structure.....	5
2.3 Device Modeling.....	6
2.4 ACTFEL Device Fabrication.....	7
2.5 Device Operation.....	9
2.6 Previous ACTFEL Device Aging Studies.....	15
2.7 Previous ACTFEL Device Temperature Studies.....	20
3 EXPERIMENTAL TECHNIQUES.....	21
3.1 Sample Description and the Current-Limiting Problem.....	21
3.2 Introduction to C-V, Q-V, and Q-F _p Analysis.....	22
3.3 Capacitance-Voltage Analysis.....	24
3.4 Charge-External Voltage (Q-V) Analysis.....	27
3.5 Internal Charge-Phosphor Field (Q-F _p) Analysis.....	28
3.6 How to Relate the Q-F _p Curve to the Applied Voltage Waveform...	32
3.7 How to Estimate C _i and C _t by using Q-F _p Curves.....	32
3.8 Q _{max} -V _{max} Analysis.....	35
3.9 Electrical Characterization of ALE ZnS:Mn ACTFEL Devices: Experimental Procedure	36

TABLE OF CONTENTS (Continued)

	<u>page</u>
3.10 Electrical Characterization at Different Temperatures: Experimental Procedure.....	37
3.11 Aging Studies of ALE ZnS:Mn ACTFEL Devices with Different Phosphor Layer Thicknesses at Different Temperatures: Experimental Procedure.....	38
4 ELECTRICAL CHARACTERIZATION OF ALE ZNS:MN ACTFEL DEVICES.....	40
4.1 Introduction	40
4.2 The Origin of Space Charge Generation.....	41
4.3 Electrical Characterization of ALE ZnS:Mn ACTFEL Device with Variable Phosphor Thicknesses.....	42
4.4 Advantages and Disadvantages of Space Charge Generation.....	46
4.5 Q_{\max} - V_{\max} Measurements.....	49
4.6 Electrical Characterization of ALE ZnS:Mn ACTFEL Devices as a Function of Temperature.....	53
4.7 Aging Study of the "Normal" ALE ZnS:Mn ACTFEL Device.....	65
4.8 Aging Study of the "Thick" ALE ZnS:Mn ACTFEL Device.....	73
4.9 Summary of ALE ZnS:Mn ACTFEL Device Aging Trends.....	81
4.10 Brightness-Voltage Measurements.....	82
5 CONCLUSION AND RECOMMENDATIONS FOR FUTURE WORK.....	85
5.1 Conclusions.....	85
5.2 Recommendations for Future Work.....	87
BIBLIOGRAPHY.....	88

LIST OF FIGURES

<u>Figure</u>		<u>Page</u>
2-1	A typical ACTFEL device structure.....	5
2-2	Simple ACTFEL device equivalent circuit model.....	6
2-3	Growth of ZnS in the ALE process using ZnCl ₂ and H ₂ S source gases.....	8
2-4	Applied voltage waveform for ACTFEL device analysis.....	10
2-5	ACTFEL device in equilibrium.....	11
2-6	ACTFEL device with a positive voltage applied to the aluminum electrode.....	12
2-7	ACTFEL device with no external applied voltage, after removing the applied voltage to the Al electrode.....	13
2-8	ACTFEL device with a positive voltage applied to the ITO electrode.....	14
2-9	ACTFEL device with internal polarization field, after removing the applied voltage to the ITO electrode.....	14
3-1	Sawyer-Tower configuration.....	23
3-2	A typical C-V curve without space charge generation.....	25
3-3	Q-V curve for an ALE ZnS:Mn ACTFEL device with ATO insulators.....	27
3-4	Q-F _p curve for an ALE ZnS:Mn ACTFEL device with ATO insulators.....	29
3-5	Symmetric bipolar pulse waveform used for ACTFEL electrical characterization.....	30
3-6	Q-F _p curves obtained using different values of C _i and C _t	33

LIST OF FIGURES (Continued)

<u>Figure</u>	<u>Page</u>
4-1 C-V curves for a "Thin" ALE ZnS:Mn ACTFEL device for both applied voltage polarities.....	43
4-2 C-V curves for a "Thick" ALE ZnS:Mn ACTFEL device for both applied voltage polarities.....	44
4-3 Q-F _p curves for a "Thin" ALE ZnS:Mn ACTFEL device.....	46
4-4 Energy band diagram for an ACTFEL device without any space charge generation in the phosphor layer.....	47
4-5 Energy band diagram for an ACTFEL device with space charge generation in the phosphor layer.....	48
4-6 Q _{max} -V _{max} curve of positive polarity applied to Al electrode of "Normal" sample.....	51
4-7 Q _{max} -V _{max} curve of positive polarity applied to Al electrode of "Thick" sample.....	51
4-8 Insulator capacitance measured from C-V and Q-F _p curves as a function of temperature for the "Thick" ALE ZnS:Mn ACTFEL device.....	54
4-9 C-V curves as a function of temperature for the "Thick" ALE ZnS:Mn ACTFEL device when the Al electrode is positively biased.....	55
4-10 C-V curves as a function of temperature for the "Thick" ALE ZnS:Mn ACTFEL device when the Al electrode is negatively biased.....	55
4-11 "Offset-adjusted" Q-F _p curves as a function of temperature for the "Thick" ALE ZnS:Mn ACTFEL device. These curves are generated using C _i ^{phys} and C _p ^{phys} in the Q-F _p equations.....	56
4-12 Voltage transient measured across the sense capacitor and after "offset-adjustment".....	57

LIST OF FIGURES (Continued)

<u>Figure</u>	<u>Page</u>
4-13 “Offset-adjusted” $Q-F_p$ curves as a function of temperature for the “Thick” ALE ZnS:Mn ACTFEL device. These curves are generated using C_i^{qfp} and C_p^{qfp} in the $Q-F_p$ equations.....	58
4-14 Q_{cond} versus temperature for the “Thick” ALE ZnS:Mn ACTFEL device.....	59
4-15 Q_{relax} versus temperature for the “Thick” ALE ZnS:Mn ACTFEL device.....	60
4-16 Q_{pol} versus temperature for the “Thick” ALE ZnS:Mn ACTFEL device.....	60
4-17 F_{ss} versus temperature for the “Thick” ALE ZnS:Mn ACTFEL device.....	61
4-18 Q_{leak}^{qfp} and corrected Q_{leak}^{qv} versus temperature for the “Thick” ALE ZnS:Mn ACTFEL device.....	61
4-19 Offset of voltage transients measured across a sense capacitor versus temperature.....	62
4-20 C-V curves as a function of aging time for the “Normal” ALE ZnS:Mn ACTFEL device when the Al electrode is positively biased.	66
4-21 C-V curves as a function of aging time for the “Normal” ALE ZnS:Mn ACTFEL device when the Al electrode is negatively biased.	66
4-22 Insulator capacitance measured from C-V curves as a function of aging time for the “Normal” ALE ZnS:Mn ACTFEL device.....	67
4-23 Q_{ss} versus aging time for the “Normal” ALE ZnS:Mn ACTFEL device.....	67
4-24 Q_{cond} and Q_{leak} versus aging time for the “Normal” ALE ZnS:Mn ACTFEL device.....	69
4-25 Q_{relax} versus aging time for the “Normal” ALE ZnS:Mn ACTFEL device.....	69

LIST OF FIGURES (Continued)

<u>Figure</u>	<u>Page</u>
4-26 Q_{pol} versus aging time for the "Normal" ALE ZnS:Mn ACTFEL device.....	70
4-27 F_{ss} versus aging time for the "Normal" ALE ZnS:Mn ACTFEL device.....	70
4-28 Proposed aging mechanism for the "Normal" ALE ZnS:Mn ACTFEL device.....	71
4-29 Q - F_p curves as a function of aging time for the "Normal" ALE ZnS:Mn ACTFEL device.....	72
4-30 C-V curves as a function of aging time for the "Thick" ALE ZnS:Mn ACTFEL device when the Al electrode is positively biased.....	74
4-31 C-V curves as a function of aging time for the "Thick" ALE ZnS:Mn ACTFEL device when the Al electrode is negatively biased.....	74
4-32 Insulator capacitance measured from C-V curves as a function of aging time for the "Thick" ALE ZnS:Mn ACTFEL device.....	75
4-33 Q_{ss} versus aging time for the "Thick" ALE ZnS:Mn ACTFEL device.....	75
4-34 Q_{cond} and Q_{leak} versus aging time for the "Thick" ALE ZnS:Mn ACTFEL device.....	76
4-35 Q_{relax} versus aging time for the "Thick" ALE ZnS:Mn ACTFEL device.....	76
4-36 Q_{pol} versus aging time for the "Thick" ALE ZnS:Mn ACTFEL device.....	77
4-37 F_{ss} versus aging time for the "Thick" ALE ZnS:Mn ACTFEL device.....	77

LIST OF FIGURES (Continued)

<u>Figure</u>	<u>Page</u>
4-38 Q-F _p curves as a function of aging time for the “Thick” ALE ZnS:Mn ACTFEL device.....	78
4-39 Proposed aging mechanism for the “Thick” ALE ZnS:Mn ACTFEL device.....	79
4-40 B-V curves of the fresh and aged dots for the “Normal” sample.....	83
4-41 B-V curves of the fresh and aged dots for the “Thick” sample.....	83

LIST OF TABLES

<u>Table</u>		<u>Page</u>
4.1	A comparison of the insulator and total capacitance (nF/cm ²) of the "Thin", "Normal", and "Thick" ALE ZnS:Mn ACTFEL devices.....	42
4.2	A comparison of the ratio of the effective insulator capacitance as deduced by C-V or Q-Fp measurement to the calculated physical insulator capacitance.....	43
4.3	A comparison of the threshold voltage obtained from a Q_{\max} - V_{\max} measurement and from an observation of the minimum voltage for light emission and a comparison of $C_i^{q\max}$ and C_i^{phys}	50
4.4	A comparison of the slopes and intercepts of the Q_{\max} - V_{\max} regression lines for a positive voltage applied to the "Thick" sample.....	52

Electrical Characterization and Aging Studies of ALE ZnS:Mn ACTFEL Devices with Varying Phosphor Layer Thicknesses

Chapter 1 - Introduction

The development goal of alternating-current thin-film electroluminescent (ACTFEL) technology is to provide an alternative display technology which is of high quality, light-weight, and in a flat panel display format in order to replace cathode ray tube (CRT) based displays. Also, ACTFEL devices can be employed in heads-up displays, virtual-reality displays, and high-definition television.

Several flat panel display implementations are available, such as liquid crystal (LCD), plasma, field emission (FED), and electroluminescent (EL) displays. Currently, full-color LCD flat displays are popularly used as monitors for portable computers and for many other applications; however there are a few drawbacks associated with LCD's, such as insufficient brightness and viewing angle, which needed to be improved.

EL devices are based on the conversion of electrical energy into luminous energy. Light is emitted from II-VI compound phosphors via excitation of luminescent impurities by non-equilibrium electrons. Electrons injected from interface states into the phosphor are accelerated to energies large enough to excite EL luminescent centers. When the excited luminescent impurity subsequently decays into the ground state, the excess energy is converted into light. The electrical field across the II-VI compound phosphor is on the order of megavolts per centimeter. In this thesis, the II-VI compound and the luminescent center of interest are ZnS and manganese, respectively.

EL displays possess advantages [1] such as wide viewing angle, high contrast, high resolution, and the emissive nature of generation of the luminescence. There are four types of EL devices: (1) ac thin-film EL, (2) ac powder EL, (3) dc thin-film EL, and (4) dc powder EL. Currently, almost all commercial production and research are concentrated toward the development of ac thin-film EL displays.

Monochrome (yellow) ACTFEL displays are already commercially available. The monochrome phosphor is zinc-sulfide doped with manganese (ZnS:Mn), which emits yellowish-orange light. Full-color ACTFEL displays have been developed by Planar America and Planar International, but the light intensity of the blue phosphor needs to be improved. Another problem associated with ACTFEL devices is yield. As each pixel is an individual device, the ACTFEL panel must contain no defects in order to be shipped. Thus, deposition uniformity is of extreme importance.

The goals of this thesis are as follows: (1) To investigate the aging stability of ZnS:Mn ACTFEL devices grown by atomic layer epitaxy (ALE). (2) To investigate space charge generation as a function of the phosphor thickness in ALE ZnS:Mn ACTFEL devices. These experimental results are then compared to space charge generation simulations using the single sheet charge model developed by Paul Keir. (3) To investigate space charge generation as a function of temperature in ALE ZnS:Mn ACTFEL devices. (4) To perform Q_{\max} - V_{\max} [2] experiments as a function of phosphor thickness using ALE ZnS:Mn ACTFEL devices.

The thesis is organized as follows. Chapter 2 is a review of literature relevant to the fundamental device physics of ACTFEL device operation and of previous work

performed by other researchers, but not directly related to the specifics of the present study. Chapter 3 presents a description of the samples employed and a short review of the techniques used for the electrical characterization of ACTFEL devices. Chapter 4 contains the space charge generation analysis for samples with different phosphor thicknesses, the space charge generation analysis with respect to different temperatures, and the aging analysis of ALE ZnS:Mn ACTFEL devices. The final chapter contains conclusions and suggestions for future work.

Chapter 2 - Literature Review of ACTFEL Devices

2.1 Brief History and Background

High-field electroluminescence was discovered by Destriau in 1936 [4]. He observed light emission from a ZnS phosphor powder dispersed in an insulator and sandwiched between two electrodes when a large ac voltage was applied. Later, during the 1950s and 1960s, ac powder EL studies focused on the development of a flat light source for wall illumination.

The first thin-film EL structures were deposited in the late 1950's [5], after the development of a transparent conductive film (SnO_2). In the 1960's Vlasenko and Popkov observed [6] a very steep rise of luminance with respect to voltage in yellow-emitting ZnS:Mn thin-film EL devices. The development of the double-insulating-layer structure (Russ and Kennedy, 1967) improved the lifetime and luminance of these devices [7].

At the 1974 SID International Symposium, Inoguchi *et al.* demonstrated [8] a stable, high-luminance orange-yellow-emitting ZnS:Mn thin-film EL panel using the double-insulating-layer structure. Subsequently, Mito *et al.* showed [9] that this EL panel could be used for TV imaging. In 1983, Tekeda *et al.* reported [10] the first commercial production of EL panels.

2.2 Device Structure

The ACTFEL devices used in this thesis are fabricated at Planar International, Espoo, Finland and are grown by atomic layer epitaxy (ALE) [1, 3, 32]. The device structure of a

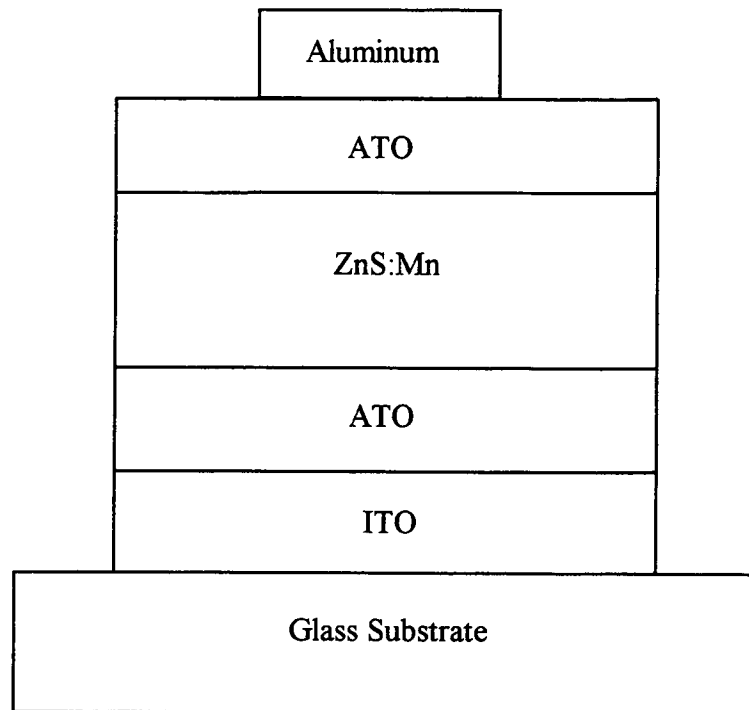


Figure 2-1. A typical ACTFEL device structure.

typical ACTFEL device is shown in Fig. 2-1. The device is fabricated on a glass substrate and consists of a phosphor layer sandwiched between two insulating layers and a pair of electrodes. The top electrode is aluminum and the bottom electrode is usually indium-tin oxide (ITO); this material is used because it is transparent to visible light. The insulators

are typically aluminum-titanium oxide (ATO). ATO is selected because it has a high dielectric constant and a high electrical breakdown strength. The phosphor layer is zinc sulfide, a II-VI semiconductor, doped with manganese (ZnS:Mn). It emits yellowish-orange light with a peak wavelength of 580 nm.

2.3 Device Modeling

This section is a review of ACTFEL device modeling. The simplest ACTFEL equivalent circuit model, shown in Fig. 2-2, is introduced here because it is later used to estimate the physical insulator capacitance and physical phosphor capacitance of the ACTFEL device. As shown in Fig. 2-2, the breakdown voltage of the Zener diodes is set to the threshold voltage for the onset of conduction across the phosphor. The phosphor capacitance is then shorted during conduction. This circuit model was proposed by Smith [12].

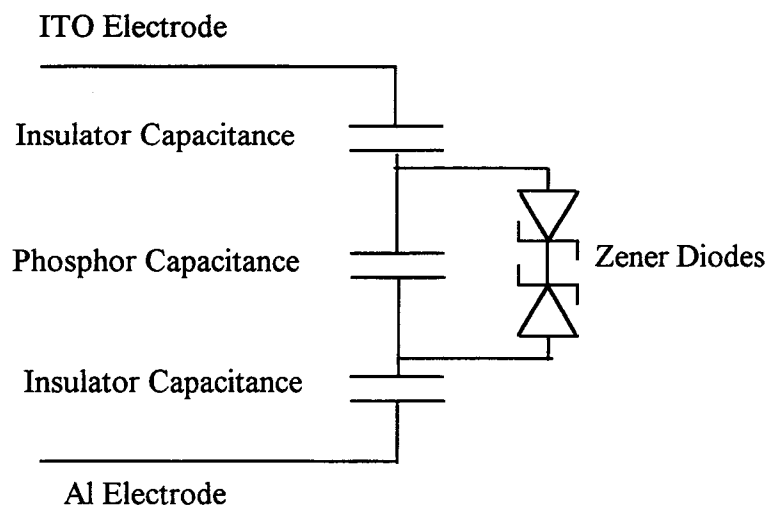


Figure 2-2. Simple ACTFEL device equivalent circuit model.

The physical insulator capacitance and total capacitance are estimated using the following parallel capacitors equations.

$$\frac{1}{C_{insulator}} = \frac{1}{C_{insulator}^{top}} + \frac{1}{C_{insulator}^{bottom}} \quad (2.1)$$

$$\frac{1}{C_{total}} = \frac{1}{C_{insulator}} + \frac{1}{C_{phosphor}} \quad (2.2)$$

Two sophisticated ACTFEL device equivalent circuit models are proposed by Keir *et al.* [13]. He includes the effects of space charge generation due to field emission or deep-level impact ionization in the ACTFEL devices into the equivalent circuit.

2.4 ACTFEL Device Fabrication

ACTFEL devices may be fabricated using physical vapor [5, 14] deposition (PVD) or chemical vapor deposition (CVD). PVD includes electron beam deposition (EBD), multi-source deposition (MSD), sputtering, and evaporation, while CVD includes metal-organic chemical vapor deposition (MOCVD), halide transport chemical vapor deposition (HTCVD), and atomic layer epitaxy (ALE).

Most commercial ACTFEL devices are fabricated using evaporation, sputtering, or ALE. All of the ACTFEL devices used in this work are fabricated by ALE. Therefore, a short discussion of ALE is provided as follows.

The ALE technique [1, 5, 11] is one of the most successful growth methods used in the commercial production of ACTFEL devices. The ALE process depends upon an exchange reaction between alternatively supplied gaseous reactants chemisorbed onto a

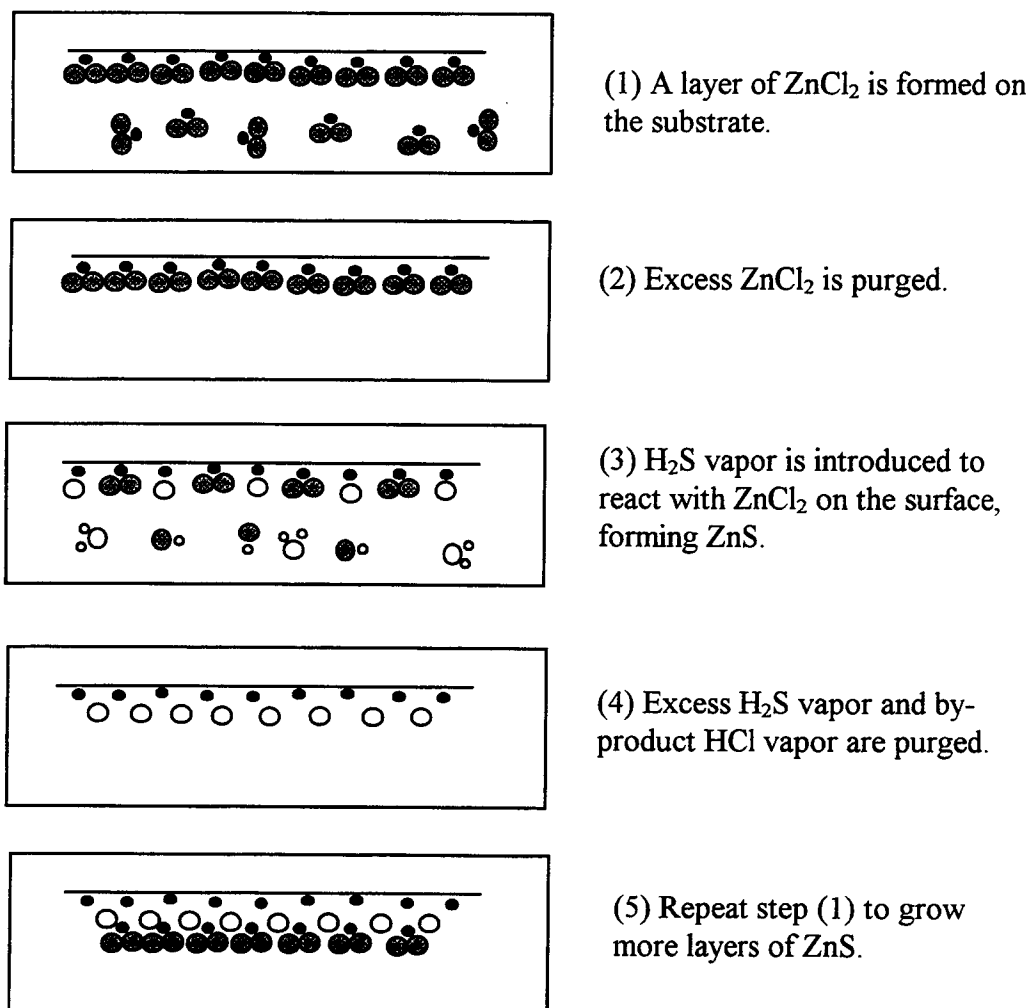
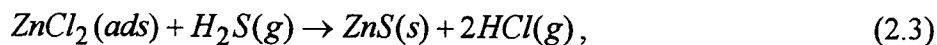


Figure 2-3. Growth of ZnS in the ALE process using ZnCl_2 and H_2S as source gases [1, 5, 11, 14].

substrate surface. As shown in Fig. 2-3, the ALE process for the deposition of ZnS is established by first exposing the substrate to a pulse of ZnCl_2 gas, thereby forming a single layer of ZnCl_2 on the surface. Excess Zn is removed as a ZnCl_2 vapor during the purge

portion of the deposition cycle in which N_2 flows through the ALE reactor. Next, a pulse of H_2S gas is introduced into the ALE reactor. S reacts with the chemisorbed Zn to form ZnS on the surface. By-products, such as HCl, are purged. The deposition cycle is then repeated to create more layers of ZnS. It is found that ZnS films grown at $350^\circ C$ have the cubic (zinc-blende) crystal structure and films grown at $500^\circ C$ have the hexagonal (wurtzite) structure. The ALE growth process for ZnS, based on the exchange reaction,



is indicated in Fig. 2-3.

According to Planar America, the ALE process has the following advantages [15]:

- (1) High thickness uniformity and properties across the panel.
- (2) High repeatability; similar panel properties are obtained run-to-run.
- (3) Conformal coating; textured surfaces may be uniformly coated.
- (4) Excellent properties and high yield compared to other thin film deposition processes.

2.5 Device Operation

ACTFEL devices operate by applying [16] an AC bias to the electrodes. In a matrixed flat panel display, a voltage just below the threshold for light emission is applied to the row electrodes and another voltage pulse is applied to the column electrodes such that the total voltage across the device exceeds the threshold voltage and light is emitted from the device. Typically, ACTFEL device operation is specified at a voltage of 40 V above threshold voltage.

For research purposes, the standard waveform used in this work to drive an ACTFEL device is symmetric with alternating bipolar pulses of trapezoidal shape with $5\ \mu\text{s}$ rise and fall times and a pulse width of $30\ \mu\text{s}$. The frequency of the waveform is $1\ \text{kHz}$. A typical amplitude of the waveform is about 60 to $100\ \text{V}$ above the threshold voltage (i.e. $200\ \text{V}$ to $260\ \text{V}$).

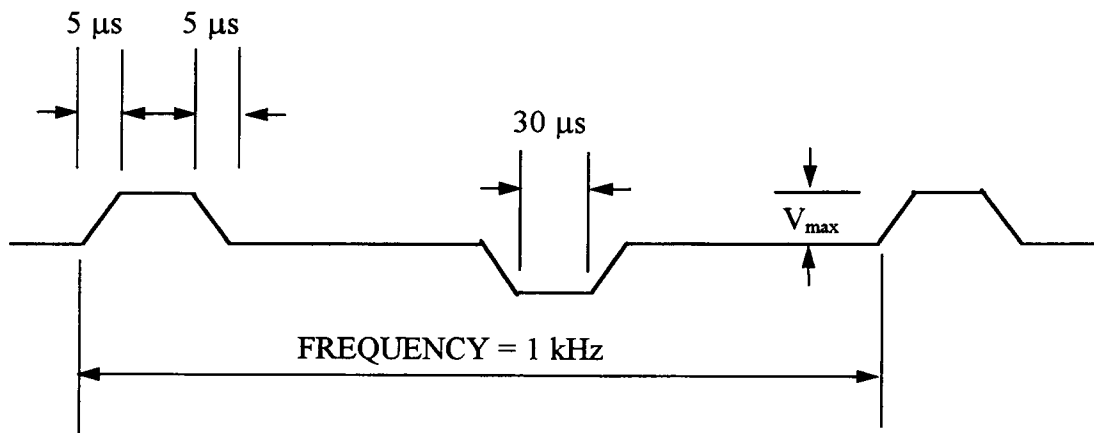


Figure 2-4. Applied voltage waveform for ACTFEL device analysis.

Once a bias is applied to the electrodes of the ACTFEL device, the voltage dropped across the ACTFEL device divides across the insulator and phosphor capacitors until breakdown occurs. At this point, the voltage drop across the phosphor layer has an associated field which introduces a large number of electrons into the phosphor, via tunnel emission from interface states. Some of these injected electrons are sufficiently hot to excite luminescent impurities, which subsequently radiatively recombine, giving off light.

Further increases in the applied voltage above threshold result in an increase in the conduction charge which gives higher luminescence [14, 16 17].

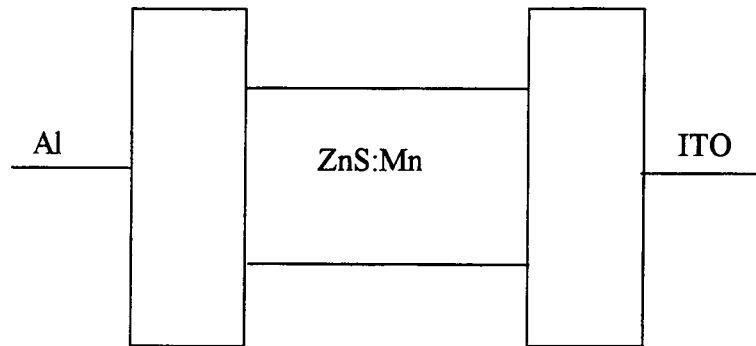


Figure 2-5. ACTFEL device in equilibrium.

An alternative way to discuss the device physics operation of an ACTFEL device is through the use of an energy band diagram. In the following discussion, an ideal ACTFEL device is used to explain basic aspects of device operation, whereas in Chapter 4, ACTFEL devices with space charge generation are discussed. An equilibrium energy band diagram of an ideal ACTFEL device is shown in Fig. 2-5 [14, 16, 17]. Application of a positive bias to the Al electrode of the ACTFEL device results in the situation shown in Fig. 2-6. When the phosphor electrical field reaches a critical value, electrons tunnel out of energy states located at the ZnS/insulator interface into the ZnS conduction band. These states are distributed throughout the band gap and are referred to as interface states. The emitted electrons are accelerated by the phosphor electrical field towards the opposite interface. The current flowing during this breakdown of the phosphor dissipates real

power and is known as conduction current. As electrons move in the field, they gain energy. If electrons gain sufficient energy before reaching the other interface they may be able to impact excite a luminescent impurity (2.1 eV is required for Mn excitation). Note

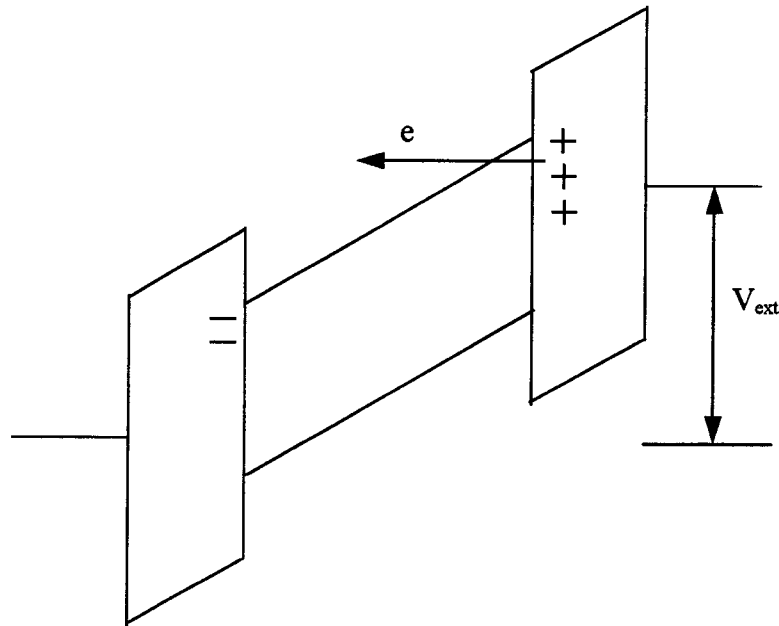


Figure 2-6. ACTFEL device with a positive voltage applied to the aluminum electrode.

that impact excitation does not involve space charge generation. When the excited luminescent impurity atom decays to its ground state, a photon is emitted with energy corresponding to the difference between that of the excited and the ground state. For Mn doped in ZnS the emitted light is centered at 585 nm and emits orange-yellow light. Once the electrons reach the opposite interface, they are captured at interface states. In the process of moving electrons from one interface to another, a charge imbalance occurs; one interface is positively charged and the other interface is negatively charged. The absolute

value of the charge which remains at one interface after the voltage pulse terminates is called the polarization charge. Polarization charge gives rise to a phosphor field component, F_{pol} , that discourages the additional injection of electrons.

After the application of an external voltage pulse, the phosphor field is non-zero and equal to F_{pol} and the polarity of F_{pol} is reversed from what it was during the previous applied voltage pulse, as shown in Fig. 2-7. The resulting band bending indicated in Fig. 2-7 is simply explained by Kirchhoff's voltage law where the sum of voltages must equal zero (i.e. $V_{phosphor} + V_{insulators} = V_{ext} = 0$, where $V_{phosphor}$ is the voltage across the phosphor, $V_{insulator}$ is the voltage across the insulators, and V_{ext} is the external applied voltage).

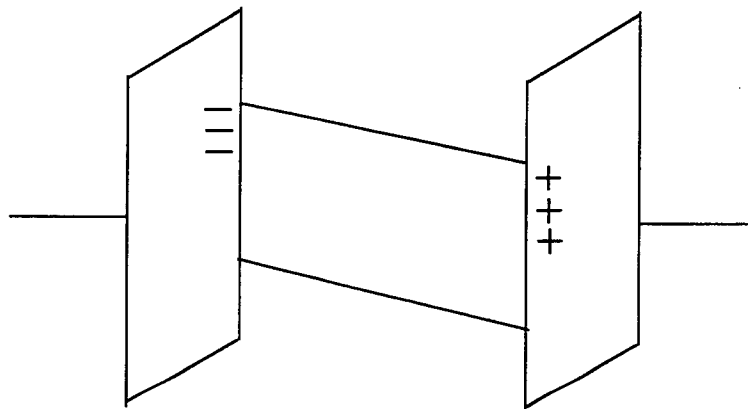


Figure 2-7. ACTFEL device with no external applied voltage, after removing the applied voltage to the Al electrode.

The external voltage is zero until the next voltage pulse of opposite polarity arrives, as shown in Fig. 2-8. Notice that during this voltage pulse the polarity of the polarization assists the emission of electrons and lowers the turn-on voltage. The presence

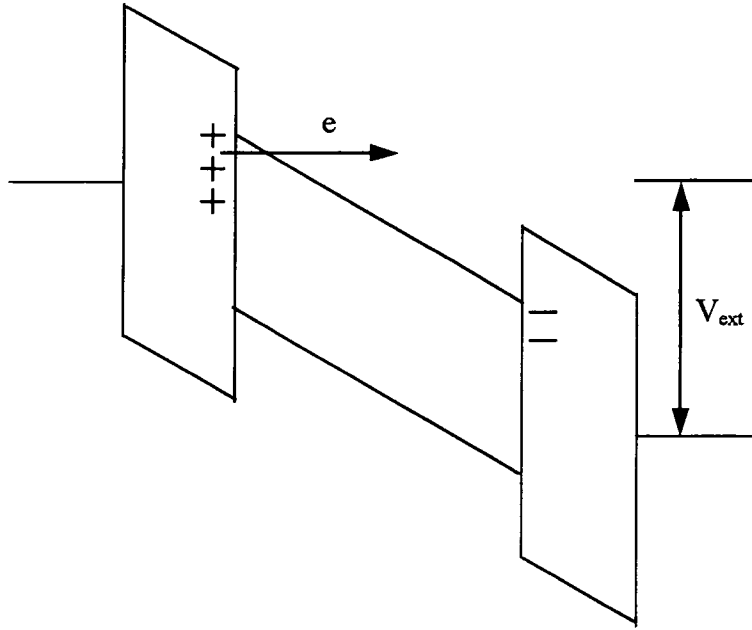


Figure 2-8. ACTFEL device with a positive voltage applied to the ITO electrode.

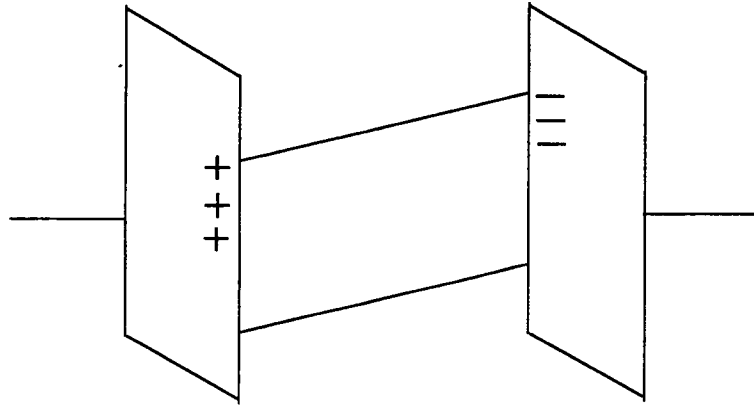


Figure 2-9. ACTFEL device with internal polarization field, after removing the applied voltage to the ITO electrode.

of polarization charge establishes an internal field in the phosphor and, thus, reduces the amount of external voltage required for conduction. Also note that the resulting conduction current flows in an opposite direction with respect to Fig. 2-6. Figure 2-8 is an energy band diagram after the application of a positive voltage pulse is applied to the ITO electrode; note that this results in a build up of polarization charge and a band bending which is of opposite polarity to that shown in Fig. 2-9. This energy band cycle continues as subsequent voltage pulses are applied to the ACTFEL device. Luminescent impurities are continuously excited during the portion of the cycle in which conduction occurs and light is given off as those excited luminescent impurities decay to their ground states.

2.6 Previous ACTFEL Device Aging Studies

The aging characteristics and device stability of ACTFEL flat panel displays have been the subject of numerous studies. The majority of this work has focused on monitoring the brightness versus voltage (BV) curve of an ACTFEL device as a function of aging time. An alternative approach is to monitor the electrical characteristics of ACTFEL devices in order to study the electrical properties of ACTFEL devices [14, 18].

It is found that evaporated ZnS:Mn ACTFEL devices show a positive shift (p-shift) in the B-V curves in which the threshold shifts to increasing voltage with aging. In contrast, ALE ZnS:Mn ACTFEL devices exhibit a negative shift (n-shift) in which the threshold shifts to lower voltages during the aging process. Simultaneous with the n-shift,

the rise in brightness as a function of voltage becomes less steep with aging, which is referred to as a softening [14, 18]. Thioulouse *et al.* propose [19] that softening is induced by electrochemical reactions due to the migration of chlorine ions toward the ZnS-insulator interface.

Mikami *et al.* [20] are able to fabricate ZnS:Mn ACTFEL devices with either n- or p-shift, using HTCVD to grow the ALE ZnS:Mn. They conclude that the growth temperature controls whether the shift is n- or p-type, at least when HTCVD growth is employed. When ZnS:Mn is prepared by vacuum evaporation, the growth temperature is less than 200°C while ALE growth occurs at about 500°C. Mikami *et al.* explain the negative shift as a combination of a softening and a shifting of the B-V curve, which they attribute to an effect associated with asymmetric polarization charge and band bending in the ZnS layer, respectively. On the other hand, the positive shift is attributed to bulk-limited conduction, in which case the conduction is symmetric.

Workers at Planar America and Oregon State University have tried to improve the stability of ACTFEL devices by adding a CaS layer at one or both of the phosphor-insulator interfaces [14]. Another approach involved oxygen exposure of the ZnS layer prior to the second insulator deposition. The conclusion of their work is that both approaches improve ACTFEL device stability. However, the second approach reduces the brightness of the device. Their explanation for the improved stability of the ACTFEL device is associated with a reduction in the tendency of sulfur vacancies to form and diffuse during device operation.

Workers at Lohja and Helsinki University of Technology performed [21] aging studies by monitoring the B-V characteristics of devices grown by ALE. The ALE devices studied have an $\text{Al}_2\text{O}_3\text{-ZnS:Mn-Al}_2\text{O}_3$ structure sandwiched between two sputtered ITO layers. They conclude that the aging process is due to electron trapping at the ZnS:Mn insulator interface. Electron trapping increases as the aging time increases. Also, shifting of B-V curves to lower threshold voltages with aging time is attributed to trapping at the ZnS:Mn insulator interface.

Another approach for studying ACTFEL device aging is to monitor the electrical characteristics of an ACTFEL device as a function of aging time [22, 23]. Davidson performed aging studies of ZnS:Mn ACTFEL devices grown by vacuum evaporation. These experiments are performed for 45 hours by monitoring the C-V and Q-V characteristics at various temperatures (80°C , 60°C , 20°C , 0°C , -10°C and -50°C). Davidson observed that (1) the threshold voltage shifts rigidly to higher voltage, (2) the C-V transition region shifts rigidly (p-shift), and (3) the insulator and phosphor capacitance are constant with respect to aging time. The p-shift observed in the C-V electrical characterization is concomitant with the p-shift observed in the B-V optical characterization. In addition, he observed that the aging rate increased as temperature increased. These observations indicate that the electrostatic charge distribution responsible for aging occurs near the phosphor/insulator interfaces, and the degradation of the ACTFEL device is due to changes in the fixed charge and not due to changes in the interface state charge. From these observations, an aging model for evaporated ZnS:Mn ACTFEL devices is provided to explain the aging of these devices. This model suggests

that the formation of deep level, fixed charge states is a result of atomic rearrangement at the insulator/phosphor interface where electrons are trapped and give rise to a reduction in the conduction charge.

Another researcher at Oregon State University, Abu-Dayah, performed aging experiments by monitoring the $Q-F_p$ and C-V characteristics as a function of time [13, 18]. The samples used are yellow ALE ZnS:Mn ACTFEL devices deposited at Planar International. The phosphor thickness is 5500 Å and the ATO insulator thickness is about 2700 Å. Aging of the ACTFEL device is conducted at room temperature. The longest aging time employed is 50 hours. All of the electrical characterization is accomplished in an automated fashion. The driving waveform used in this experiment is the standard waveform described earlier with a voltage amplitude of 210 V.

For a positive pulse applied to the Al electrode (Al-plus), the C-V curve shifts in a non-rigid manner with respect to aging time; the non-rigid shift in the C-V curve indicated that the pre-clamping interface state density, Q_{ss} [24], increases as a function of aging time. From the C-V curve, the softening indicates that electrons are injected from shallower interface states as aging progresses. The insulator capacitance, C_i , as obtained from C-V measurements, decreases with aging time; most of the decreases in C_i occurs during the initial 10 hours of aging.

For a negative voltage pulse applied to the Al electrode (Al-minus; i.e. the electrons are emitted from the Al interface), it is observed that the C-V curves are quite different initially and they display distinctly different aging trends than when a positive pulse is applied to the Al electrode. Thus, the electrical properties and aging

characteristics associated with the two voltage polarities, and presumably the two phosphor/insulator interfaces, are also quite different.

Overshoot is observed in Al-minus C-V curves, which is evidence for space charge generation. The magnitude of this overshoot decreases with aging. C-V curves first shift rigidly to lower voltages and then shift almost rigidly to higher voltages with increasing aging time. This rigid shift is interpreted as indicating that Q_{ss} is rather constant with aging. Furthermore, since these C-V curves are rather steep, Q_{ss} is relatively small. As a result of these aging studies, it is observed that the interface state distributions at the Al and ITO interfaces are asymmetric and, furthermore, exhibit highly asymmetric aging characteristics.

In summary, Abu-Dayah's work concludes the following [14, 18]:

- (1) The interface state densities of the top and bottom interface are distinctly different and exhibit different aging characteristics.
- (2) Both shallow and deep traps are created during aging at the bottom interface.
- (3) A lesser number of predominately deep traps are created at the top interface during aging.
- (4) The decrease in C_i with aging indicates that some of the "interface state charge" actually moves deeper into the ZnS bulk with aging.
- (5) The decrease in the C-V overshoot of the bottom interface indicates that the amount of space charge build up in the ZnS decreases with aging time.

2.7 Previous ACTFEL Device Temperature Studies

Davison performed an aging study of evaporated ZnS:Mn ACTFEL devices as a function of temperature [22]. He observed a linear relationship of the threshold voltage with temperature, but the cause of this temperature dependence was uncertain. He checked the insulator capacitance and the dielectric constant from 20°C to 95°C and found a variation of only 4 percent, which is too small to account for the observed temperature-dependent aging trends.

Chapter 3 Experimental Techniques

3.1 Sample Description and the Current-Limiting Problem

Three yellow ALE ZnS:Mn ACTFEL devices from Planar International are used in this thesis. These devices have the same structure described previously in Fig. 1, Chapter 2. The ATO insulator thicknesses are approximately constant for all of these devices and range from 230 nm to 290 nm. The phosphor layer thicknesses are approximately 230, 550 and 920 nm. These devices are referred to as “Thin”, “Normal”, and “Thick”, respectively, in the remainder of this thesis.

The ALE samples received from Planar International have 12 dots deposited on a 6 X 4 inch glass substrate. Each dot has an area of 0.49 cm². This large area requires a large amount of current to turn on the device. Unfortunately, the high voltage amplifier used for this experiment is current-limited when such large-area devices are tested. Consequently, the voltage waveform supplied to the ACTFEL device is severely distorted so that C-V, Q-F_p, and Q-V curves are no longer reliable due to the voltage waveform distortion.

The solution to overcoming the amplifier current-limiting problem is to evaporate smaller aluminum dots onto the sample and to test these small-area dots. The large plates received from Planar International are cut into small pieces of 2 X 2 inch. New aluminum dots of area 0.0792 cm² are evaporated onto the top of the ACTFEL stack. Some of these small dots are aged for 24 hours in order to perform C-V, Q-V, and Q-F_p measurements on “burned in” dots whose properties do not change significantly with time.

Other fresh dots are used for aging experiments. It is observed that the voltage waveform distortion is negligible when these small dots are tested. Therefore, smaller aluminum dots help to reduce the current needed to drive the ACTFEL devices and the current-limiting problem is circumvented.

3.2 Introduction to C-V, Q-V, and Q-F_p Analysis

The electrically measurable quantities useful for characterizing an ACTFEL device can be divided into two major groups: (1) external quantities, measured with respect to the electrodes of the device, and (2) internal quantities, associated with that of the phosphor. The standard methods used to characterize the electrical properties of ACTFEL devices are C-V, Q-V, and Q-F_p analysis. The Q-V [5, 14, 16] method is used to determine both external and internal electrical quantities. Conduction charge and relaxation charge are quantities determined with respect to the external applied voltage. Turn-on voltage, insulator capacitance, phosphor capacitance, leakage charge, and polarization charge are external quantities obtained from Q-V curves. The C-V [14, 16, 22, 24] method can only measure external quantities and is used to establish different turn-on voltages, the interface state density in the pre-clamping regime, the total capacitance, and the insulator capacitance. The Q-F_p [2, 13, 14, 17, 25] method measures only internal quantities such as conduction charge, relaxation charge, leakage charge, polarization charge, and steady-state field inside the phosphor.

In order to plot C-V, Q-V, or Q-F_p curves, the external applied voltage and the current or the total charge flowing through the device must be measured with respect to time. Current is measured as a voltage drop across a small resistor (10.5 Ω in this case) in series with the ACTFEL device. Total external charge is measured as a function of time by placing a capacitor (110.8 nF in this case) in series with the device, which effectively integrates the current. This is known as the Sawyer-Tower configuration and is shown in Fig. 3-1.

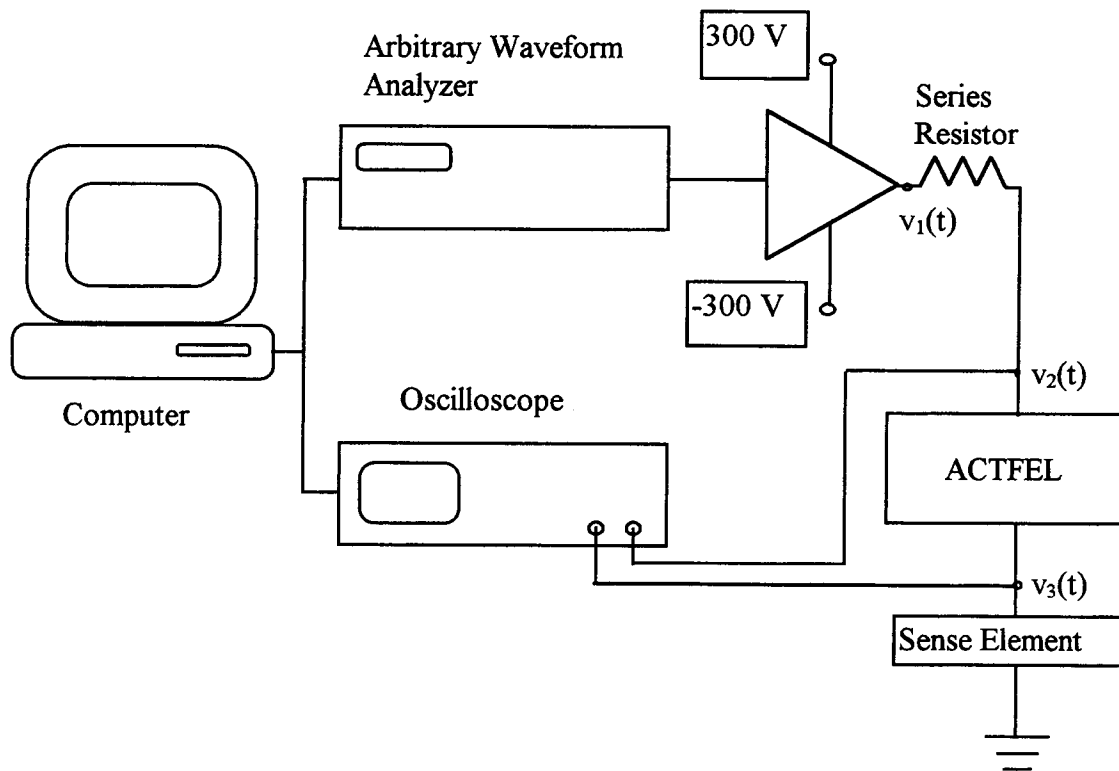


Figure 3-1. Sawyer-Tower configuration.

3.3 Capacitance-Voltage Analysis

A C-V curve is generated by plotting the ratio of the current to the time derivative of the voltage versus the voltage using the following equation,

$$C(t) = \frac{i(t)}{\frac{d[v_2(t) - v_3(t)]}{dt}} \quad (3.1)$$

The current, $i(t)$, is calculated from the voltage across the sense resistor,

$$i(t) = \frac{v_3(t)}{R_c} \quad (3.2)$$

Alternatively a C-V curve may be generated by plotting

$$C(t) = \frac{dq(t)}{dV(t)} = \frac{d[C_{sense} v_3(t)]}{d[v_2(t) - v_3(t)]} \quad (3.3)$$

when a sense capacitor is used.

At voltages just below the threshold voltage, the measured capacitance is the total capacitance of the phosphor capacitor, the top insulator capacitor, and the bottom insulator capacitor in series. Above the threshold voltage, the phosphor capacitor breaks down due to the flow of conduction charge; therefore, the measured capacitance increases to that of the total insulator capacitance. Note that experimentally the physical insulator capacitance is only measured in the absence of space charge generation in the phosphor and when enough conduction occurs across the phosphor that the flow of conduction current completely shunts the phosphor capacitance. Space charge generation tends to yield a measured C-V capacitance greater than that of the physical insulator capacitance

whereas an inadequate flow of conduction charge results in a measured C-V capacitance smaller than that of the physical insulator capacitance.

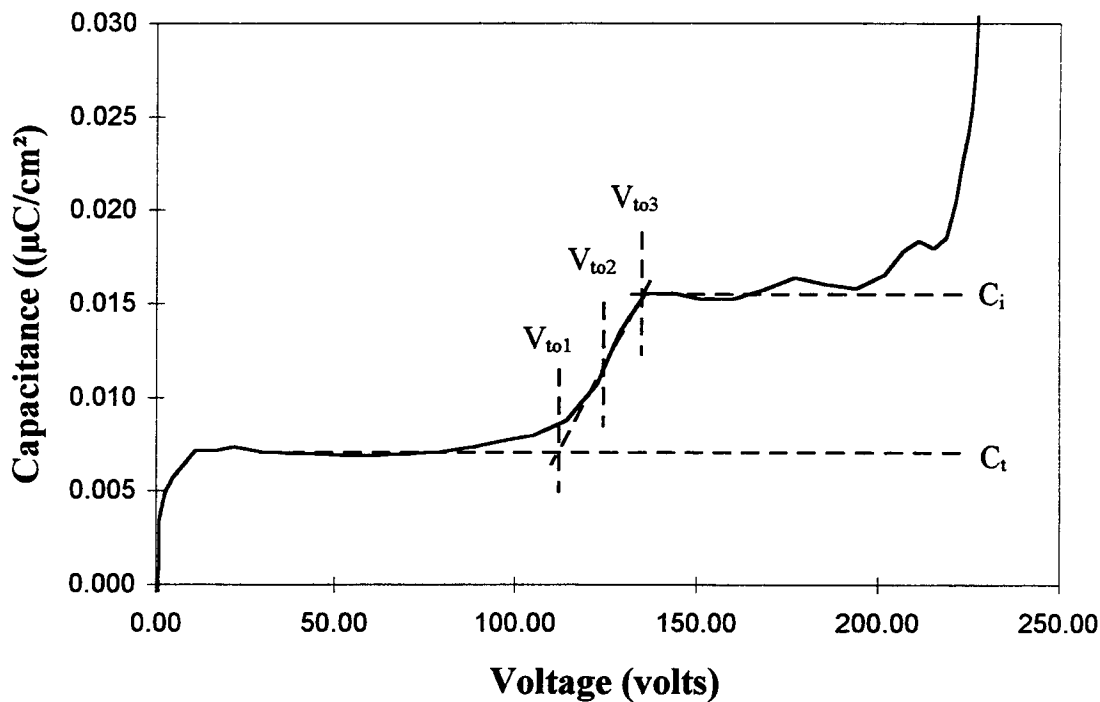


Figure 3-2: A typical C-V curve without space charge generation.

A typical C-V curve without space charge generation is shown in Fig. 3-2. The total capacitance and insulator capacitance can be directly read from the C-V curve. In addition, information such as the turn-on voltages (i.e. V_{to1} , V_{to2} , and V_{to3}), the source of the charge (i.e. interface or bulk), and the presence of a large parasitic resistance may be obtained from a C-V plot. Note, that the turn-on voltage (V_{to}) and threshold voltage (V_{th}) are two distinctly different quantities. V_{to} is the minimum external applied voltage required

to initiate conduction in the phosphor; the magnitude of V_{to} depends on the magnitude of the polarization charge (Q_{pol}). In contrast, V_{th} is independent of Q_{pol} ; it is the minimum external applied voltage necessary to initiate conduction without the assistance of any polarization charge stored in the interface [1]. The slope of the C-V curve is related to the pre-clamping density of interface states [2, 14, 16, 24] as follows,

$$Q_{ss} = \frac{C_i^2}{2qA} \frac{C_t}{C_p} \left[\frac{\Delta C}{\Delta V} \right]^{-1} \quad (3.4)$$

where C_i is the insulator capacitance, C_t is the total capacitance, C_p is the phosphor capacitance, and A is the area of the ACTFEL device.

If space charge generation is present in the ACTFEL device, an overshoot in the C-V curve may be observed. There are two kinds of overshoot commonly observed. (1) The insulator capacitance increases and saturates at a capacitance greater than that of the physical insulator capacitance. (2) The capacitance first increases to a value in excess of that of the physical insulator capacitance and subsequently decreases towards a value nearly equal to that of the physical insulator capacitance. According to a single sheet charge model developed by Keir *et al.* [13, 28], these two different kinds of overshoot are due to the magnitude of the characteristic field for impact ionization of deep-level traps (i.e. this is related to the energy depth of the traps). The characteristic field, and hence the energy depth of the trap, for the first kind of overshoot is less than that of the second kind.

3.4 Charge-External Voltage (Q-V) Analysis

A Q-V plot is generated by plotting the external charge monitored via the Sawyer-Tower circuit versus the external voltage. The sense element used in the Sawyer-Tower configuration is a 110.8 nF capacitor. The external charge, q_{ext} , is calculated from

$$q_{ext}(t) = C_{sense} v_3(t). \quad (3.5)$$

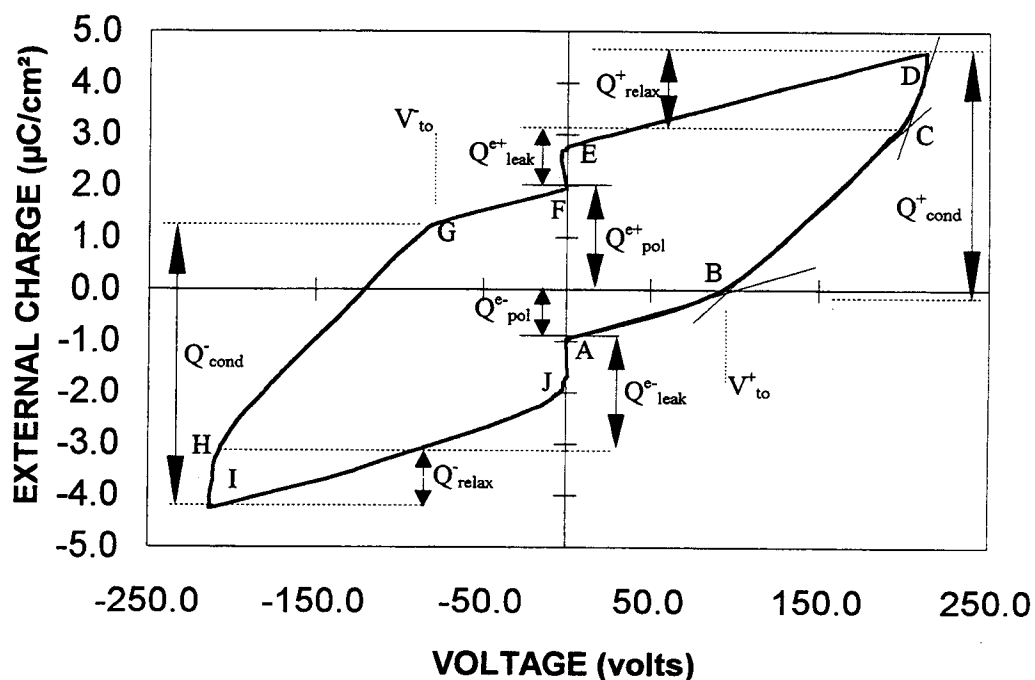


Figure 3-3: Q-V curve for an ALE ZnS:Mn ACTFEL device with ATO insulators.

A Q-V curve is then obtained by plotting q_{ext} versus the external applied voltage.

A typical Q-V curve is plotted in Fig. 3-3. The constant slope for voltages less than the turn-on voltage is equal to the total capacitance of the ACTFEL device since the dynamic capacitance is defined as

$$C = \frac{dQ}{dV}. \quad (3.6)$$

At a voltage larger than the turn-on voltage, conduction current begins to flow in the phosphor as the phosphor layer breaks down. This breakdown results in an increase in the measured capacitance which is manifest as an increase in the slope of the Q-V plot. The increased slope is due to the remaining capacitance of the top and bottom insulator layers in series. Also, the threshold voltage, turn-on voltage, leakage charge, relaxation charge, conduction charge and polarization charge can be obtained from a Q-V curve. For an evaporated ZnS:Mn ACTFEL device, the Q-V curve is symmetrical about the origin due to the absence of space charge generation, while an ALE ZnS:Mn ACTFEL device shows asymmetry due to the presence of the space charge generation near the interface at the ITO side. Further discussion of space charge generation is found in the next chapter.

3.5 Internal Charge-Phosphor Field (Q-F_p) Analysis

Q-F_p analysis provides direct information about the internal behavior of the ACTFEL device. Q-F_p analysis is accomplished using the Sawyer-Tower circuit shown in Fig. 3-1, where the sense element is a 110.8 nF capacitor, as in the case for Q-V analysis. The internal phosphor field, $f_p(t)$, is defined from Eq. (2b) of Brinquier's paper [26] and is given by

$$f_p = \frac{q - C_i v_g}{d_p (C_i + C_p)} \quad (3.7)$$

where d_p is the phosphor field thickness and C_i and C_p are the insulator and phosphor capacitances, respectively. v_g is the external applied voltage across the ACTFEL device, and is equal to $v_2(t) - v_1(t)$.

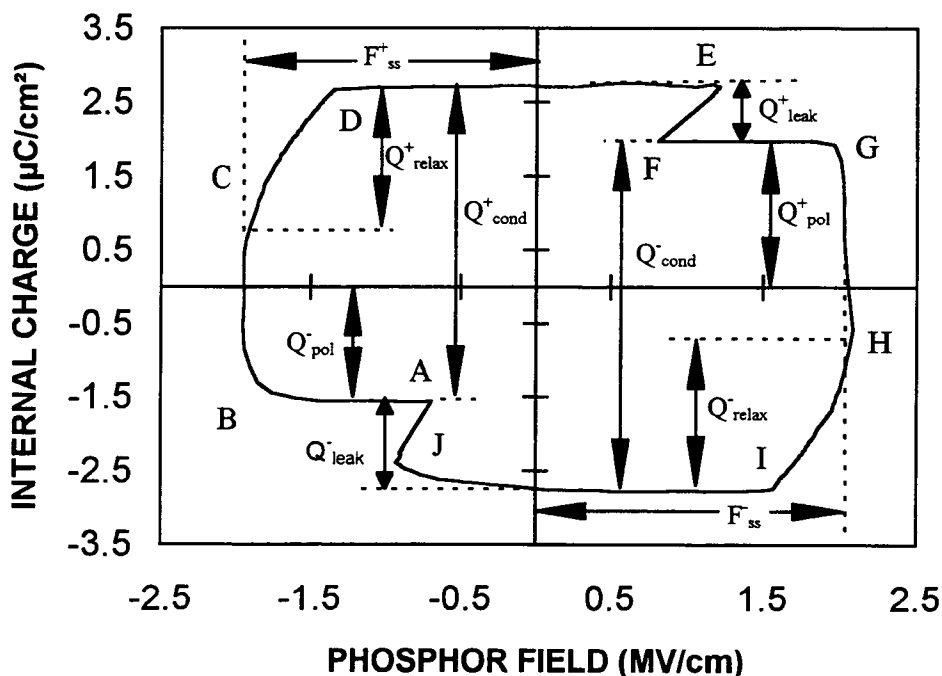


Figure 3-4: Q - F_p curve for an ALE ZnS:Mn ACTFEL device with ATO insulators.

q is the internal charge in the phosphor and is defined from Eq. (4) of

Bringuier's paper [26] as

$$q = \frac{C_i + C_p}{C_i} q_a - C_p v_g \quad (3.8)$$

where q_a is the external charge and is equal to $C_{sense}(t) \cdot v_3(t)$, as shown in Fig. 3-1.

Putting all this information into Eqns. (3.7) and (3.8) yields

$$q(t) = \frac{(C_i + C_p)}{C_i} C_{sense} v_3(t) - C_p [v_2(t) - v_3(t)] \quad (3.9)$$

$$f_p = \frac{1}{d_p} \left[\frac{C_{sense} v_3(t)}{C_i} - (v_2(t) - v_3(t)) \right]. \quad (3.10)$$

A Q-F_p curve is then obtained by plotting $q(t)$ versus $f_p(t)$ from Eqns. (3.9) and (3.10).

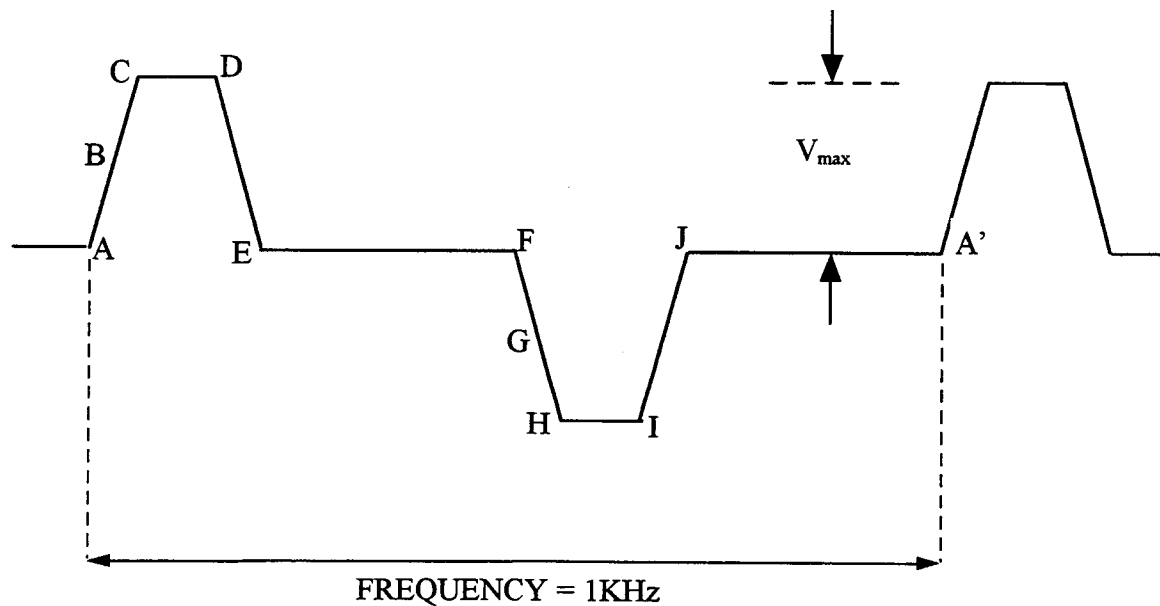


Figure 3-5: Symmetric bipolar pulse waveform used for ACTFEL electrical characterization.

A typical $Q-F_p$ curve for an ALE ZnS:Mn ACTFEL device is shown in Fig. 3-4. The labels A through J [2, 14, 16, 25] are used to designate certain points on the $Q-F_p$ curve; these points are also shown on a corresponding $Q-V$ curve and the standard symmetric bipolar pulse waveform, as indicated in Fig. 3-3 and Fig. 3-5, respectively. Superscripts + and - used in Figure 3-3 and 3-4 correspond to the polarity of the applied voltage pulse; a positive voltage pulse is defined as when the Al electrode bias is positive and a negative voltage pulse is defined as when the Al electrode bias is negative. The steady-state field, F_{ss} , corresponds to the phosphor field which is constant or approximately constant during the BC or GH portion of the applied voltage pulse. Q_{cond} is the conduction charge transported across the phosphor during the AD or FI portion of the applied voltage pulse; this is the charge responsible for impact excitation of luminescent impurities, which gives rise to light emission. Q_{pol} is the polarization charge stored at the phosphor/insulator interfaces just prior to the onset of the subsequent pulse of opposite polarity. Q_{leak} denotes the leakage charge arising from the emission of electrons from shallow interface states during the EF and JA' portion of the applied voltage pulse. Q_{relax} is the relaxation charge which flows across the phosphor during the CD or HI portion of the applied voltage pulse, during which the applied voltage is constant at its maximum value; the phosphor field relaxes during this period of the waveform.

3.6 How to Relate the Q-F_p Curve to the Applied Voltage Waveform

The points A and A' correspond to the onset of a positive voltage pulse applied to the Al electrode [2, 16, 14]. Non-zero values of $q(t)$ and $f_p(t)$ are observed at A and A' because of the polarization charge residing at the phosphor/insulator interfaces left behind by the previous pulse of negative polarity. The AB portion of the Q-F_p curve arises from the rising edge of the waveform when the voltage magnitude is less than the turn-on voltage of the ACTFEL device. The BC portion is still in the rising portion of the waveform, but the applied voltage magnitude is greater than that of the turn-on voltage. The field is constant or approximately constant during this portion of the waveform and is equal to F_{ss} . CD corresponds to the portion of the waveform in which the external voltage is held constant at its maximum amplitude, V_{max} . DE corresponds to the falling edge to the voltage pulse; the polarity of the field reverses during this portion of the waveform. EF corresponds to the segment of the waveform in which no external bias is applied to the ACTFEL device. The remainder of the Q-F_p curve from F to A' is similar to the A to F portion of the curve except that the external applied field is of negative polarity.

3.7 How to Estimate C_i and C_t by using Q-F_p Curves

For Q-F_p analysis, q and f_p both depend on C_i , as evident from Eqns. (3.10) and (3.11). The accuracy of a Q-F_p curve depends upon how well C_i is estimated. Three different kinds of capacitance are distinguished [27], as follows: (i) the actual, physical capacitance, (ii) the effective capacitance associated with a C-V measurement, and (iii) the

effective capacitance associated with a Q-F_p measurement. This distinction between these different kinds of capacitance is necessary because in ACTFEL devices which exhibit effects related to space charge generation (as do all of the ACTFEL devices tested in this study) the experimentally deduced capacitance is not identical to the actual, physical capacitance. Thus, C_i^{phys} and C_p^{phys} are denoted as the physical capacitance of the insulator layers and the phosphor layer, respectively; these capacitances are calculated from known values of the dielectric constant, the cross sectional area, A , and the layer thickness, d , via

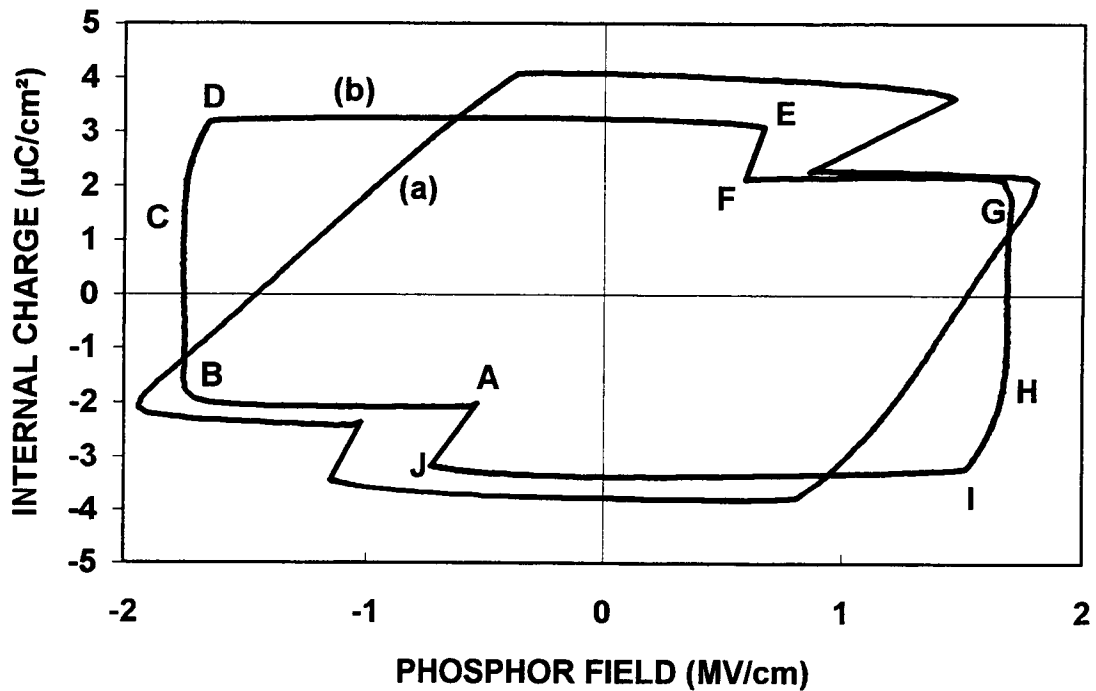


Figure 3-6: Q-F_p curves obtained using different values of C_i and C_t .

the parallel plate capacitor formula

$$C = \frac{\epsilon A}{d}. \quad (3.12)$$

From C_i^{phys} and C_p^{phys} , the physical capacitance of the total phosphor stack, C_t^{phys} is determined as

$$\frac{1}{C_t^{\text{phys}}} = \frac{1}{C_i^{\text{phys}}} + \frac{1}{C_p^{\text{phys}}}. \quad (3.13)$$

In contrast to the physical capacitances defined above, the insulator, phosphor, and total capacitance deduced via C-V analysis are denoted as C_i^{cv} , C_p^{cv} , and C_t^{cv} , respectively. C_i^{cv} and C_t^{cv} are determined directly from a C-V measurement whereas C_p^{cv} is calculated from an equation analogous to Eqn. (3.13). C_t^{cv} is usually found to agree with C_t^{phys} quite well, whereas C_i^{cv} and C_i^{phys} are distinctly different.

Finally, C_i^{qfp} and C_t^{qfp} are effective capacitances deduced experimentally from a fit to the Q-F_p curve. Figure 3-6 shows two Q-F_p curves. Curve (a) is generated using C_i^{phys} and C_p^{phys} in the Q-F_p equations; this leads to a Q-F_p curve which is severely distorted from the expected, ideal case. In contrast, curve (b) in Fig. 3-6 is a "normal-looking" Q-F_p curve. Curve (b) is obtained by allowing the values of C_i^{phys} and C_p^{phys} to be freely adjusted so that the resulting Q-F_p curve is as "normal-looking" as possible. Operationally in order to obtain C_i^{qfp} and C_t^{qfp} , a family of Q-F_p curves is plotted as function of C_t^{qfp} . C_t^{qfp} is chosen based on the value of C_t^{qfp} which yield the most horizontal AB/FG and DE/IJ sections of the Q-F_p curves. Next, a family of curves is plotted as a function of C_i^{qfp} . C_i^{qfp} is chosen based on the value of C_i^{qfp} which yields the most vertical BC/GH sections and the most horizontal AB/FG and DE/II sections of the Q-F_p curves. Sometimes it is

necessary to iterate several times in the fitting procedure to determine the optimal values of C_i^{qfp} and C_t^{qfp} .

3.8 Q_{max} - V_{max} Analysis

Q_{max} - V_{max} analysis is an electrical characterization technique which provides information indicating whether band-to-band impact ionization occurs in the phosphor during ACTFEL operation. Q_{max} may be defined as

$$Q_{max}^+ = Q_{cond}^+ - Q_{pol}^- \quad (3.14)$$

$$Q_{max}^- = Q_{cond}^- - Q_{pol}^+ \quad (3.15)$$

where Q_{max}^+ and Q_{max}^- refer respectively to a positive or negative voltage pulse applied to the Al electrode. Q_{max} is the net charge accumulated at the interface with respect to the flat band or charge neutral condition [2]. V_{max} is the maximum applied voltage to the ACTFEL device, as shown in Fig. 3-5. Originally, a Q_{max} - V_{max} curve was obtained by assessing Q_{max} values from various Q- F_p curves measured at different V_{max} 's [31]. It is very time consuming to plot a Q_{max} - V_{max} curve in this manner. This motivated Pham [2] to develop an automated procedure for performing a Q_{max} - V_{max} measurement; is now takes approximately two minutes to obtain a Q_{max} - V_{max} plot.

Two important pieces of information may be obtained from a Q_{max} - V_{max} curve [2]. First, the threshold voltage is defined as the intercept of the linear portion of a Q_{max} - V_{max} curve extrapolated to the V_{max} axis. The threshold voltage is usually found to be similar to the threshold voltage found in brightness-voltage (B-V) measurements. Second, the slope

[2, 31] of a Q_{\max} - V_{\max} curve defines a Q_{\max} - V_{\max} insulator capacitance, C_i^{qmax} . If C_i^{qmax} is greater than the physical insulator capacitance, C_i^{phys} , this is evidence that band-to-band impact ionization (i.e. electron-hole pair creation in the bulk region) occurs during the ACTFEL device operation [31].

Room temperature Q_{\max} - V_{\max} curves are obtained for “Thin”, “Normal”, and “Thick” ALE ZnS:Mn ACTFEL devices, as discussed in Chapter 4. The area of the test dots used is 0.0972 cm^2 .

3.9 Electrical Characterization of ALE ZnS:Mn ACTFEL Devices: Experimental Procedure

“Thin”, “Normal”, and “Thick” samples are electrically characterized at room temperature after a 24-hour aging process of the ACTFEL dots. C-V and Q- F_p curves are obtained for maximum applied voltage (V_{\max} 's) of 60, 80, 100, 120 V in excess of the threshold voltage, $V_{\text{th}}^{\text{BV}}$. $V_{\text{th}}^{\text{BV}}$ is defined as the minimum applied voltage at which an appreciable amount of light is observed by the human eyes. Al^+ and Al^- denote the applied voltage polarity with respect to the aluminum electrode.

The results of the electrical characterization of ALE ZnS:Mn ACTFEL device are discussed in Chapter 4, Section 3.

3.10 Electrical Characterization at Different Temperatures: Experimental Procedure

Electrical characterization of ALE ZnS:Mn ACTFEL devices as a function of temperature are accomplished using a Sun Systems environmental chamber. The Sun Systems environmental chamber is a high-quality digital temperature controller with built-in GPIB. The heater inside the environmental chamber is able to bring the temperature to 573 K (i.e. 300 C). Liquid nitrogen (LN₂) is used to cool the chamber to a minimum temperature of 80 K. There is no pump connected to the environmental chamber, so that it operates under atmospheric conditions.

Temperature-dependent analysis is performed only for the “Thick” sample since the goal of this experiment is to explore the space charge generation trends as a function of temperature; the “Thick” sample shows more space charge generation than the other samples (see Chapter 4, Section 1,2 and 3 for details).

The “Thick” sample is placed into the Sun System environmental chamber under atmospheric conditions. After electrical characteristics of the ALE ZnS:Mn ACTFEL device are collected at 300 K, the temperature is lowered to 200 K, and then to 100 K to collect electrical characteristics at these lower temperatures. Finally, the temperature is raised to 400 K to collect electrical data at a temperature above room temperature. No brightness or chromaticity data are measured during this experiment since the window of the Sun System environmental chamber fogs up during the low temperature portion of the experiment.

The results of the electrical characterization study of the “Thick” ALE ZnS:Mn ACTFEL device at various temperatures are presented in Chapter 4, Section 4.7.

3.11 Aging Studies of ALE ZnS:Mn ACTFEL Devices with Different Phosphor Layer Thicknesses at Different Temperatures: Experimental Procedure

As mentioned in the aging study performed by a previous OSU researcher, Abu-Dayah, evaporated ZnS:Mn ACTFEL devices [14] exhibit a very different aging mechanism than do ALE ZnS:Mn ACTFEL devices. Both Planar America and Planar International grow ZnS:Mn ACTFEL devices by ALE; therefore, there is a need for understanding the aging behavior of ALE ZnS:Mn ACTFEL device since they are widely used in monochrome EL flat panel displays.

Both "Thick" and "Normal" ALE ZnS:Mn ACTFEL devices are used in the aging studies since more space charge generation is observed in these samples than in the "Thin" sample, as shown in Tables 4.1 and 4.2 in Chapter 4. The waveform used in this study is described in Fig. 3-5, and V_{\max} is 210 V for the "Normal" sample, and 230 V for the "Thick" sample.

Aging studies at $-10\text{ }^{\circ}\text{C}$, $27\text{ }^{\circ}\text{C}$, and $52\text{ }^{\circ}\text{C}$ are performed using both "Normal" and "Thick" samples. Several high temperatures were tried in this aging study. When the sample was placed in an environmental chamber at $100\text{ }^{\circ}\text{C}$, the test dot only operated for 6 hours. When the temperature was $77\text{ }^{\circ}\text{C}$, the test dot operated for 15 hours or so. Finally, if the maximum temperature was maintained $52\text{ }^{\circ}\text{C}$, the test dot was found to operate for 24 hours or more during the aging experiment.

Several cold temperatures were tried in this aging study. If a temperature of $-100\text{ }^{\circ}\text{C}$ or $-50\text{ }^{\circ}\text{C}$ was used, the test dots were destroyed. Water vapor is suspected to cause the destruction of the test dots since the environmental chamber operates at

atmospheric conditions and water vapor was present in the chamber. Finally, if a minimum temperature of $-10\text{ }^{\circ}\text{C}$ was used, the test dot was found to operate during the entire aging experiment.

During the aging experiment, Q-F_p and C-V data are taken at the same time using a 110.8 nF sense capacitor. The general C-V trends using a sense capacitor are similar to C-V trends using a sense resistor except that the C-V curves obtained using the sense capacitor are smoother due to the low pass filtering action of the sense capacitor. This filtering of the C-V curve due to the sense capacitor is achieved at a cost, however, since some of the C-V information associated with the abruptness of the C-V transition is lost.

The results of the variable-temperature aging study are presented in Chapter 4, Section 9.

Chapter 4 Electrical Characterization of ALE ZnS:Mn ACTFEL Devices

4.1 Introduction

The explanation for light emission in an ACTFEL device presented in Chapter 2 assumes the absence of space charge generation within the ZnS bulk; consequently, the electrical field across the phosphor is constant. This assumption of no space charge generation can adequately explain the performance of evaporated ZnS:Mn ACTFEL devices. In order to explain the asymmetrical behavior of ALE ZnS:Mn ACTFEL devices, the concept of asymmetrical space charge generation [28, 32] in the phosphor layer is required.

This chapter contains a discussion of several topics related to the electrical characterization of ALE ZnS:Mn ACTFEL devices:

- (1) A discussion of the origin of space charge generation.
- (2) A presentation of the results of a study of the electrical characteristics of ALE ZnS:Mn ACTFEL devices in which the phosphor layer thickness is varied. Advantages and disadvantages of space charge generation are then discussed.
- (3) A presentation of the results of a study of the electrical characteristics of ALE ZnS:Mn ACTFEL devices at different temperatures (i.e. 100 K, 200 K, 300 K, and 400 K).
- (4) A comparison of Q_{\max} - V_{\max} results to results obtained using other electrical characterization methods.

(5) A presentation of the results of an aging study of ALE ZnS:Mn ACTFEL devices with different phosphor thicknesses at different temperatures (i.e. 263 K, 300 K, and 325 K).

4.2 The Origin of Space Charge Generation

Space charge generation modeling [13] presumes that the creation of space charge in the phosphor of an ACTFEL devices is due to impact ionization of deep-level traps. A mechanism involving impact ionization of deep-level traps is presented as follow.

It has been proposed [14, 27] that the origin of space charge generation in ALE ZnS:Mn ACTFEL devices is associated with impact ionization of the zinc vacancy portion of chlorine-zinc vacancy self-activated defect complexes. Chlorine is identified as the coactivator which complexes with a zinc vacancy since the aluminum, zinc, and manganese ALE process gases are all chlorides.

According to a proposed thermodynamic argument [27, 29], as more chlorine donors are incorporated into the ZnS, the Fermi level is pushed towards the conduction band. The shift of the Fermi level makes the creation of a zinc vacancy more energetically favorable, instead of ionization of donor electrons to the conduction band. This process of compensating shallow donors or acceptors via the creation of vacancies is referred to as self-compensation. Zinc vacancy creation via self-compensation is thermodynamically favorable when a moderate concentration of chlorine is present in the ZnS. Evidence for space charge generation via impact ionization of zinc vacancies in ALE ZnS:Mn ACTFEL devices which are grown using chlorine-containing process gases is proposed [1, 5, 27].

Evaporated ZnS:Mn ACTFEL devices do not exhibit evidence for space charge generation since evaporation process is a chlorine-free process.

4.3 Electrical Characterization of ALE ZnS:Mn ACTFEL Device with Variable Phosphor Thicknesses

Table 4.1: A comparison of the insulator and total capacitance (nF/cm^2) of the Thin, Normal, and Thick ALE ZnS:Mn ACTFEL devices.

	Physical Capacitance	C-V		Q-F _p	
		Al ⁺	Al ⁻	Al ⁺	Al ⁻
Thin, V _{th} = 100 V					
Insulator Capacitance (C _i)	23	27	27	26	27
Total Capacitance (C _t)	13	11	11	13	13
Normal, V _{th} = 123 V					
Insulator Capacitance (C _i)	22	38	38	38	37
Total Capacitance (C _t)	8	9	9	9	9
Thick, V _{th} = 163 V					
Insulator Capacitance (C _i)	20	39	39	44	44
Total Capacitance (C _t)	6	6	6	7	7

The experimental results of an electrical characterization study of pre-aged dots of the samples denotes “Thick”, “Normal”, and “Thin” are summarized in Table 4.1. As indicated in Table 4.1, the insulator and total capacitances, as estimated from the known physical thicknesses and dielectric constants, are compared to estimates which are deduced experimentally from C-V and Q-F_p measurements. From Table 4.1 it is evident that there is fairly good agreement between the total capacitances C_t^{phys} , C_t^{cv} and C_t^{qfp} . In

Table 4.2: A comparison of the ratio of the effective insulator capacitance as deduced by C-V or Q-F_p measurements to the calculated physical insulator capacitance.

Capacitance Ratio	Applied Voltage Polarity	Thin	Normal	Thick
C_i^{C-V}/C_i^{phys}	Al ⁺	1.2	1.7	2.0
	Al ⁻	1.2	1.7	2.0
C_i^{qfp}/C_i^{phys}	Al ⁺	1.1	1.7	2.2
	Al ⁻	1.2	1.7	2.2

contrast, there are significant differences between C_i^{phys} and the insulator capacitances deduced from electrical measurements (i.e. C_i^{cv} , and C_i^{qfp}) and these differences become more pronounced as the thickness of the phosphor increases. These differences between

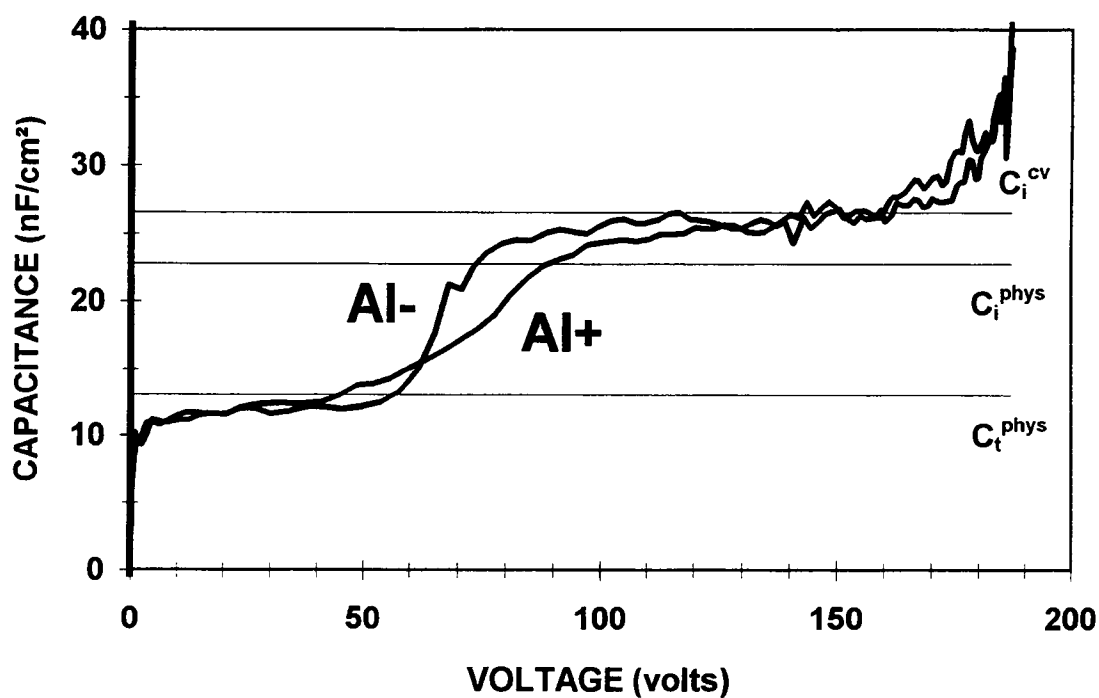


Figure 4-1: C-V curves for a "Thin" ALE ZnS:Mn ACTFEL device for both applied voltage polarity.

the physical insulator capacitance and that deduced from electrical measurements are more clearly indicated in Table 2 where the ratio of the insulator capacitance determined

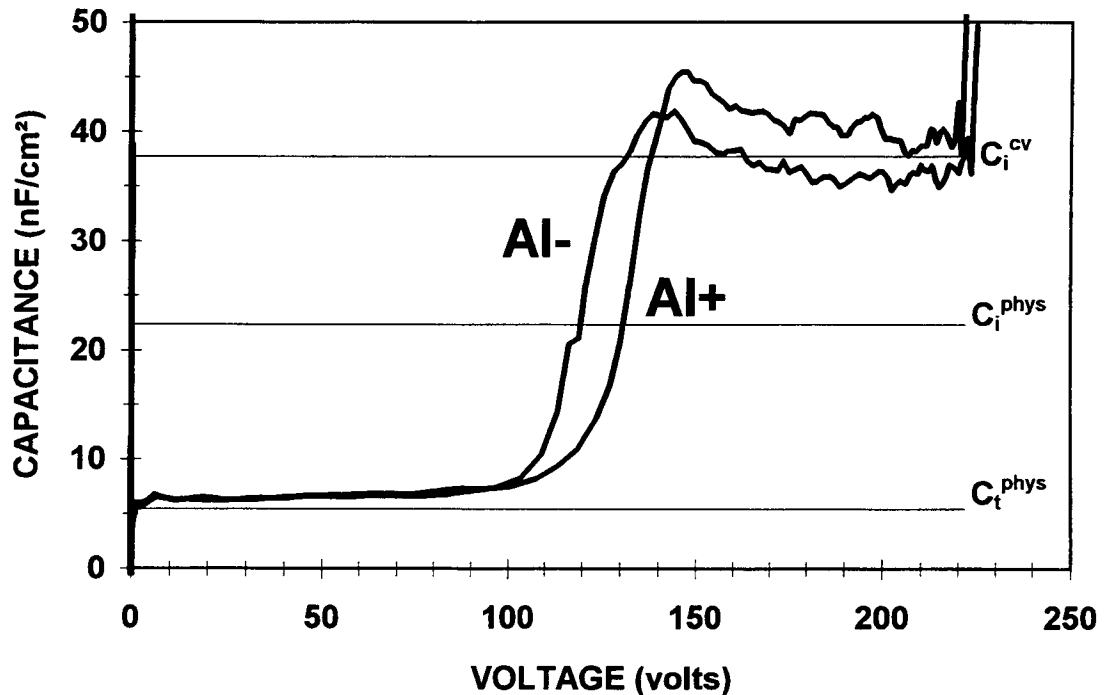


Figure 4-2: C-V curves for a "Thick" ALE ZnS:Mn ACTFEL device for both applied voltage polarities.

experimentally from C-V or Q-F_p measurements to the physical insulator capacitance is tabulated for the three ALE ZnS:Mn ACTFEL samples; these insulator capacitance ratios are tabulated also as a function of the applied voltage polarity. The message of Table 4.2 is that the capacitance ratio increases with increasing phosphor thickness; this trend is attributed to an increasing amount of space charge generation with increasing phosphor thickness.

Table 4.1 and 4.2 do not provide any indication of the asymmetrical nature of the electrical characteristics of the ALE ZnS:Mn ACTFEL devices employed in this study. Evidence for asymmetry is illustrated in Figs. 4-1 and 4-2 in which the C-V curves for both polarities are shown for the "Thin" and "Thick" ACTFEL devices, respectively. As shown in Figs. 4-1 and 4-2, a polarity-dependent asymmetry is observed for both samples.

From the data shown in Table 4.2, the insulator capacitance, as deduced from C-V and Q-F_p analysis, is greater than the calculated physical insulator capacitance. This implies that space charge creation occurs in the phosphor layer of these ACTFEL devices during device operation. Other evidence for space charge generation is witnessed in the raw experimental data as:

(1) Overshoot in the C-V characteristics. As shown in Figs. 4-1 and 4-2, two types of overshoot are observed; in the first case (i.e. Fig. 4-1) the capacitance increases and saturates at a value greater than that of the physical insulator capacitance, whereas in the second case (i.e. Fig. 4-2) the capacitance first increases to a value in excess of that of the physical insulator capacitance and subsequently decreases towards a value nearly equal to, or a bit larger than that of the physical insulator capacitance.

(2) Q-F_p distortion, as shown in Figs. 3-6 and 4-3. Figure 3-6 illustrates the dramatic nature of Q-F_p distortion if physical capacitances are employed in the Q-F_p equations. Figure 4-3 shows several Q-F_p curves obtained at various maximum applied voltages for the "Thin" ACTFEL device. The Q-F_p curves shown in Fig. 4-3 are obtained by fitting the insulator and total capacitances but still exhibit a slight amount of overshoot and a lack of

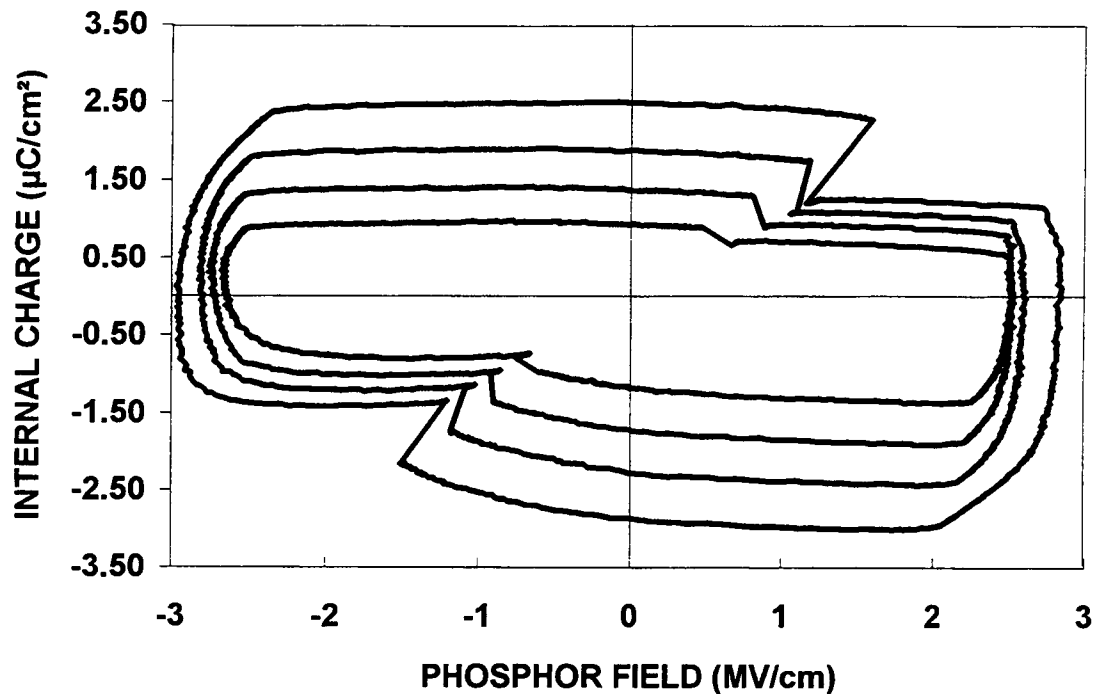


Figure 4-3: Q-Fp curves for a "Thin" ALE ZnS:Mn ACTFEL device.

field-clamping, both of which are further evidence for space charge generation during ACTFEL operation.

4.4 Advantages and Disadvantages of Space Charge Generation

The primary experimental finding is that the thicker the phosphor in an ALE ZnS:Mn ACTFEL device, the more space charge generation occurs within the phosphor during device operation. Space charge generation is a mixed blessing. The primary disadvantage of the thicker ACTFEL devices is that the threshold voltage increases with

increasing phosphor thickness, as is evident from Table 4.1. However, there are advantages of having space charge generation occur during ACTFEL operation.

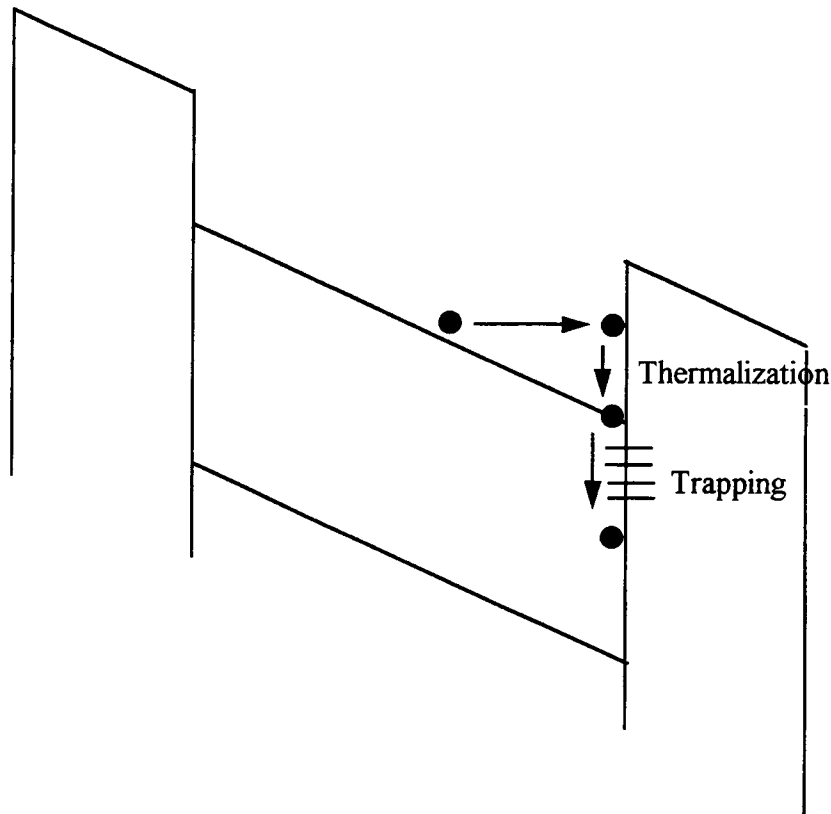


Figure 4-4: Energy band diagram for an ACTFEL device without any space charge generation in the phosphor layer.

The first advantage has to do with the aging stability of ACTFEL devices with space charge generation. To see this, first consider the energy band diagram shown in Fig. 4-4 for a phosphor with no space charge (so that the slope of the energy band is constant in the phosphor and insulator layers) which shows an electron in the phosphor conduction band impinging at the phosphor/insulator conduction band discontinuity. If there is indeed no space charge generation in the ZnS:Mn ACTFEL device the phosphor field is constant with a magnitude of about 1.75 MV/cm; thus, a significant number of the electrons which

impinge upon the conduction band discontinuity are significantly heated. For these hot electrons to subsequently be trapped at interface states, they must dissipate a significant amount of thermalization energy to reach the bottom of the phosphor conduction band at the interface in addition to the energy that they must dissipate in the process of undergoing interface state trapping. Most of this energy is dissipated as phonons in a very thin region of the device near the interface. It is likely that such a localized phonon dissipation process would lead to local heating of the lattice and multiphonon emission [33] such that interfacial interdiffusion occurs; this process of enhanced interdiffusion due to localized phonon dissipation has been proposed [34] as an aging mechanism for evaporated ZnS:Mn ACTFEL devices.

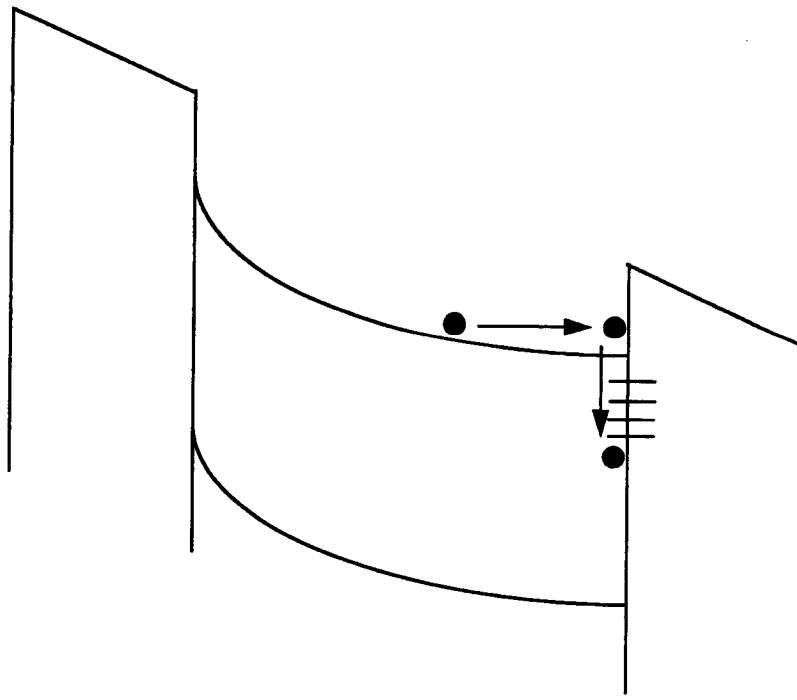


Figure 4-5: Energy band diagram for an ACTFEL device with space charge generation in the phosphor layer.

In contrast to the constant electric field case shown in Fig. 4-4, consider Fig. 4-5, in which space charge generation occurs and the electric field is not constant across the phosphor. In this case, the slope of the energy bands is large (i.e. large electric field) near the cathode interface from where electrons are injected but the energy bands are rather flat (i.e. small electric field) near the anode due to the creation of positive space charge which arises from space charge generation. Thus, electrons which impinge at the anode phosphor/insulator interface are much cooler and dissipate much less thermal energy at the interface so that less interdiffusion occurs.

4.5 Q_{\max} - V_{\max} Measurements

Table 4.3 is a comparison of the threshold voltage obtained from a Q_{\max} - V_{\max} measurement (i.e. $V_{\text{th}}^{\text{qmax}}$) and from an observation of the minimum voltage for light emission (i.e. $V_{\text{th}}^{\text{BV}}$). C_i^{qmax} and C_i^{phys} are also compared in Table 4.3. From Table 4.3, it is clear that the measured $V_{\text{th}}^{\text{qmax}}$'s are very close to the measured $V_{\text{th}}^{\text{BV}}$'s. This good correlation between $V_{\text{th}}^{\text{qmax}}$ and $V_{\text{th}}^{\text{BV}}$ is a further demonstration that a Q_{\max} - V_{\max} measurement is an electrical analog of the B-V measurement. The measured values of C_i^{qmax} are slightly larger than C_i^{qfp} , as tabulated in Table 4.1, and are much larger than C_i^{phys} . This observation implies that band-to-band impact ionization occurs in these three ACTFEL devices. However, it is possible that this large magnitude of C_i^{qmax} is primarily due to trap-to-band impact ionization, which appears to be the mechanism responsible for space charge generation in ALE ZnS:Mn ACTFEL devices. More work is required to

determine whether band-to-band impact ionization indeed occurs in these ALE ZnS:Mn ACTFEL devices. This good agreement between the electrically- and optically-assessed threshold voltages indicates that electrical processes (e.g. electron injection, transport, impact excitation).

Table 4.3: A comparison of the threshold voltage obtained from a $Q_{\max}-V_{\max}$ measurement (i.e. $V_{\text{th}}^{\text{qmax}}$) and from an observation of the minimum voltage for light emission (i.e. $V_{\text{th}}^{\text{BV}}$) and a comparison of C_i^{qmax} and C_i^{phys} .

		Minimum Voltage to start light emission (V)	Threshold Voltage from $Q_{\max}-V_{\max}$ (V)	Slope of $Q_{\max}-V_{\max}$ curve (nF/cm ²)	Physical Insulator Capacitance (nF/cm ²)
Thin	Al+	105	112	28.66	23
	Al-		112	25.63	
Normal	Al+	135	136	40.27	22
	Al-		135	40.27	
Thick	Al+	172	179	46.72	20
	Al-		179	47.22	

primarily determine the threshold voltage rather than optical processes (e.g. radiative recombination and optical outcoupling). Also, note, that $V_{\text{th}}^{\text{BV}}$ in Table 4.3 is slightly

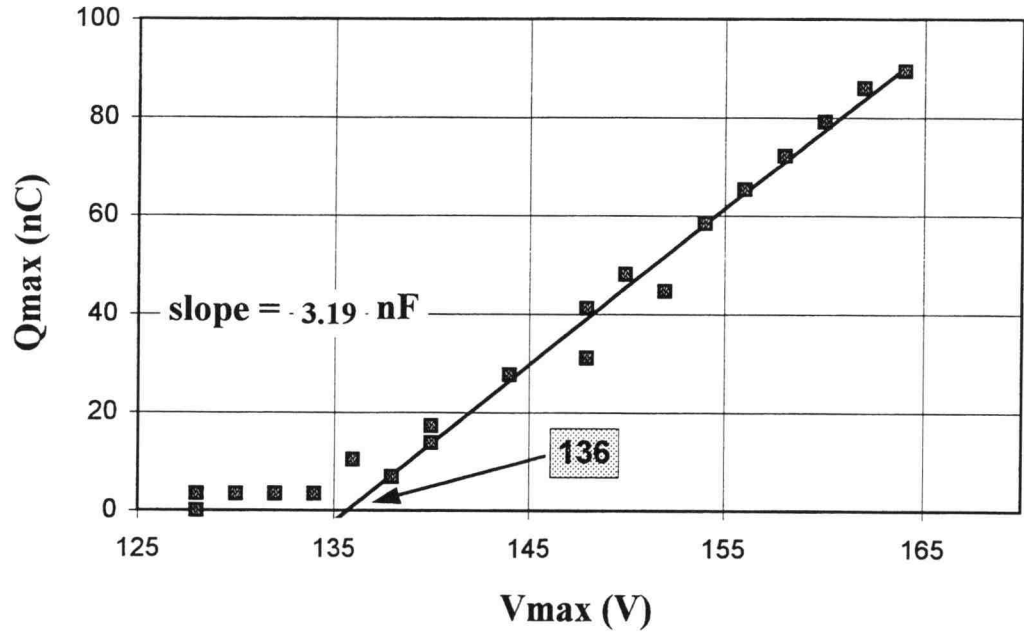


Figure 4-6: Q_{max} - V_{max} curve of positive polarity applied to Al electrode of "Normal" sample.

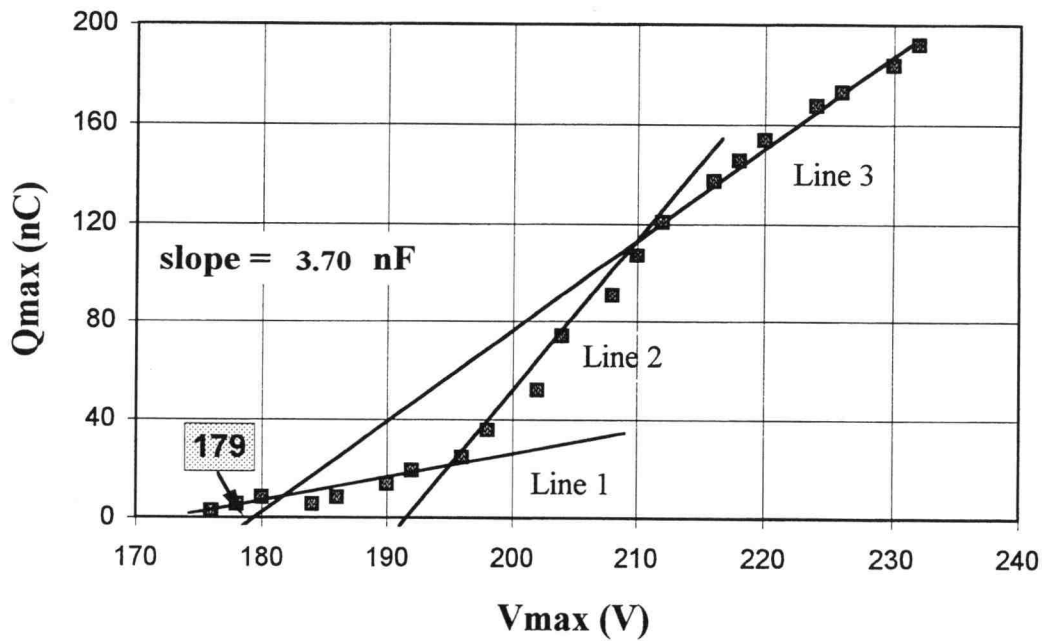


Figure 4-7: Q_{max} - V_{max} curve of positive polarity applied to Al electrode of the "Thick" sample.

Table 4.4 A comparison of the slopes and intercepts of the Q_{\max} - V_{\max} regression lines for a positive polarity voltage applied to the "Thick" sample (see Figs. 4-6 and 4-7).

	Slope of Q_{\max} - V_{\max} regression line (nF/cm ²)	V_{\max} intercept (V)
First regression line	12.63	174
Second regression line	75.37	192
Third regression line	46.72	179

larger than V_{th} reported in Table 4.1, even though these thresholds are estimated in the same manner. This disagreement is due to the fact that V_{th}^{BV} are assessed at different regions of that sample.

Figures 4-6 and 4-7 show Q_{\max} - V_{\max} curves for the "Normal" and "Thick" samples with a positive polarity voltage pulse applied to the Al electrode. Q_{\max} - V_{\max} curves for the negative polarity voltage pulse are very similar to those of positive polarity. For the normal sample, a linear regression fit to the linearly increasing portion of the Q_{\max} - V_{\max} curve provides a relatively straight forward and unique estimate of V_{th}^{qmax} . The single linear regression fit shown in Fig. 4-6 is fairly typical of "Thin", "Normal", and thiogallate [2] samples. In contrast, it is possible to fit three regression lines to the Q_{\max} - V_{\max} curve of the "Thick" sample as shown in Fig. 4-7. The more complex behavior of the Q_{\max} - V_{\max} curve shown in Fig. 4-7 is undoubtedly related to space charge generation, although the details of how space charge generation causes such Q_{\max} - V_{\max} features are not yet understood. The slopes and V_{\max} intercepts of these three regression lines are compared in

Table 4.4. Recall that the physical insulator capacitance, C_i^{phys} , of this “Thick” sample is 20 nF/cm². Note that slope of the first regression line is less than that of the C_i^{phys} whereas the slope of the other two regression lines are significantly greater than that of C_i^{phys} . Perhaps trends in the slope of the regression lines indicate that very little impact ionization occurs at the smaller V_{max} 's above threshold, but it then increases at larger V_{max} 's. Again, more work is required to understand these $Q_{\text{max}}-V_{\text{max}}$ features for the “Thick” ALE ZnS:Mn ACTFEL device. Note that the third linear regression fit at the largest V_{max} 's is used as an estimate of $V_{\text{th}}^{\text{qmax}}$ and C_i^{qmax} for Table 4.3.

4.6 Electrical Characterization of ALE ZnS:Mn ACTFEL Devices as a Function of Temperature

The results of electrical characterization of the “Thick” ALE ZnS:Mn ACTFEL device as a function of temperatures are presented in Figs. 4-8 to 4-19. The “Thick” sample is chosen for this study since it exhibits the largest amount of space charge generation. Experimental procedure details of this study are found in Chapter 3, Section 10.

Both C_i^{cv} and C_i^{qfp} are plotted as a function of temperature in Fig. 4-8. C_i^{cv} is estimated as the minimum insulator capacitance from the C-V curves shown in Figs. 4-9 and 4-10. C_i^{qfp} is obtained using the curve fitting technique discussed in Chapter 3, Section 7. The trends shown in Fig. 4-8 are a very clear indication that the insulator capacitance of the positive polarity is always greater than that of the negative polarity, and that the

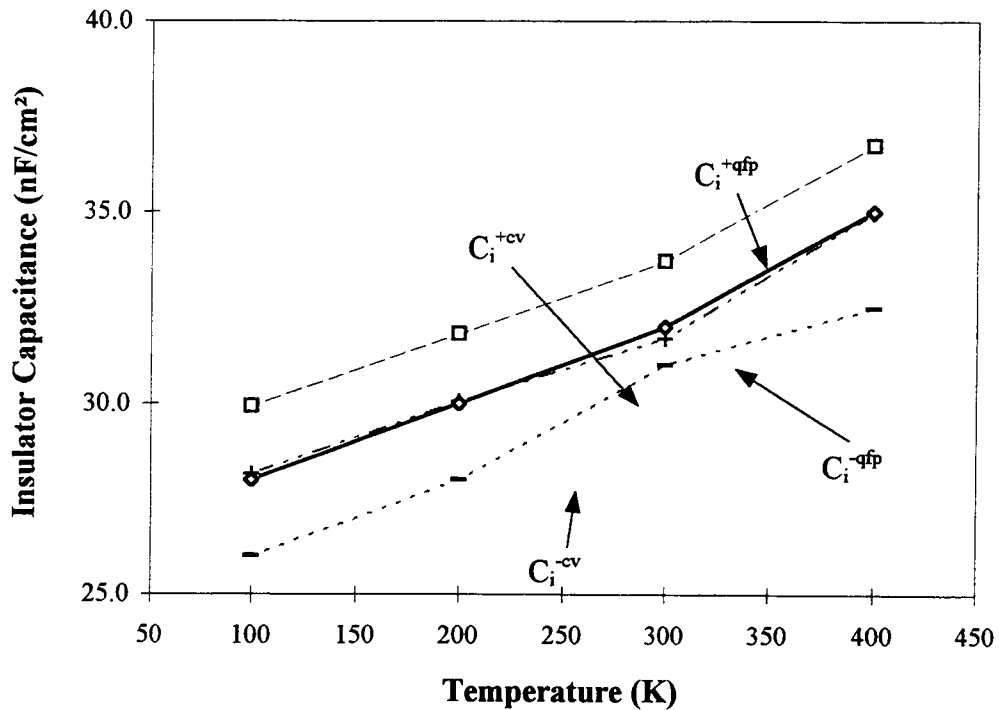


Figure 4-8: Insulator capacitance measured from C-V and Q-F_p curves as a function of temperature for the "Thick" ALE ZnS:Mn ACTFEL device.

insulator capacitance of both voltage polarities increases with increasing temperature. Also note that there is a moderate amount of voltage asymmetry in the temperature-dependent C-V curves shown in Figs. 4-9 and 4-10. Finally, Figs. 4-9 and 4-10 display a softening of the C-V curves in the V_{to1} region at higher temperature. The increase in insulator capacitance with temperature is attributed to space charge generation. The softening of the C-V curves near V_{to1} indicates that additional charge is sourced primarily from the phosphor bulk and not from the phosphor/insulator interface. The C-V asymmetry suggests that the space charge generation occurs nonuniformly across the phosphor. Since the negative polarity insulator capacitance found from C-V and Q-F_p measurements is

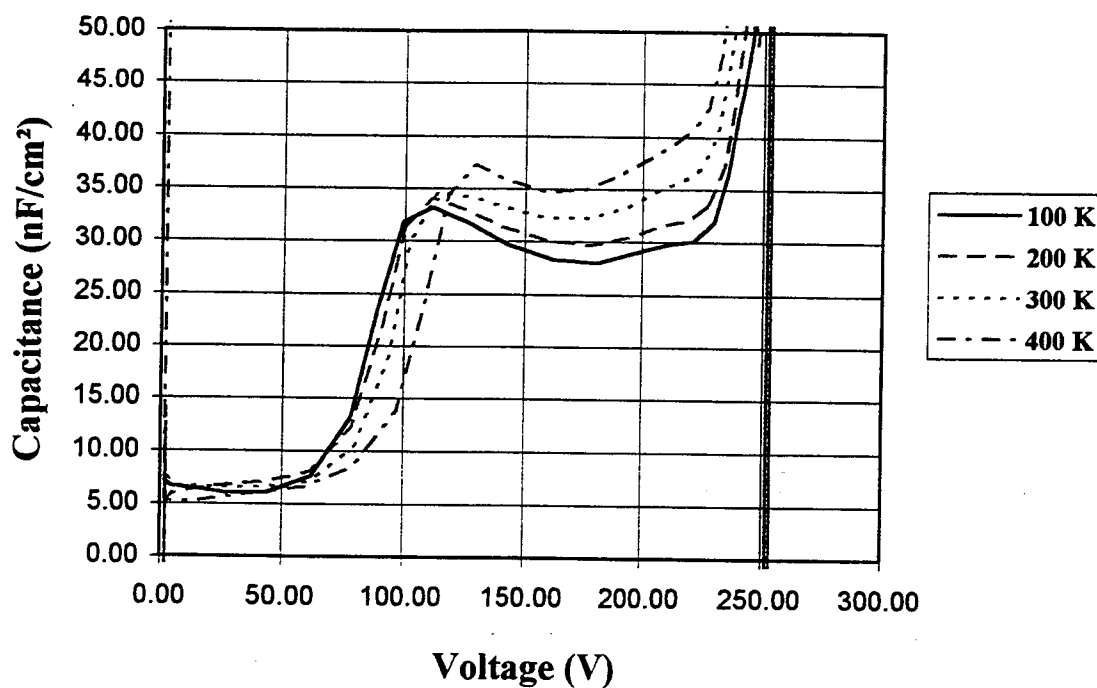


Figure 4-9: C-V curves as a function of temperature for the "Thick" ALE ZnS:Mn ACTFEL device when the Al electrode is positively biased.

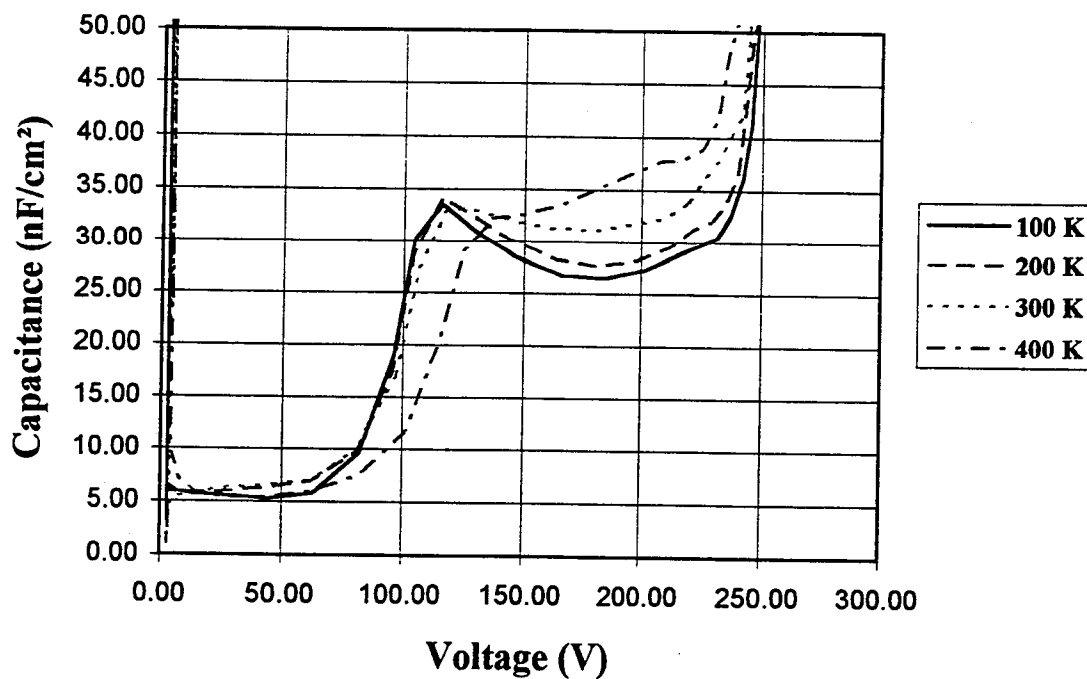


Figure 4-10: C-V curves as a function of temperature for the "Thick" ALE ZnS:Mn ACTFEL device when the Al electrode is negatively biased.

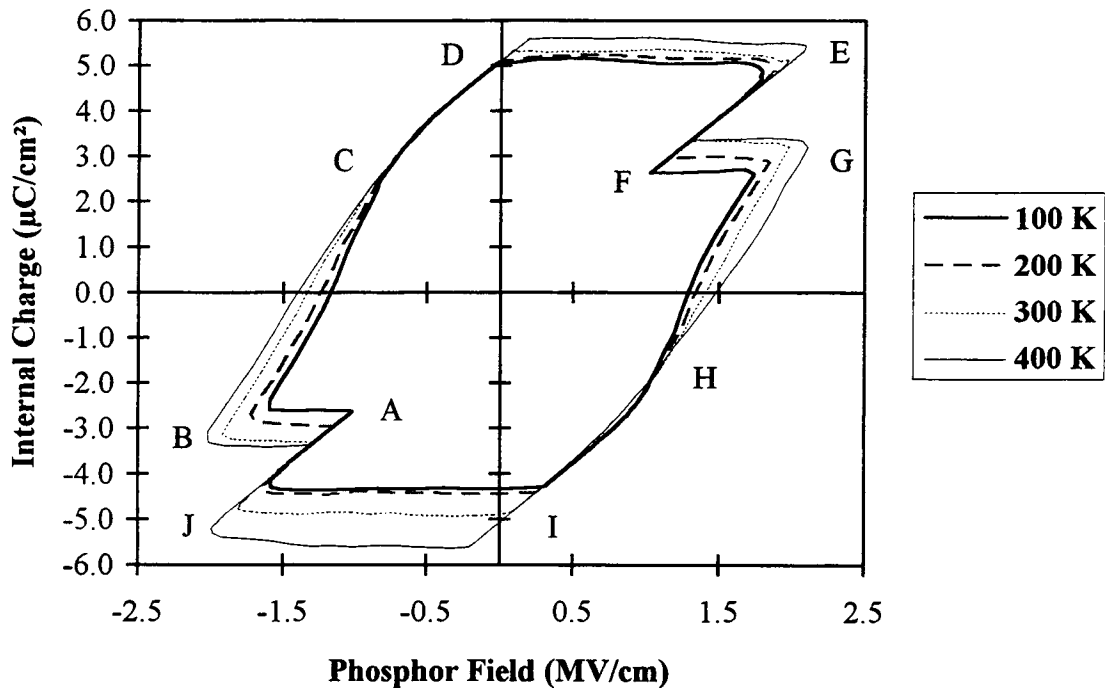


Figure 4-11: "Offset-adjusted" $Q-F_p$ curves as a function of temperature for the "Thick" ALE ZnS:Mn ACTFEL device. These curves are generated using C_i^{phys} and C_p^{phys} in the $Q-F_p$ equations.

greater than that of the positive polarity, the centroid of space charge generation occurs closer to the Al electrode phosphor/insulator interface.

Figure 4-11 presents $Q-F_p$ curves as a function of temperature plotted using the physical insulator and phosphor capacitance in the $Q-F_p$ equations (i.e. Eqns. (3.9) and (3.10)). Although these curves are distorted compared to evaporated ZnS:Mn ACTFEL devices which exhibit no space charge generation, some useful trends are still evident from these curves. First, note that the peak fields near point B and G increase monotonically with temperature. Second, the conduction charge increases with increasing temperature.

Third, the polarization charge and polarization field near point A and F increase monotonically with increasing temperature.

Note that the $Q-F_p$ curves shown in Fig. 4-11 are all “offset-adjusted”. The nature of this offset adjustment is indicated Fig. 4-12. The voltage transients measured across a sense capacitor for certain ACTFEL devices are found to be asymmetrical about the

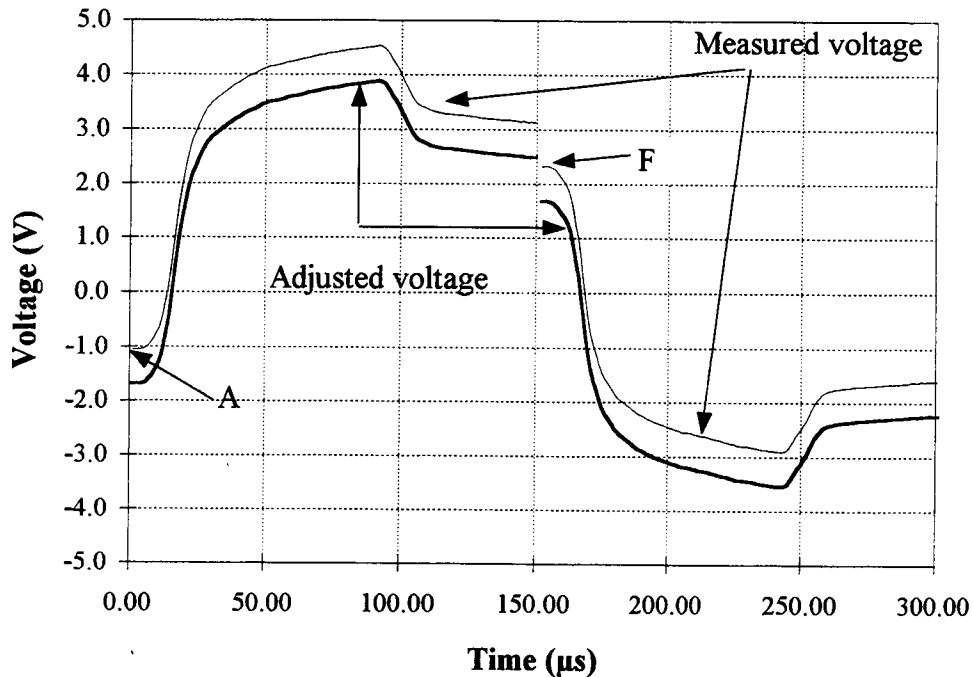


Figure 4-12: Voltage transients measured across the sense capacitor and after “offset-adjustment”.

voltage axis. This voltage asymmetry, or offset, is evident as a difference in the magnitudes of the voltages at the A and F points indicated in Fig. 4-12. A and F are points in the transient voltage waveform which occur just prior to the onset of an applied voltage pulse. “Offset adjustment” is accomplished by shifting the sense capacitor voltage transient curve until points A and F are equidistant from the voltage axis origin.

Figure 4-13 shows the offset voltage as a function of temperature. It is clear from Fig. 4-13 that the amount of offset increases with increasing temperature; the offset

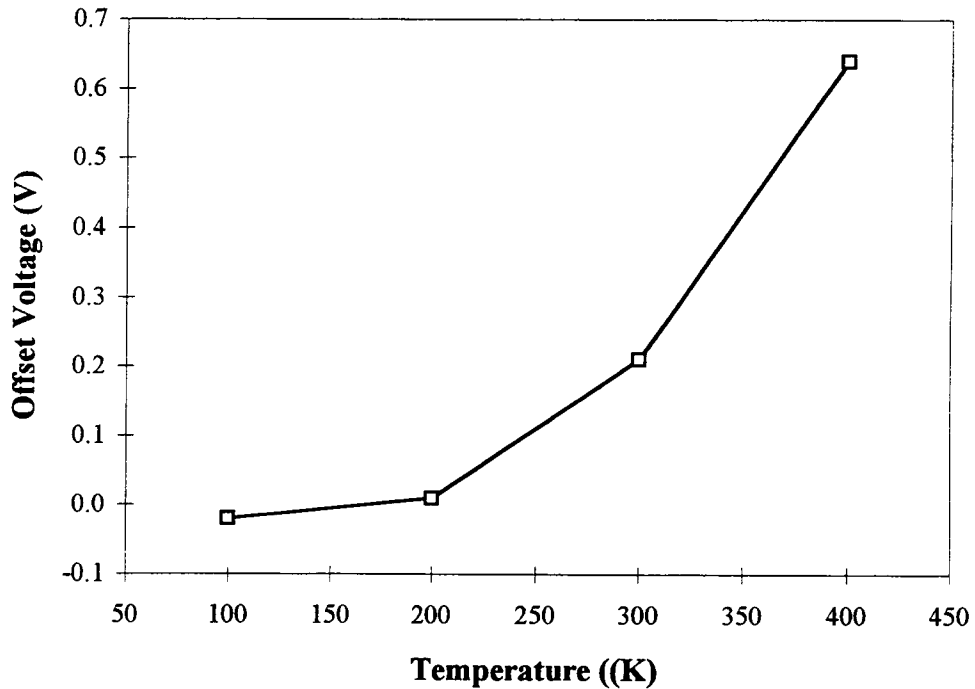


Figure 4-13: Offset voltage versus temperature for the “Thick” ALE ZnS:Mn ACTFEL device.

voltage increase is particularly large at the higher temperatures. This observation is important since space charge generation using a single sheet charge model [28] indicates that such a voltage offset arises from asymmetrical generation of space charge within the phosphor. Note that if Fig. 4-11 is not offset adjusted, the Q - F_p curves shown in Fig. 4-11 would be offset upward and to the right due to the positive voltage offset shown in Fig. 4-12. Also note that Q - V as well as Q - F_p curves are subject to this offset. Finally, note that Q_{pol} and F_{ss} are very sensitive to voltage offset, while Q_{cond} , Q_{relax} , and Q_{leak} are independent of voltage offset.

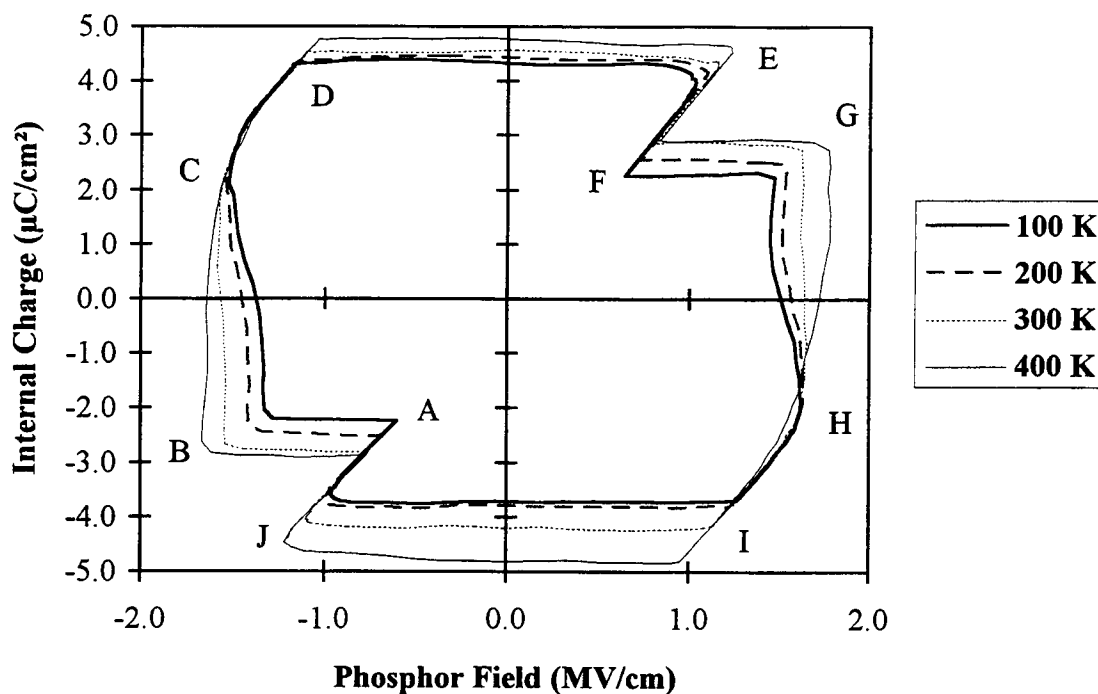


Figure 4-14: "Offset-adjusted" Q - F_p curves as a function of temperature for the "Thick" ALE ZnS:Mn ACTFEL device. These curves are generated using C_i^{qfp} and C_p^{qfp} in the Q - F_p equations.

Figure 4-14 presents "offset-adjusted" Q - F_p curves which are obtained using the Q - F_p fitting procedure in which the effective insulator and total capacitances give rise to the most horizontal DE/IJ segments and the most vertical BC/GH segments of the Q - F_p curves. From Fig. 4-14 Q_{cond} , Q_{relax} , Q_{pol} , F_{ss} , and Q_{leak} are plotted as a function of temperature in Figs. 4-15 through 4-19.

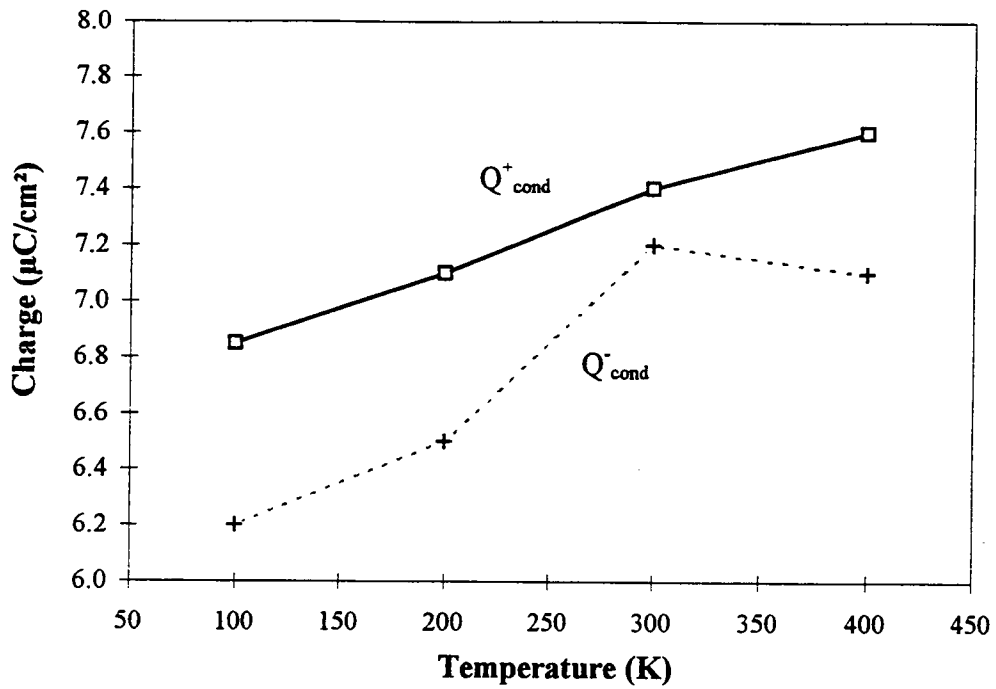


Figure 4-15: Q_{cond} versus temperature for the "Thick" ALE ZnS:Mn ACTFEL device.

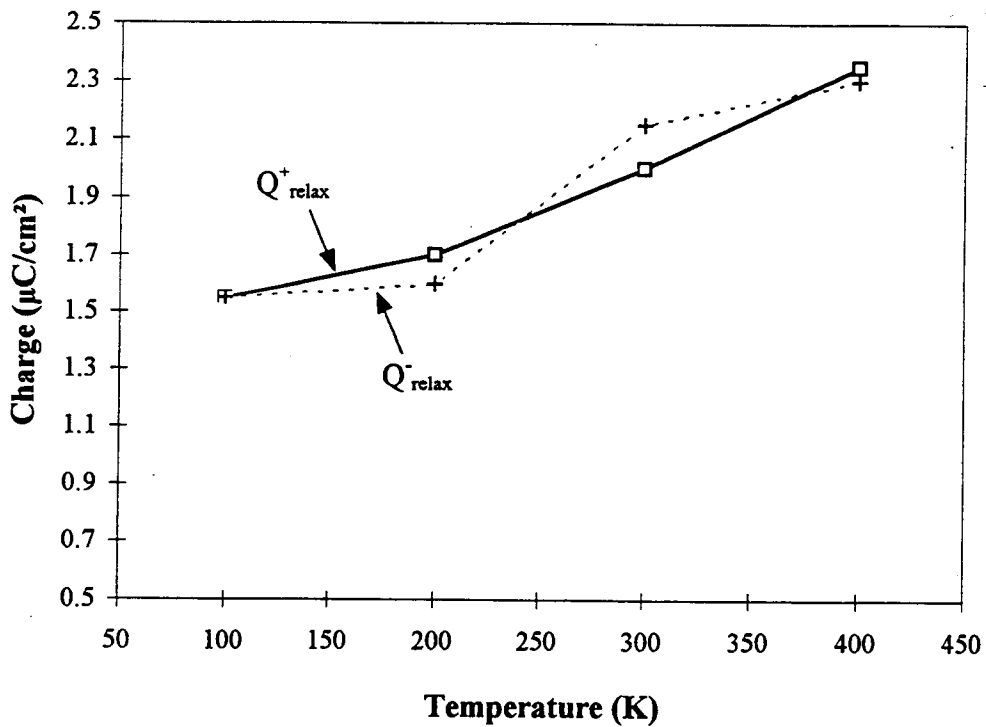


Figure 4-16: Q_{relax} versus temperature for the "Thick" ALE ZnS:Mn ACTFEL device.

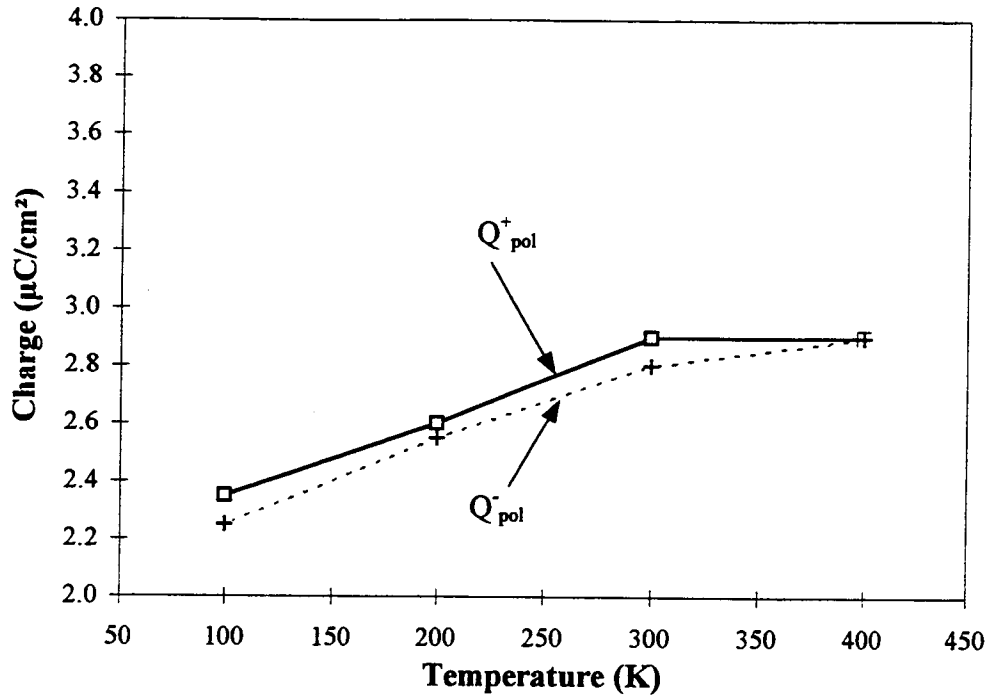


Figure 4-17: Q_{pol} versus temperature for the "Thick" ALE ZnS:Mn ACTFEL device.

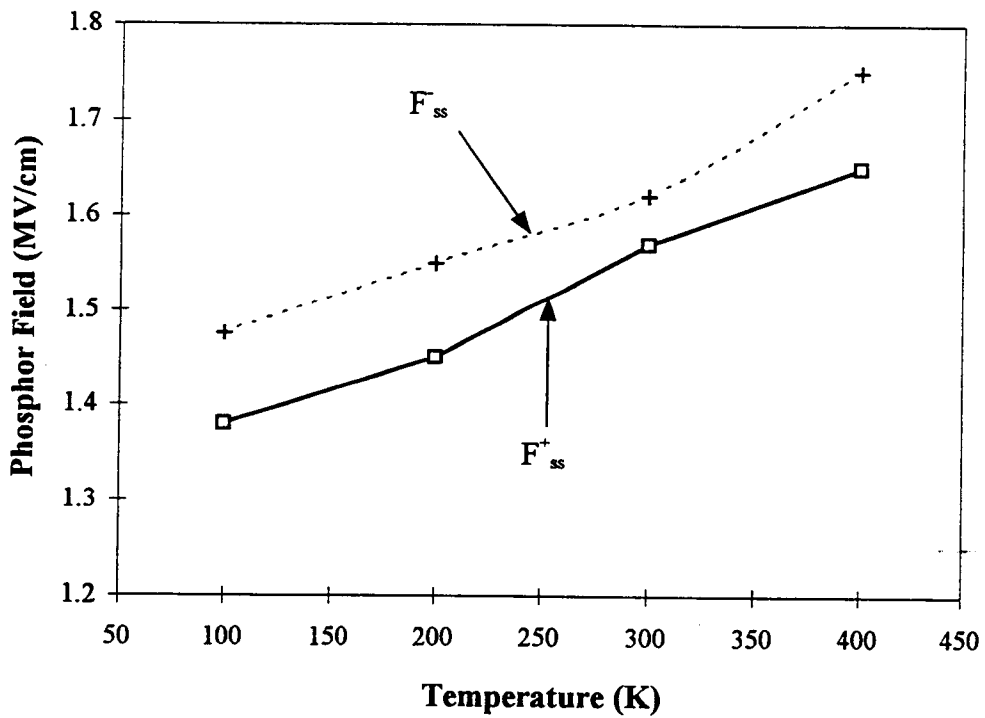


Figure 4-18: F_{ss} versus temperature for the "Thick" ALE ZnS:Mn ACTFEL device.

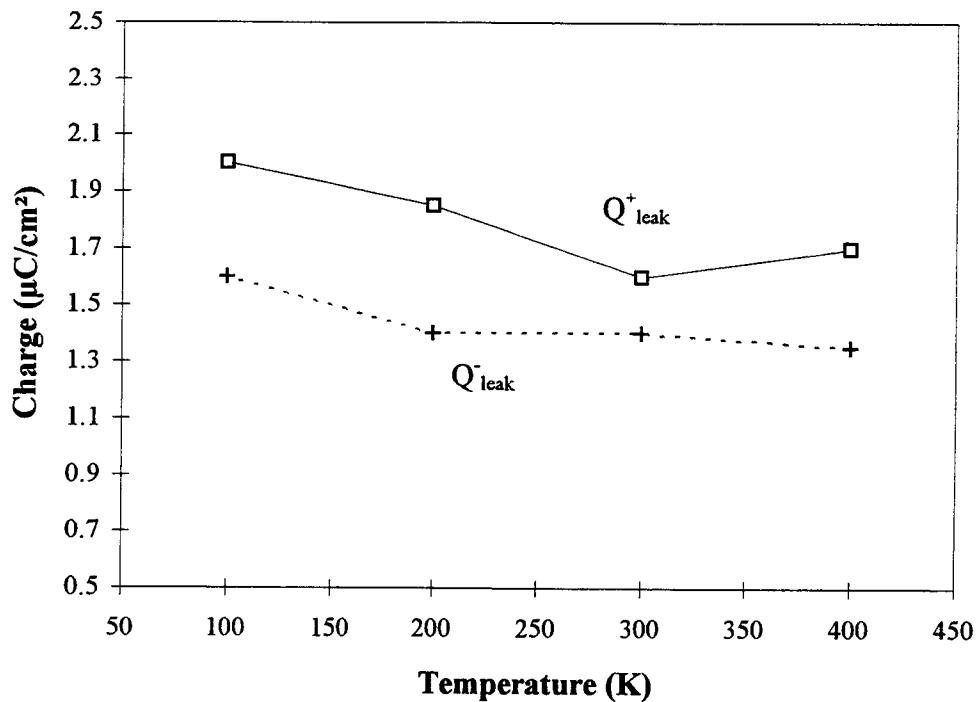


Figure 4-19: Q_{leak} versus temperature for the "Thick" ALE ZnS:Mn ACTFEL device.

These figures show that Q_{cond} , Q_{relax} , Q_{pol} , and F_{ss} all tend to increase with increasing temperature, although Q_{cond} and Q_{pol} show some evidence for saturation between 300 K and 400 K. The Q - F_p trends show that Q_{leak} decreases slightly with increasing temperature.

The Q - F_p trends of increasing Q_{cond} , Q_{pol} , and F_{ss} are internally self-consistent: i.e. more conduction charge flows because of a larger phosphor field and more polarization charge is a consequence of having a larger conduction charge transported. Unfortunately, these Q_{cond} , Q_{pol} , and F_{ss} trends seem to be inconsistent with the fact that Q_{leak} is found to decrease slightly with temperature; i.e. if Q_{pol} increases, it is expected that Q_{leak} would also

increase since a larger Q_{pol} implies a larger polarization electrical field to extract electrons from interface states; also, a larger Q_{pol} implies that some of the interface electrons occupy more shallow states and so can more readily be emitted as leakage charge.

One possible reason for Q_{leak} not increasing with increasing temperature is that electrons emitted from interface states may be trapped in the bulk prior to traveling across the entire length of the phosphor to the opposite interface; this trapping would be manifest as a reduction in leakage charge, compared to what it would have been if trapping did not occur. C-V asymmetry, V_{to1} softening, and Q-F_p & Q-V voltage offset trends support the possibility of bulk trapping since these trends establish that more charge is sourced from the phosphor bulk at elevated temperatures. Additionally, it is well known that the capture cross-section of traps which undergo multiphonon emission have capture-cross section which increase with increasing temperature [33] as

$$\sigma = \sigma_{\infty} \exp\left(\frac{-E_{\infty}}{KT}\right), \quad (4.1)$$

where σ_{∞} and E_{∞} are the capture cross section and activation energy at infinitely high temperature, respectively. Thus, an enhanced rate of trapping is expected if trapping is via multiphonon emission. Therefore, the observed Q-F_p trends in which Q_{cond} , Q_{pol} , and F_{ss} increase and Q_{leak} is decreasing slightly with increasing temperature are considered to be self-consistent trends, as long as the Q_{leak} trend is attributed to an increase in trapping with increasing temperature.

In summary, the experimental data shown in Figs. 4-8 through 4-19 leads to the following observations:

- (1) The insulator capacitance increases with increasing temperature. This is attributed to an increase in space charge generation as a function of temperature.
- (2) Softening of the V_{to1} region of the C-V curve is observed. This observation indicates that charge is sourced at least partially from the phosphor bulk and not exclusively from the interfaces.
- (3) The amount of offset of Q- F_p and Q-V curves increases as a function of temperature. This is evidence that space charge is generated asymmetrically across the phosphor.
- (4) Q_{cond} , Q_{pol} , Q_{relax} , and F_{ss} increase with increasing temperature whereas Q_{leak} decreases slightly with increasing temperature.

Thus, the existent data indicates that these temperature-dependent trends in the electrical characteristics arise from the temperature-dependence of space charge generation and, perhaps, recombination. The initial impetus of this temperature-dependent study was to try to determine whether bulk space charge arises from bulk trap field-emission or band-to-trap impact ionization. The idea behind this experiment is that for a constant electric field, field-emission should be temperature-independent, whereas the rate of band-to-trap impact ionization should increase with decreasing temperature due to the fact that the electron distribution would be hotter at low temperature due to the presence of fewer phonons. However, the present experiment is inconclusive since the phosphor field changes with temperature such that which mechanism dominates cannot be established from these temperature-dependent measurements. Therefore, it is suggested that a temperature-dependent study of the electrical characteristics using a field-control circuit to maintain the phosphor field constant may be a viable approach for determining

the mechanism of space charge generation. This experiment is suggested as future work in Chapter 5.

4.7 Aging Study of the “Normal” ALE ZnS:Mn ACTFEL Device

An aging study of the “Normal” ALE ZnS:Mn ACTFEL device at room temperature yields a result which is similar to the aging study performed by Abu-Dayah [14]. Note that the devices employed by Abu-Dayah are very similar to the “Normal” device used in this study but were prepared approximately two years earlier when the ALE process and device structure were slightly different from that used presently.

Figure 4-20 shows C-V curves as a function of aging time for a positive voltage pulse applied to the Al electrode. It is observed that the C-V curves shift to higher voltages in a non-rigid manner as a function of aging time. This non-rigid shift is attributed to an increase of the pre-clamping interface state density, Q_{ss} , which is related to the slope of the C-V curve in the transition region between where the total and insulator capacitances are measured. Figure 4-22 shows that C_i^{cv} of the positive polarity decreases with aging time and Fig. 4-23 shows that Q_{ss}^+ increases as aging time due to the non-rigid shift of C-V curves. It is also observed from Fig. 4-22 that the C_i^{cv} decreases as a function of aging time; however, C_i^{cv} is still much greater than C_i^{phy} . Returning to Fig. 4-20 the softening of the C-V curves near V_{b1} with aging indicates that some electrons are sourced from the bulk ZnS and not exclusively from the interface.

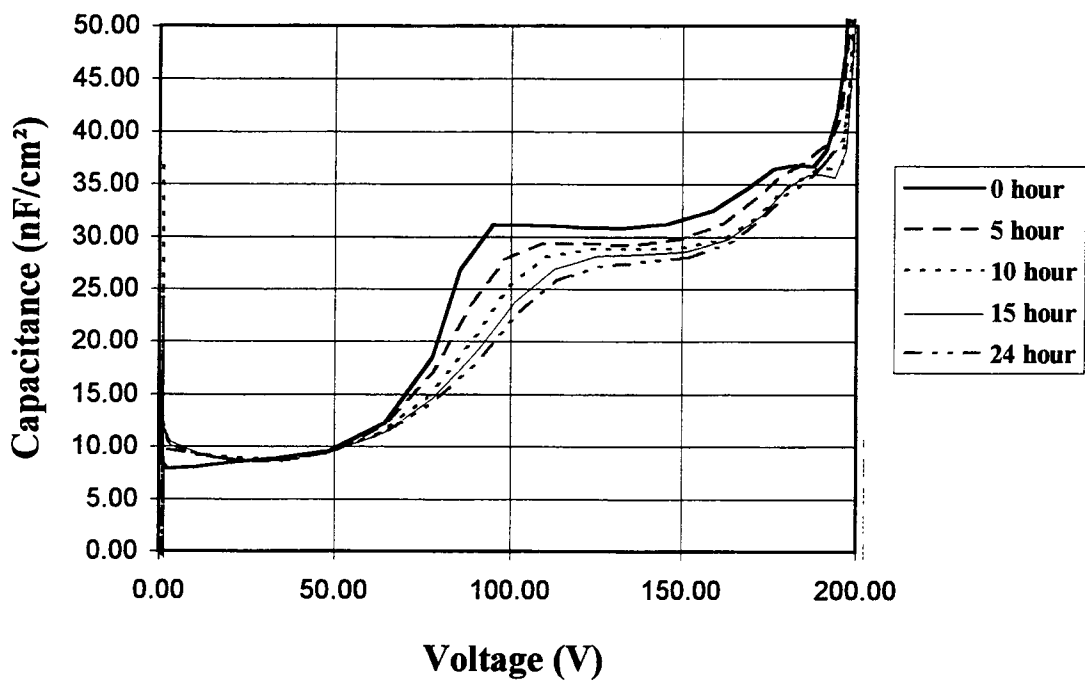


Figure 4-20: C-V curves as a function of aging time for the “Normal” ALE ZnS:Mn ACTFEL device when the Al electrode is positively biased.

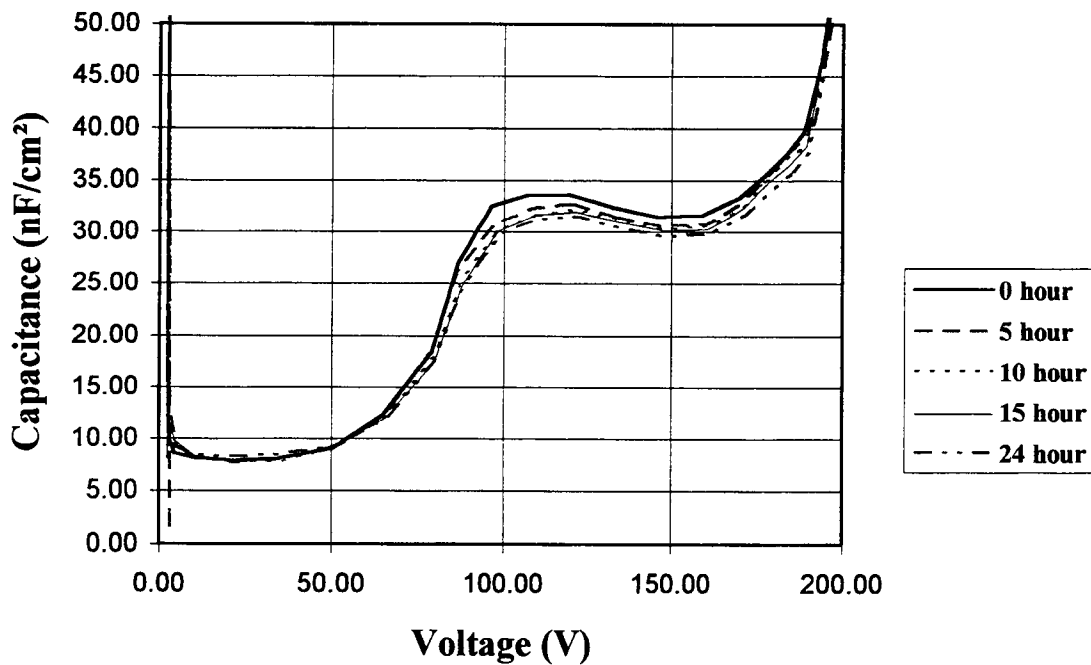


Figure 4-21: C-V curves as a function of aging time for the “Normal” ALE ZnS:Mn ACTFEL device when the Al electrode is negatively biased.

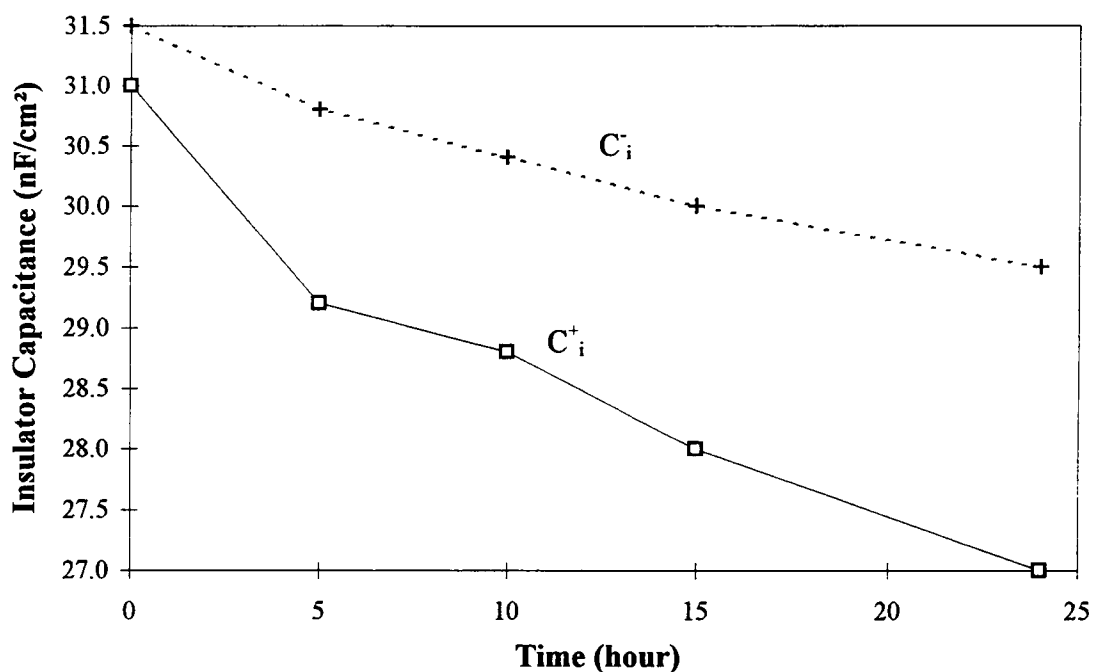


Figure 4-22: Insulator capacitance measured from C-V curves as a function of aging time for the “Normal” ALE ZnS:Mn ACTFEL device.

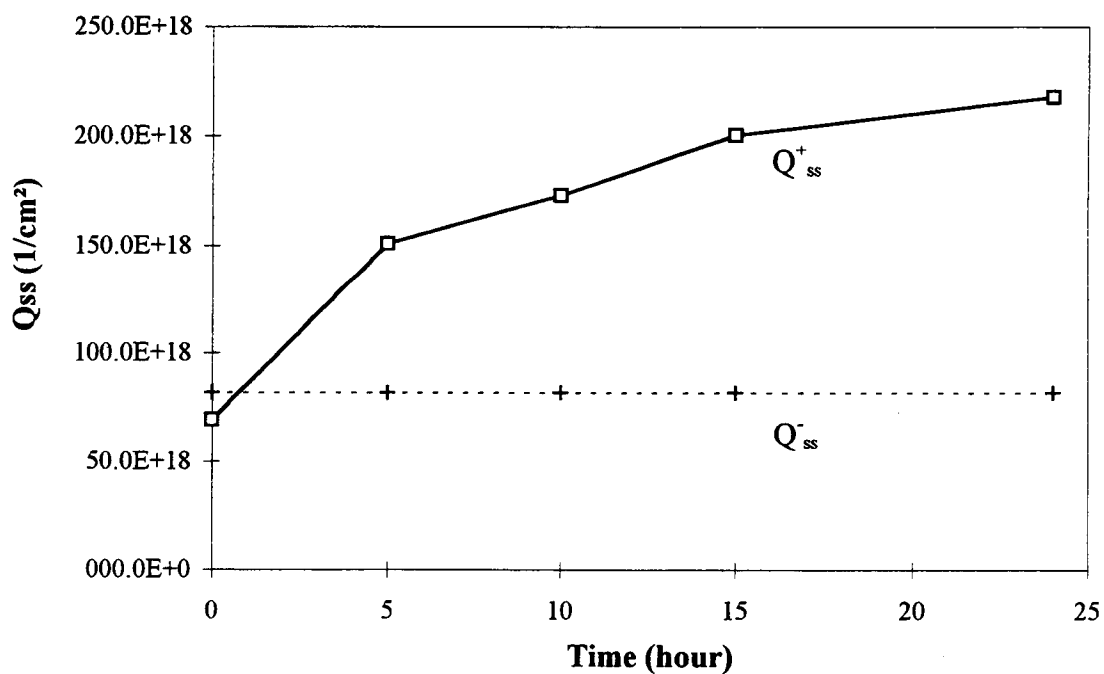


Figure 4-23: Q_{ss} versus aging time for the “Normal” ALE ZnS:Mn ACTFEL device.

Figure 4-21 shows C-V curves as a function of aging time for a negative voltage pulse applied to the Al electrode. The negative polarity C_i^{cv} also decreases with aging time, as shown in Figs. 4-21 and 4-22. Furthermore, it is evident from Fig. 4-21 that the amount of C-V overshoot decreases with aging time. Previous work [14] proposed that the reduction of C_i^{cv} and C-V overshoot with aging time is attributed to a reduction of the local electric field near the Al interface. This reduction of the local electrical field results in less space charge generation. From Fig. 4-21 it is evident that the C-V curves shift slightly to higher voltage with aging with very little change in slope; this indicates that Q_{ss} is relatively constant with aging time, as shown in Fig. 4-23. The steepness of the C-V curve indicates that Q_{ss} is relatively small for this polarity. The asymmetry of the C-V curves shows that the centroid of space charge generation is not located at the center of the phosphor layer and/or the interface state densities are asymmetrical.

Other aging trends are obtained from Q-F_p analysis and are shown in Figs. 4-24 to 4-27. It is observed that the Q_{cond} , Q_{leak} , and Q_{relax} all decrease and saturate with aging time for both polarities. In contrast, Q_{pol} and F_{ss} both increase and then saturate with aging time for both polarities. Note that the Q_{pol} and F_{ss} values plotted in Figs. 4-26 and 4-27, respectively, are "offset-corrected" by adjusting with ΔF_{ss} and ΔQ_{pol} . ΔF_{ss} and ΔQ_{pol} is the difference between the center of the Q-F_p curve and the midpoint of AF segment in the Q-F_p curve. Also note that Q_{cond} , Q_{relax} , and Q_{leak} require no such of "offset-correction". In summary, all of the aging trends presented in Figs. 4-20 to 4-27 are similar to the aging trends previously reported by Abu-Dayah [14].

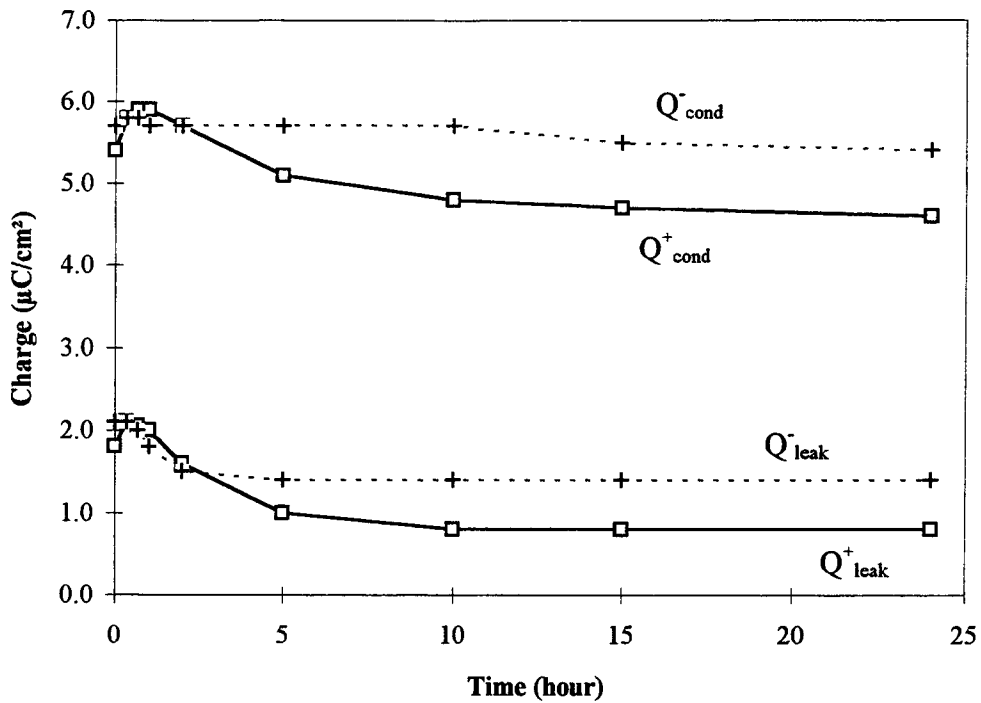


Figure 4-24: Q_{cond} and Q_{leak} versus aging time for the "Normal" ALE ZnS:Mn ACTFEL device.

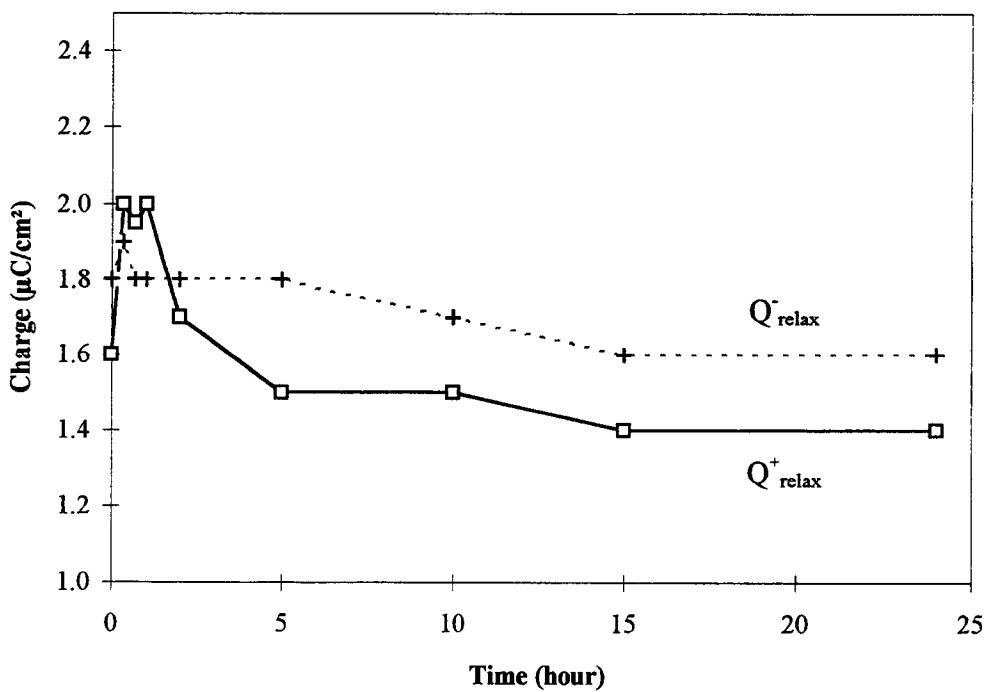


Figure 4-25: Q_{relax} versus aging time for the "Normal" ALE ZnS:Mn ACTFEL device.

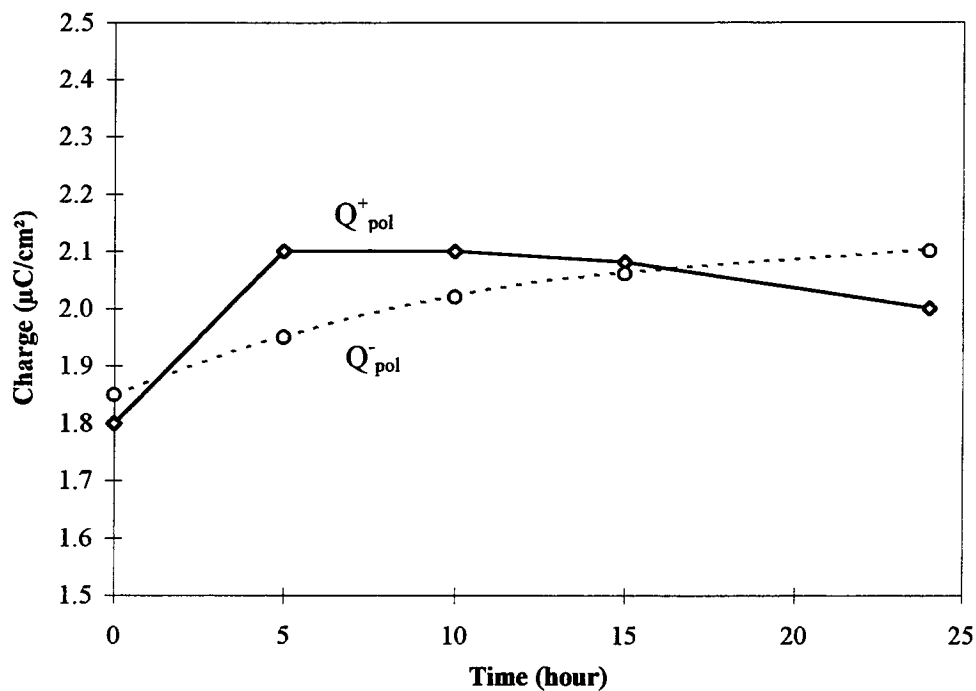


Figure 4-26: Q_{pol} versus aging time for the "Normal" ALE ZnS:Mn ACTFEL device.

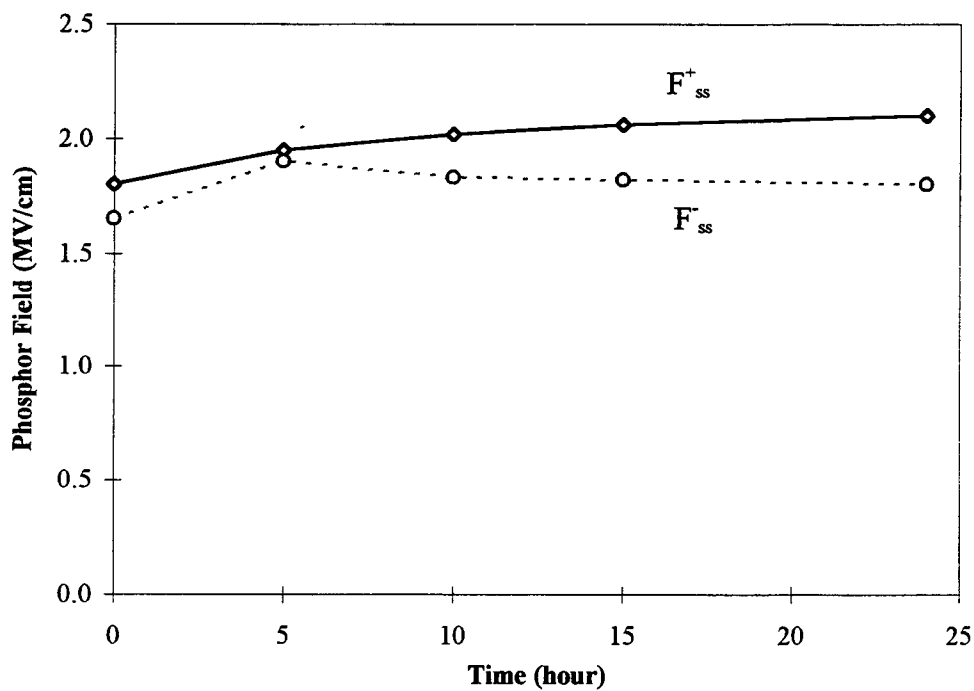


Figure 4-27: F_{ss} versus aging time for the "Normal" ALE ZnS:Mn ACTFEL device.

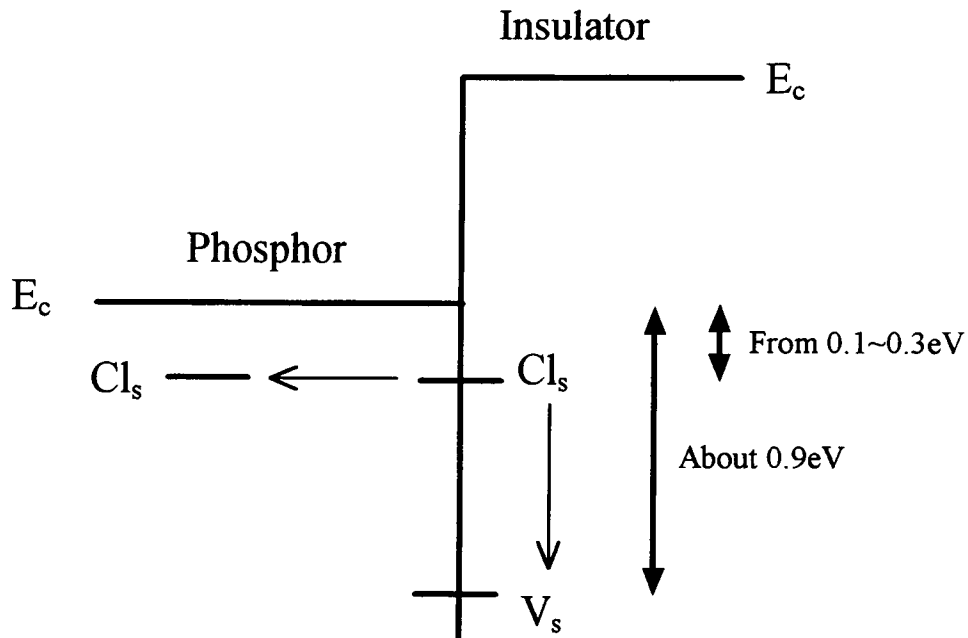


Figure 4-28: Proposed aging mechanism for the “Normal” ALE ZnS:Mn ACTFEL device.

An aging model proposed by Abu-Dayah *et al.* [14] and clarified by the space charge simulation of Keir [13, 28] asserts that the chlorine concentration in the ZnS phosphor near the Al interface is much greater than the chlorine concentration near the ITO interface due to the nature of the growth of these ALE ACTFEL devices. As shown in Fig. 4-28, [27, 29] chlorine on a sulfur site, Cl_s , is considered to be a relatively shallow donor in ZnS. With aging, chlorine moves away from the interface at the Al side into the ZnS bulk, creating deeper interface state as sulfur vacancies, V_s 's, are left behind at the interface. Previous researchers have concluded that V_s 's are the source of interface states

[14]. By invoking this model, it is possible to explain the reduction of conduction charge, reduction of leakage charge and the increase in polarization charge and steady-state field with aging time as a consequence of the creation of deeper interface states. The decrease in C_i^{cv} and, to a certain extent, the charges in Q_{ss} are attributed to the migration of Cl during aging.

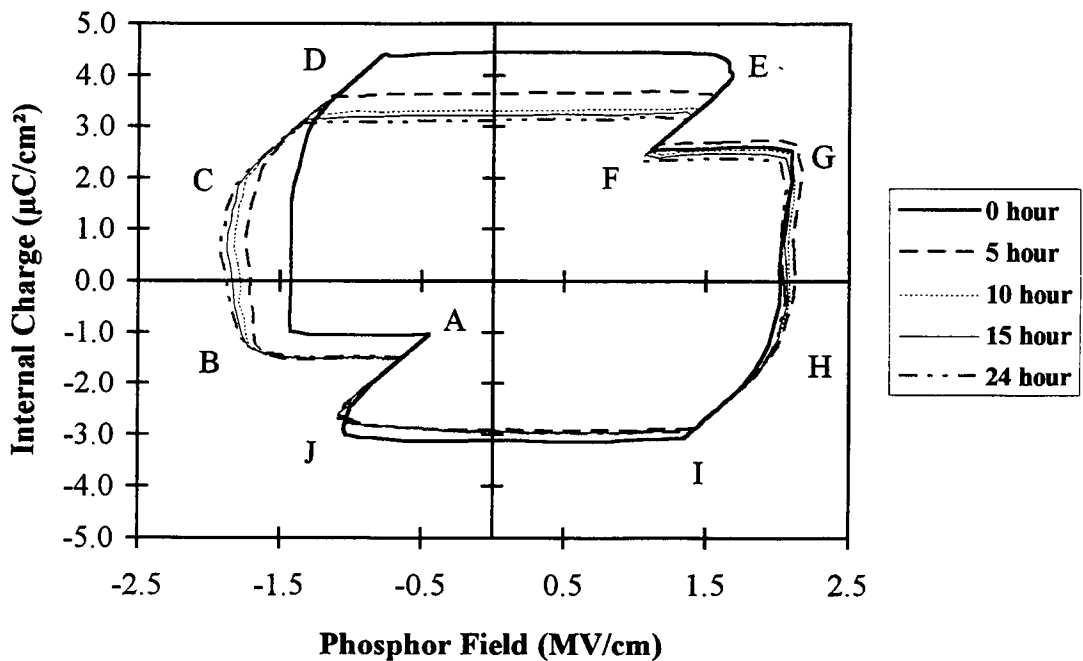


Figure 4-29: $Q-F_p$ curves as a function of aging time for the "Normal" ALE ZnS:Mn ACTFEL device.

$Q-F_p$ curves as a function of aging time are shown in Fig. 4-29. Note that the zero hour curve is highly asymmetrical and that the centroid of this curve is offset upward and to the right; the corresponding $Q-V$ curve shows a similar offset. Later, as aging progresses, there is less asymmetry and less offset in the $Q-F_p$ curves, which is consistent with the fact

that the magnitudes of the positive and negative internal fields (i.e. F_{ss}^+ and F_{ss}^-) get closer with aging. The offset of a Q- F_p or Q-V curve has been attributed [13, 28] to the centroid of space charge generation being located away from the center of the phosphor. Thus, the offset aging trend presented in Fig. 4-28 suggests that the centroid of space charge generation is initially close to the Al interface and moves closer to the center of the phosphor with aging. Thus, this offset aging trend is consistent with the migration of an enhanced concentration of Cl away from the Al interface into the ZnS bulk.

The aging trends of the "Normal" sample at higher or lower temperatures (i.e. 52 °C and -10 °C, respectively) are very similar to the aging trend at room temperature, except that the aging at 52 °C is accelerated, while the aging at -10 °C is slow.

4.8 Aging Study of the "Thick" ALE ZnS:Mn ACTFEL Device

An aging study of the "Thick" ALE ZnS:Mn ACTFEL device yields significantly different results than that of the "Normal" ALE ZnS:Mn ACTFEL device. Figures 4-30 and 4-31 show C-V curves as a function of aging time for positive and negative applied pulses to the Al electrode, respectively. Unlike the "Normal" sample, the C-V curves of the "Thick" sample are much less voltage polarity-dependent and exhibit similar aging trends. The C-V curves for both polarities shift to higher voltages in an almost rigid manner with aging time; this suggests that most of the injected charge is sourced from interface states. However, C_i^{cv} is significantly greater than C_i^{phys} which indicates that space charge is being generated in this device. Also, a small amount of overshoot is observed in

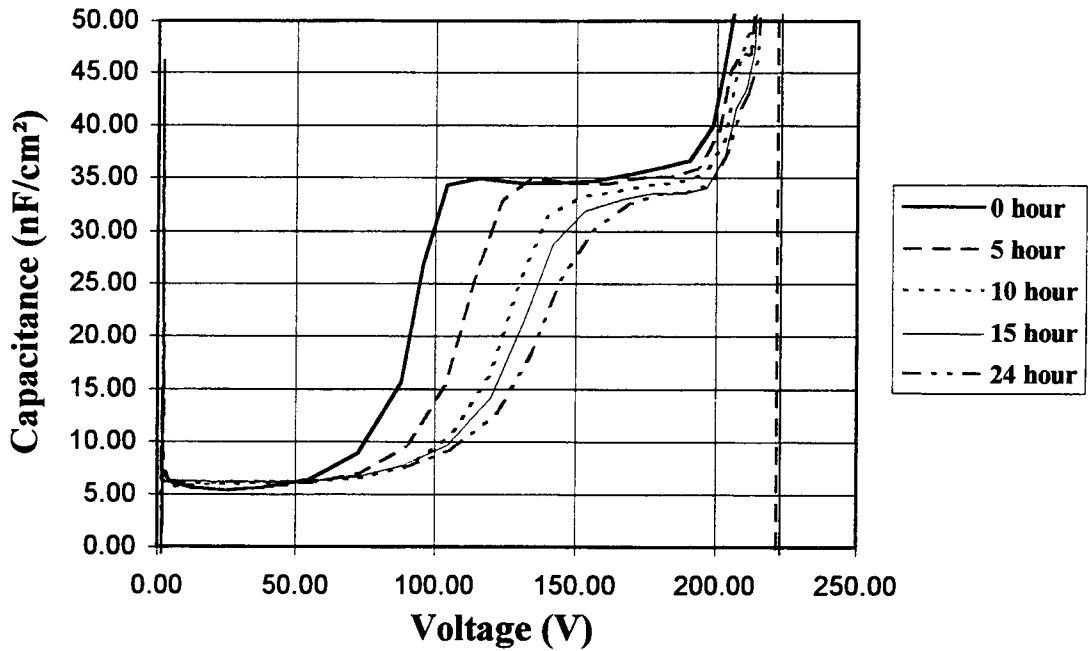


Figure 4-30: C-V curves as a function of aging time for the “Thick” ALE ZnS:Mn ACTFEL device when the Al electrode is positively biased.

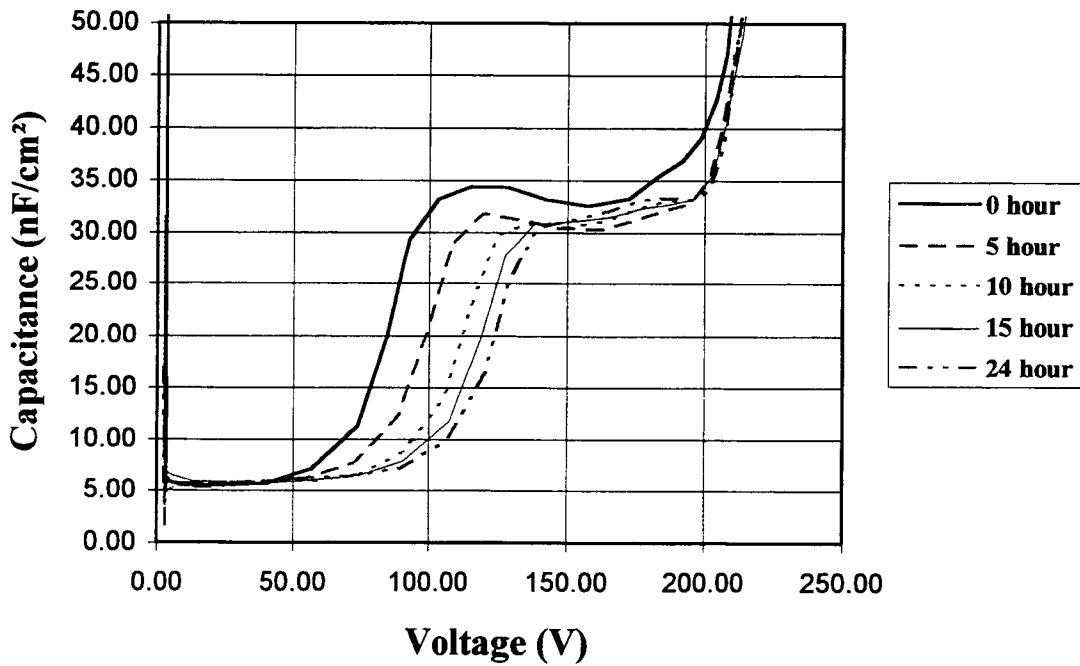


Figure 4-31: C-V curves as a function of aging time for the “Thick” ALE ZnS:Mn ACTFEL device when the Al electrode is negatively biased.

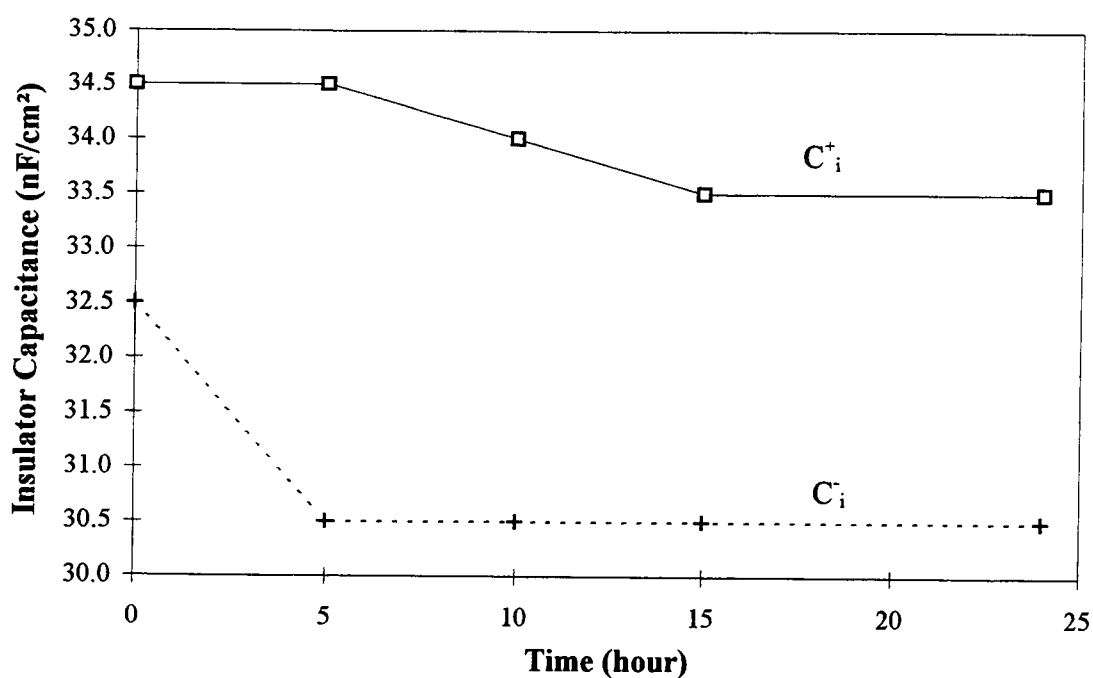


Figure 4-32: Insulator capacitance measured from C-V curves as a function of aging of the "Thick" ALE ZnS:Mn ACTFEL device.

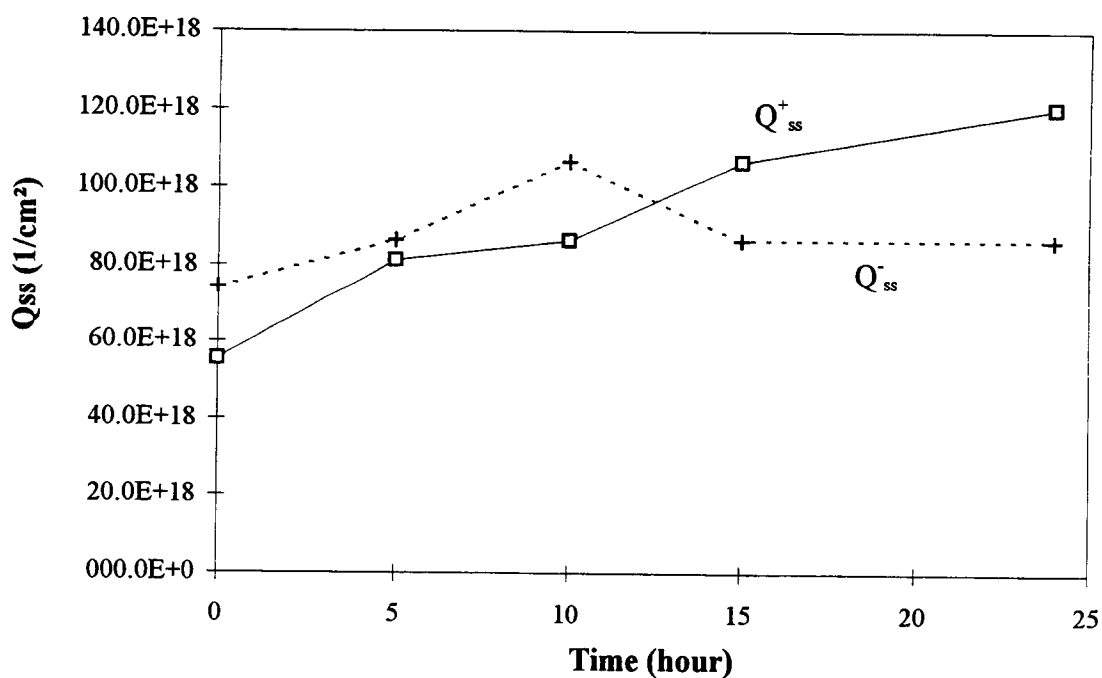


Figure 4-33: Q_{ss} versus aging time for the "Thick" ALE ZnS:Mn ACTFEL device.

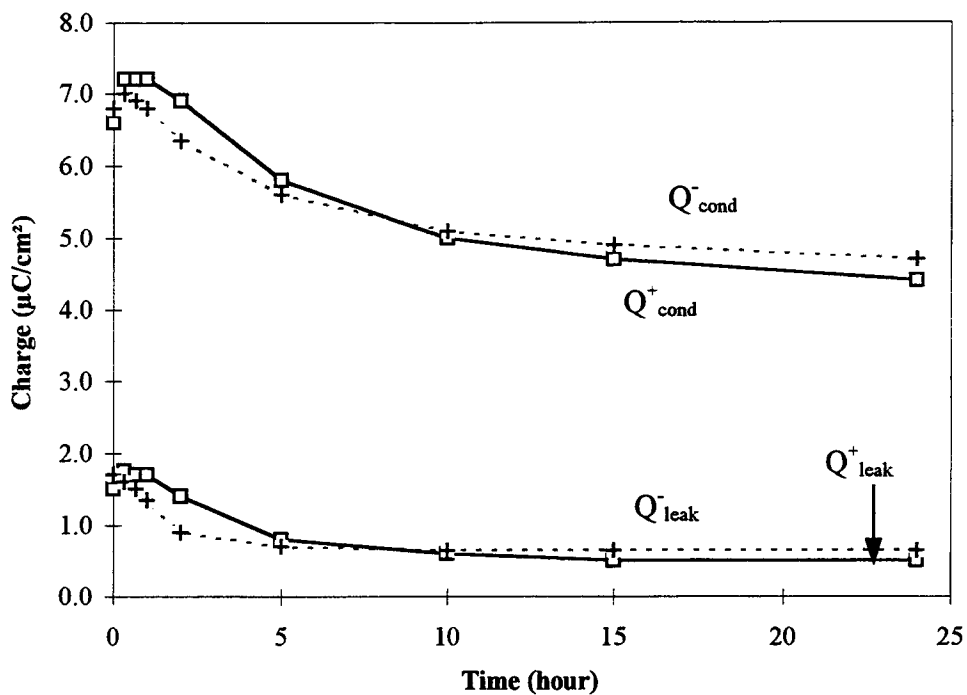


Figure 4-34: Q_{cond} and Q_{leak} versus aging time for the "Thick" ALE ZnS:Mn ACTFEL device.

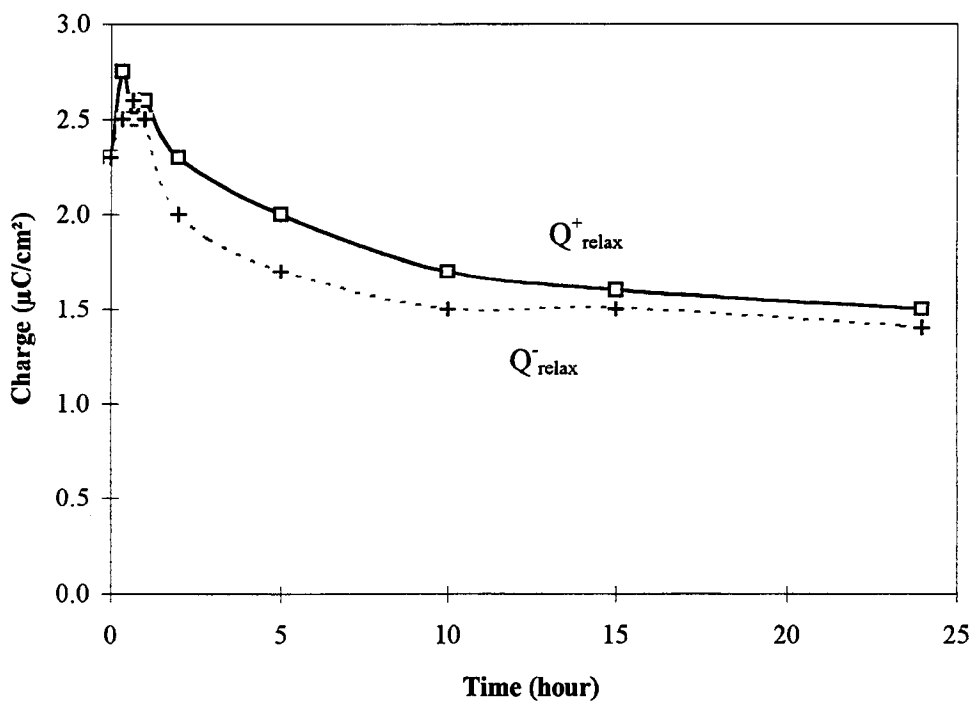


Figure 4-35: Q_{relax} versus aging time for the "Thick" ALE ZnS:Mn ACTFEL device.

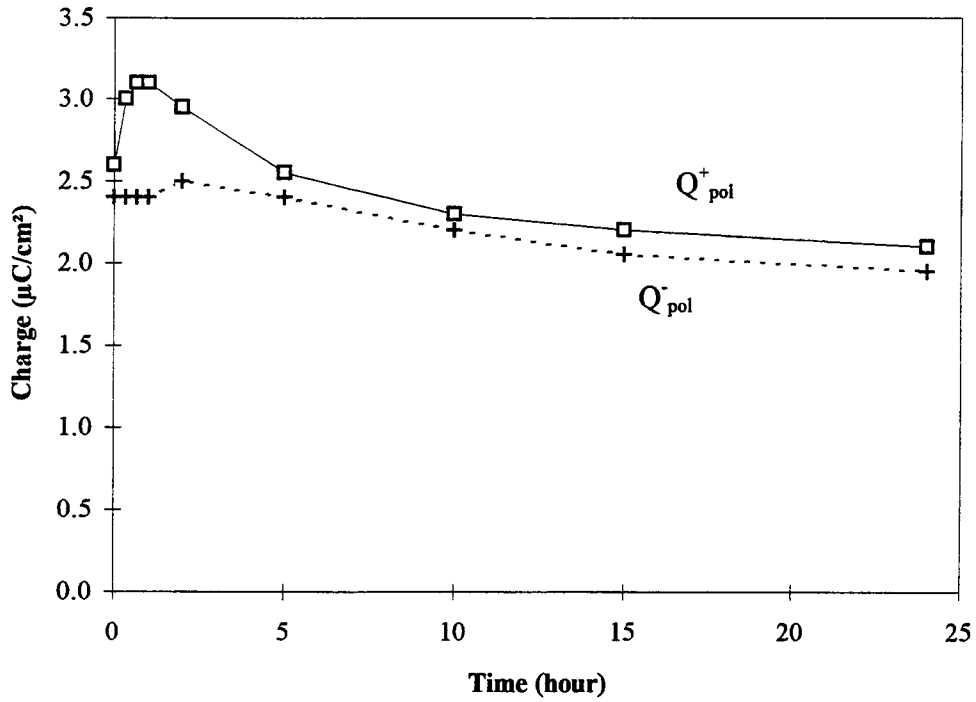


Figure 4-36: Q_{pol} versus aging time for the "Thick" ALE ZnS:Mn ACTFEL device.

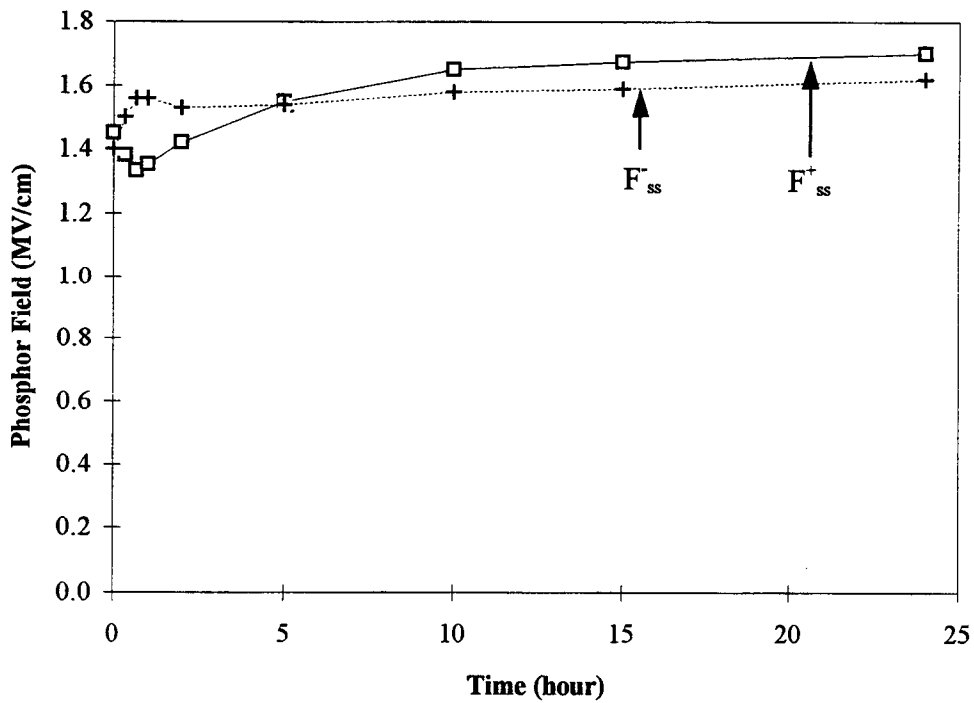


Figure 4-37: F_{ss} versus aging time for the "Thick" ALE ZnS:Mn ACTFEL device.

the C-V curves of negative polarity. As shown in Fig. 4-32, C_i^{cv} decreases slightly for both polarities which is attributed to bulk charge rearrangement (probably Cl migration) with aging. As shown in Fig. 4-33, Q_{ss}^+ slowly increases with aging time and Q_{ss}^- remains fairly constant during aging. Further evidence that Q_{ss}^- is constant is the rigid shift of the C-V curves of negative polarity toward higher voltage with aging time. The steepness of the C-V curve indicates that Q_{ss} is relatively small.

Figures 4-34 to 4-37 show that the conduction charge, leakage charge, relaxation charge, and polarization charge all decrease and almost saturate with aging time, while the average internal field increases slightly with aging time. Also note from these curves that there is much less voltage polarity asymmetry in these curves than that seen for the "Normal" sample. One of the most important aging trends is that of the polarization

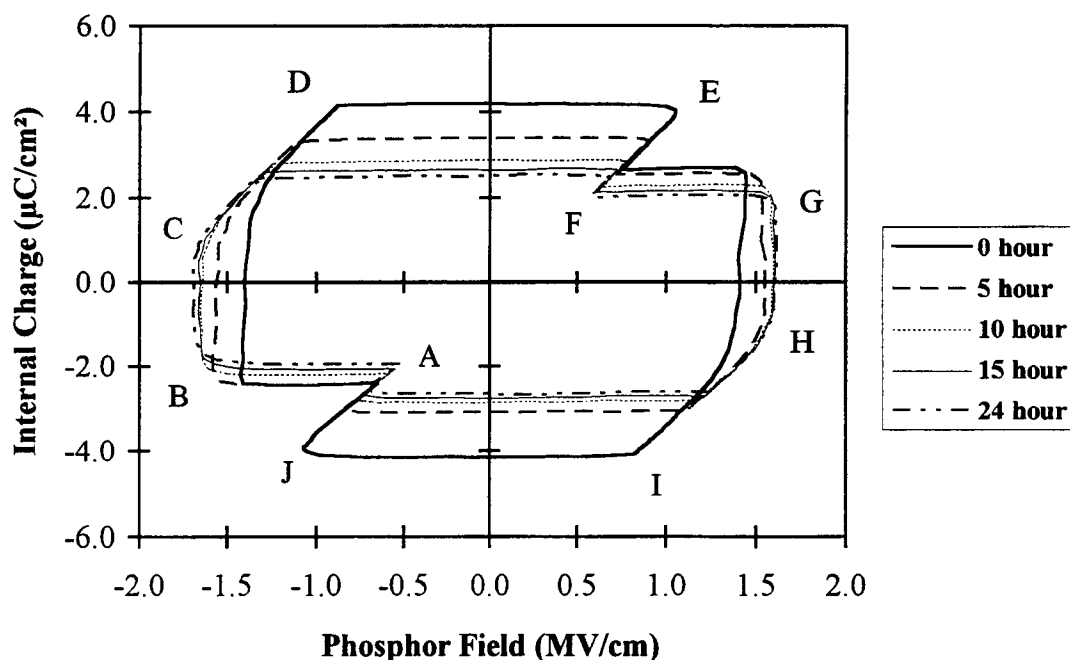


Figure 4-38: $Q-F_p$ curves as a function of aging time for the "Thick" ALE ZnS:Mn ACTFEL device.

charge, as indicated in Fig. 4-36. Q_{pol}^+ and Q_{pol}^- both decrease monotonically with aging time. This is in sharp contrast to the polarization charge trends shown in Fig. 4-26 for the "Normal" sample in which both Q_{pol} 's increase slightly and saturate with aging time. This observed decrease in the polarization charge with aging can be explained using the aging model proposed by Davidson et al. [23] for evaporated ZnS:Mn ACTFEL devices, as discussed below.

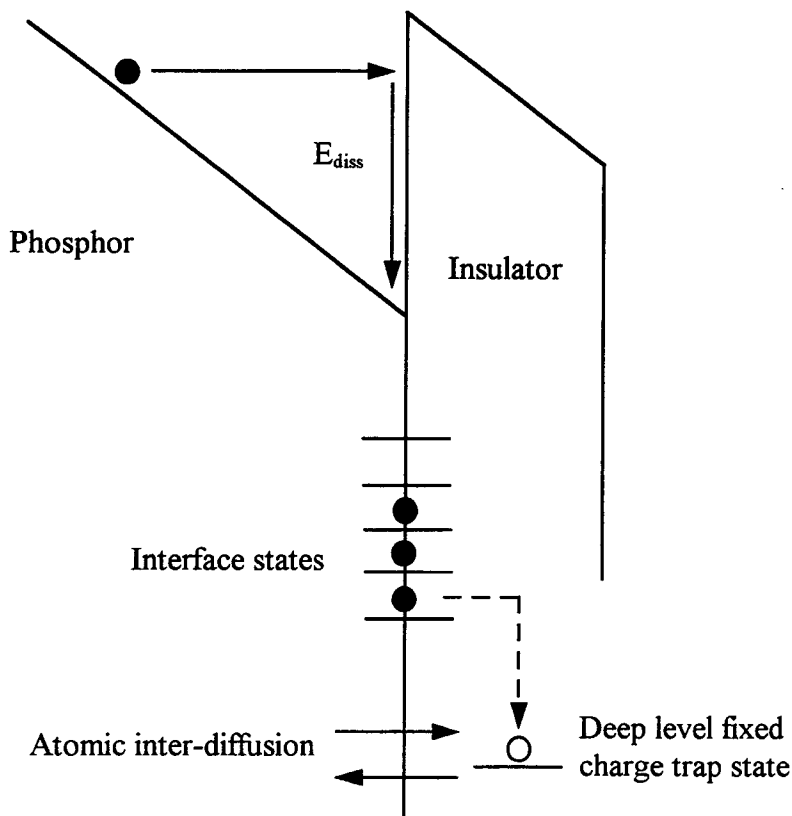


Figure 4-39: Proposed aging mechanism for the "Thick" ALE ZnS:Mn ACTFEL device.

The $Q-F_p$ curves as a function of aging time are displayed in Fig. 4-38. From this figure it is observed that the $Q-F_p$ curves are all quite symmetric. This is consistent with the symmetry of the aging trends of the various internal charges and field, as shown in Figs. 4-32 through 4-37. Also, there is no $Q-F_p$ or $Q-V$ offset present for the "Thick" sample, in contrast to that found for the "Normal" sample.

The same aging model as proposed previously to explain aging of the "Normal" thickness sample cannot be invoked to explain the distinctly different aging trends exhibited by the "Thick" sample. The rigid C-V shift to larger voltage observed for the "Thick" sample implies that most of the aging occurs near the phosphor/insulator interface. Both Davidson *et al.* [22, 23] and Pham *et al.* [2] observed C-V curves which shift rigidly to larger voltage in their respective studies of evaporated ZnS:Mn and thiogallate ACTFEL devices. Therefore the aging model originally proposed by Davidson *et al.* [22, 23] is used to explain the dominant aging behavior of the "Thick" sample. Davidson *et al.*'s aging model involves the creation of deep level, fixed charge states at the phosphor/insulator interfaces as a consequence of atomic migration at the interface during aging. Figure 4-39 illustrates the primary features of this aging mechanism. Creation of such deep level, fixed charge states leads to a reduction of conduction charge (as interface state charge is trapped into fixed charge states), a reduction of leakage charge (since the most shallow interface states are no longer able to be injected from the interface during the zero bias portion of the applied voltage waveform as they now reside in fixed charge states), a reduction in polarization charge (due to charge balance of interface state and fixed charge at each interface, as explained in detail in Fig. 12 of reference 22), and an

increase in the steady-state field (since the conduction charge must be extracted from deeper interface states). The primary attribute of the aging model of Davidson *et al.* is that aging occurs near the phosphor/insulator interface. Although most of the “Thick” sample aging trends seem to be interface-related, several aging trends (namely, the slight reduction in C_i^{cv} and the increase in Q_{ss} with aging) appear to be more bulk-like. These bulk-like aging characteristics are attributed to the Cl migration aging model invoked to explain aging of the “Normal” thickness sample. Finally, note that the magnitude of C_i^{cv} for the “Thick” device indicates that a significant amount of space charge generation occurs in this device. However, the fact that the aging trends are fairly symmetric with respect to the applied voltage polarity suggests that the charge centroid of this space charge generation is located near to the center of the ZnS phosphor and that its position does not change appreciably with aging time.

The aging trends of the “Thick” sample at higher or lower temperature (i.e. 52 °C and -10 °C, respectively.) are similar to the aging trend of the “Thick” sample at room temperature, except that aging is accelerated at high temperature and is slower at low temperature.

4.9 Summary of ALE ZnS:Mn ACTFEL Device Aging Trends

It is observed from previous sections that the dominant aging trends of the “Normal” sample are more bulk-like, while the aging trends of the “Thick” sample are more interface-like. These findings motivated an investigation of the aging trend of the

“Thin” sample, which is found to have the least amount of space charge generation in the phosphor.

The dominant aging trends of the “Thin” sample are bulk-like and are very similar to aging trends of the “Normal” sample. For the “Thin” sample, the effective insulator capacitances (i.e. C_i^{cv} or C_i^{qfp}) decrease with aging time and the C-V curves shift in an asymmetrical, non-rigid manner. All of these features are similar to the aging trends of the “Normal” sample discussed in Section 9 of this chapter.

The aging study observations for these three samples lead to following picture of aging for ALE ZnS:Mn ACTFEL devices with varying thicknesses. For the “Thin” and “Normal” samples, in which the phosphor layer is relatively thin, the dominant aging mechanism involves chlorine migration from the phosphor/insulator interface near the Al electrode into the bulk of phosphor. The phosphor of the “Thick” sample is thicker than that of the other two samples. Although chlorine is undoubtedly present in the bulk of the “Thick” phosphor, it appears to be more uniformly distributed throughout the phosphor and less likely to migrate during aging, presumably because of the absence of a concentration gradient. Therefore, interface-like aging appears to be the dominant aging mechanism operating in these ACTFEL devices with thicker phosphor layers.

4.10 Brightness-Voltage Measurements

The brightness-voltage (B-V) curves for fresh dots and after 24 hours of aging for the “Normal” and “Thick” samples are shown in Figs. 4-40 and 4-41, respectively. Both of

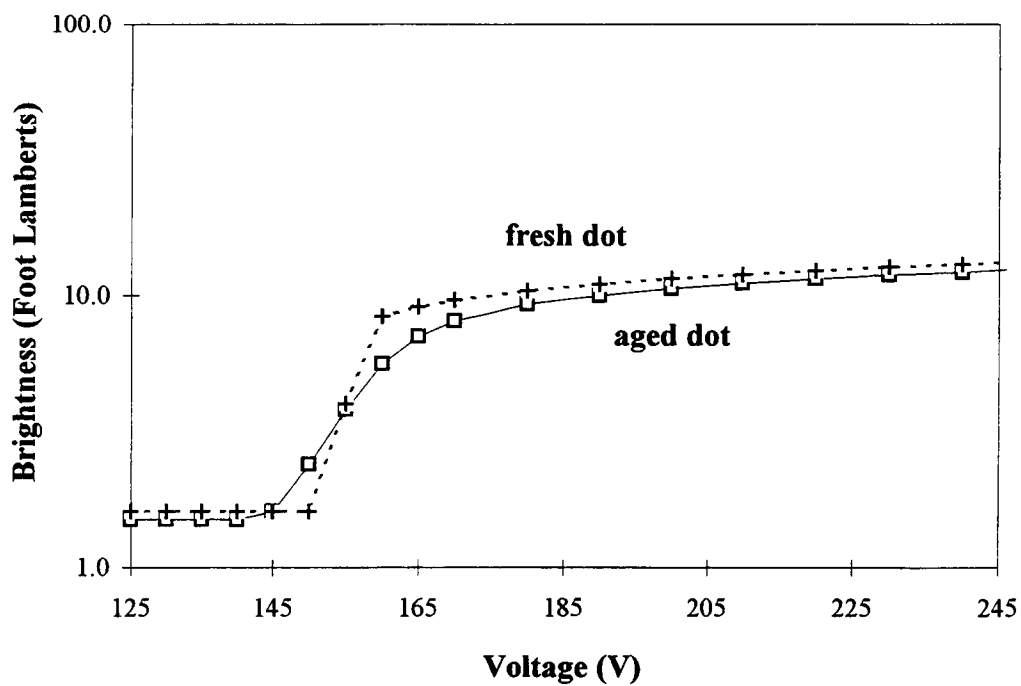


Figure 4-40: B-V curves of the fresh and aged dots for the “Normal” sample.

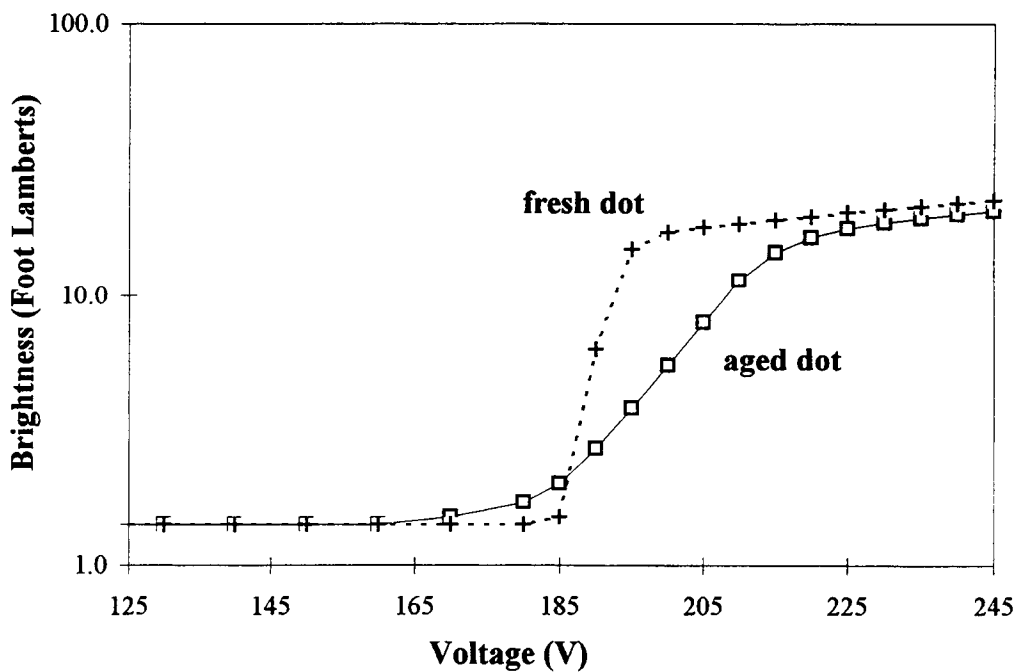


Figure 4-41: B-V curves of the fresh and aged dots for the “Thick” sample.

these samples exhibit some n-type shifting of the B-V curves as evidenced by the fact that the threshold voltage washes out and shifts to lower voltages. However, there is also some evidence of a p-shift in both samples since the B-V curves at above threshold shift to higher voltages; this p-like shift is particularly significant for the "Thick" sample. Clearly, more work is required before these kinds of B-V trends can be understood within the context of the measured electrical aging trends.

Chapter 5 Conclusions and Recommendations for Future Work

5.1 Conclusions

Three ALE ZnS:Mn ACTFEL devices fabricated at Planar International are studied. These samples have the same layer structure and similar insulator thicknesses; only the phosphor layer thickness of these samples is intentionally varied. These samples are denoted “Thin”, “Normal”, and “Thick”, according to their phosphor thickness.

C-V, Q-V, and Q-F_p curves are collected from aged dots of these three samples. It is shown that more space charge generation is observed in a sample with a thicker phosphor layer. In agreement with previous researchers [28], it is proposed that the space charge generation is due to impact ionization of the zinc vacancy portion of chlorine-zinc vacancy self-activated defect complexes. Zinc vacancies are thought to be created via self-compensation of ZnS, since chloride compounds are used in the ALE process.

C-V, Q-V, and Q-F_p curves are obtained for the “Thick” sample as a function of temperature, since it is the sample with the most space charge generation. It is found that the effective insulator capacitance increases as the temperature increases. It is proposed that this increase is due to the larger rate of electron injection due to phonon-assisted tunneling. Note that deep-level impact ionization, which is proposed as the major mechanism for space charge generation, cannot account for the observed trend in which the effective insulator capacitance increases with increasing temperature. The rate of deep-level impact ionization should decrease with increasing temperature as the hot electron distribution will be cooler at a higher temperature because of increased phonon emission.

“Normal” and “Thick” samples shows two distinctly different aging trends. Two aging model proposed by previous OSU researchers [14, 16] are employed to explain the aging behavior of these two ACTFEL devices. Aging of the “Normal” sample is more bulk-like and is attributed to chlorine migration from near the Al electrode phosphor/insulator interface toward the bulk of the phosphor. The electrical signatures of bulk-like aging are non-rigid shifts of C-V curves, a constant or approximately constant turn-on voltage (V_{to1}), a softening of this V_{to1} voltage, and an insulator capacitance which decreases with aging time. In contrast, the “Thick” sample shows more interface-like aging trends which are ascribed to the creation of deep level fixed charge states near the phosphor/insulator interface. Evidence for this type of interface-like aging is provided by the fact that the C-V curves shift rigidly, the threshold voltage, V_{to1} , changes with aging time, and the decrease of the insulator capacitance is relatively small compared to that of the “Normal” sample.

Q_{max} - V_{max} experiments are performed with aged dots for all three samples. The threshold voltage obtained from a Q_{max} - V_{max} plot is found to be similar to the threshold voltage defined as the minimum of the externally applied voltage required to see light emission as detected by the human eye. The slope of the Q_{max} - V_{max} curve is found to be slightly greater than the insulator capacitance; this is evidence of band-to-band and/or trap-to-band impact ionization.

5.2 Recommendations for Future Work

(1) Test whether aging is reversible. Previous work [14, 16] has indicated that the aging of ALE ZnS:Mn ACTFEL devices is reversible. Heating or photo-excitation of the sample after aging should be performed to see whether the sample may be returned to its pre-aged state. Determining whether aging is reversible or irreversible provides an important clue as to the mechanism of aging (e.g. electron injection and trapping in the insulator is a reversible process, whereas atomic diffusion is an irreversible process [14]).

(2) Perform an aging study of ALE ZnS:Mn ACTFEL devices by simultaneously monitoring Q_{\max} - V_{\max} and B-V curves.

(3) Perform aging studies of various kinds of ACTFEL devices by monitoring the luminance as a function of aging time as well as the electrical characteristics. In this manner electrical and optical aging characteristics may be correlated.

(4) Perform aging studies at various temperatures and attempt to identify aging mechanism via Arrhenius analysis of the electrical and optical aging data.

Bibliography

- [1] Yoshimasa A. Ono, "Electroluminescence", Encyclopedia of Applied Physics, vol. 5, pp. 295, 1993.
- [2] L. V. Pham, M.S. Thesis, Oregon State University, 1995.
- [3] R. C. McArthur, J. D. Davidson, J. F. Wager, I. Kormaei, and C. N. King, "Capacitance-voltage characteristics of alternating-current thin-film electroluminescent devices", Appl. Phys. Lett. 56 (190), 1889, 1990.
- [4] G. Destriau, "Recherches sur les Scintillations des Zinc aux Rayons", Journal de Chime Physique., vol. 33, pp. 587, 1936.
- [5] Yoshimasa A. Ono, "Electroluminescent Displays," vol. 1, pp. 36, 1995. World Scientific Publishing Co. Pte. Ltd.
- [6] N. A. Vlasenko and Iu. A. Poplov, "Study of the electroluminescence of a sublimed ZnS-Mn phosphor", Optics & Spectroscopy, vol 8, pp. 39, 1960.
- [7] M. J. Russ and D. I. Kennedy, "The effects of double insulating layers on the electroluminescence of evaporated ZnS:Mn film", J. Electrochem. Soc. 114, p1066, 1967.
- [8] T. Inoguchi, M. Takeda, Y. Kakihara, Y. Nakata and M. Yoshida, "Stable high luminance Thin-Film electroluminescent", Digest of 1974 SID International Symposium (1974) 84
- [9] S. Mito, C. Suzuki, Y. Kanatani and M. Ise, Digest of 1974 SID International Symposium (1974) 86.
- [10] M. Takeda, Y. Kanatani, H. Kishishita, T. Inoguchi and K. Okano, Digest of 1980 SID International Symposium (1980) 66 and Proc. SID 22 (1981) 57.
- [11] C. H. L. Goodman, and M. V. Pessa, "Atomic layer epitaxy", J. Appl. Phys. vol. 60, No. 3, 1986.
- [12] D. H. Smith, "Modeling A. C. Thin-Film Electroluminescent Devices," J. Lum., vol. 23, pp. 209, 1981.
- [13] P. D. Keir, M. S. Thesis, Oregon State University, 1995.
- [14] A. Abu-Dayah, M.S. Thesis, Oregon State University, 1993.

- [15] Direct quotations on the wall of the laboratory in Planar America, Beaverton, Oregon, U.S.A.
- [16] A. A. Douglas, M. S. Thesis, Oregon State University, 1993.
- [17] M. Kumar, M. S. Thesis, Oregon State University, 1994.
- [18] A. Abu-Dayah, and J. F. Wager, "Aging Studies of Atomic Layer Epitaxy ZnS:Mn alternating-current thin-film electroluminescent devices," *J. Appl. Phys.* 75 (7), 1994.
- [19] P. Thioulouse, R. Tueta, A. Izrael, and N. Duruy, 1984 *SID Proc.* 15, p. 81 (1984).
- [20] A. Mikami, K. Tareda, K. Okibayashi, K. Tanaka, M. Yoshida, and S. Nakajima, J., "Aging characteristics of ZnS:Mn electroluminescent film grown by a chemical vapor deposition technique", *Appl. Phys.* 72, 773 (1992).
- [21] R. Tornqvist and S. Korpela, *J. Cryst. Growth* 59, 395 (1982).
- [22] J. D. Davidson, M.S. Thesis, Oregon State University, 1991.
- [23] J. D. Davidson, J. F. Wager, and S. Kobayashi, "Aging studies of evaporated ZnS:Mn alternating-current thin-film electroluminescent devices," *J. Appl. Phys.* 71 (8) 1992.
- [24] J. D. Davidson, J. F. Wager, R. I. Kormaei, C. N. King, and R. Williams, "Electrical Characterization and Modeling of Alternating-Current Thin-Film Electroluminescent Devices," *IEEE Transactions on Electron Devices*, vol. 39, NO. 5. 1992.
- [25] A. Abu-Dayah, J. F. Wager, and S. Kobayashi, "Internal charge-phosphor field characteristics of alternating-current thin-film electroluminescent devices," *Appl. Phys. Lett.* 62, 744, 1993.
- [26] E. Brinquier and A. Geoffroy, "Charge transfer in ZnS-type electroluminescence revisited", *Appl. Phys. Lett.* 60, 1256, 1992.
- [27] S. Shih, P. D. Keir, and J. F. Wager, "Space charge generation in atomic layer epitaxy ZnS:Mn alternating-current thin-film electroluminescent devices with varying phosphor layer thickness," accepted for publication in *J. Appl. Phys.*
- [28] P. D. Keir, W. M. Ang, and J. F. Wager, "Modeling space charge in alternating-current thin-film electroluminescent devices using a single sheet charge model," accepted for publication in *J. Appl. Phys.*

- [29] J. F. Wager, "Thermodynamics and kinetics of vacancy self-compensation in wide-bandgap semiconductors," *Philosophical Magazine A*, vol. 67, No. 4, 897-904, 1993.
- [30] G. Vincent, A. Chantre, and D. Bois, "Electric field effect on thermal emission of traps in semiconductor junctions", *J. Appl. Phys.*, vol. 50, no. 8, 1979.
- [31] W. M. Ang, S. Pennathur, L. Pham, J. F. Wager, S. M. Goodnick, and A. A. Douglas "Evidence for band-to-band impact ionization in evaporated ZnS:Mn alternating-current thin-film electroluminescent devices", *J. Appl. Phys.* vol. 77, No.6, 1995.
- [32] A. A. Douglas, J. F. Wager, D. C. Morton, J. B. Koh, and C. P. Hogg, "Evidence for space charge in atomic layer epitaxy ZnS:Mn alternating-current thin-film electroluminescent devices", vol. 73, No. 1, 1993.
- [33] C. H. Henry and D. V. Lang, "Nonradiative capture and recombination by multiphonon emission in GaAs and GaP", *Physical Review B*, Volume 15, Number 2, 15 January 1977.
- [34] J. D. Davidson, J. F. Wager, and S. Kobayashi, "Aging studies of evaporated ZnS:Mn alternating-current thin-film electroluminescent devices", *J. Appl. Phys.* 71, 4040 (1992).